Microfluidic Batch Process Platforms for Lab on a Chip Applications using Acoustofluidics

by

Citsabehsan Devendran
Bachelor of Engineering (Mechanical) (Hons.)

Thesis submitted in fulfilment
of the requirements for the degree of

Doctor of Philosophy

Supervisor: Assoc. Prof. Adrian Neild
Associate Supervisor: Dr. Tuncay Alan

Laboratory for Micro Systems (LMS)
Department of Mechanical and Aerospace Engineering
Faculty of Engineering
Monash University
Australia

November 2015

Microfluidic Batch Process Platforms for Lab on a Chip Applications using Acoustofluidics

Copyright Notices

Notice 1

Under the Copyright Act 1968, this thesis must be used only under the normal conditions of scholarly fair dealing. In particular no results or conclusions should be extracted from it, nor should it be copied or closely paraphrased in whole or in part without writen consent of the author. Proper written acknowledgement should be made for any assistance obtained from this thesis.

Notice 2

I certify that I have made all reasonable efforts to secrure copyright permissions for third-party content included in this thesis and have not knowingly added copyright content to my work without the owner's permission.

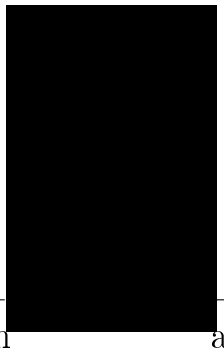

Citsabeh an
30th November 2015

"*The only way of discovering the limits of the possible is to venture a little way past them into the impossible*"

Arthur C. Clarke

In loving memory of my father and grandparents

In dedication to my mother

Acknowledgements

Firstly, I would like to express my deepest gratitude to my supervisors, Associate Professor Adrian Neild and Dr. Tuncay Alan for their full support, guidance, encouragement and understanding throughout this endeavour, without which, this candidature would have been unquestionably an overwhelming pursuit. The continuous and priceless advice given, has not only been useful to overcome research related challenges but an approach to life in general. Furthermore, I am extremely appreciative of the incredible patience and freedom given to run riot with ideas, no matter how dubious they were. I could not have asked for better mentors.

Secondly, to my fellow colleagues and friends at the Laboratory for Micro Systems, thank you for making this journey an unforgettable and entertaining one. The opportunity to work with an amazing and diverse group of people is an experience that I will cherish forever. It has been an absolute privilege and joy to have been given the opportunity to collaborate and bounce ideas of each other.

To the Department of Mechanical and Aerospace Engineering, the Faculty of Engineering and the Monash Institute of Graduate Research, thank you for the technical and administrative support given throughout my candidature. In addition, I would like to thank the Department of Education and Training for the financial support provided as part of the Australian Postgraduate Award given by the Australian Government.

To my friends, thank you for the continuous encouragement and emotional support which kept me sane in completing the work and the writing up of this thesis.

Finally, to my mother, Indrani Kandasamy thank you for your undying support, love and patience. This dream would not have been possible without your immense sacrifices. To my brother, Amahran Devendran for your never-ending encouragement and guidance. A special mention to my uncle and aunty, Mr. and Mrs. Ratnakumar, for your endless, wholesome support and encouragement.

Citsabehsan Devendran
Laboratory for Micro Systems
Monash University
November 2015

Contents

List of Figures

List of Tables

Abstract

The inception of microfluidics, utilising borrowed technology from the microelectronics industry, has enabled a wide range of applications in various fields ranging from engineering to biochemistry. Advancements in terms of microfabrication and micro-scale fluid control has led to the rise of Lab on a Chip. These systems aim to replicate the results of conventional laboratory procedures in miniaturised systems. Lab on a Chip systems, offer immense potential for a wide range of diagnostic and therapeutic tools. Furthermore, when sample volumes are extremely scarce, rendering conventional diagnostic methods and continuous flow microfluidic techniques impractical, other methods need to be established. To this end, microfluidic batch process systems offers a solution, although relatively underdeveloped. Batch process systems are a single or multi-stage process in which a certain quantity of inputs are processed to achieve the desired outcome one sample set at a time. It should be noted, as these systems operate at a much smaller scale, some conventional forcing techniques, such as centrifugation are no longer practical. Therefore, different actuation mechanisms need to be developed to replicate the results of their larger scale conventional laboratory and continuous flow counterparts. Acoustic excitation is a potential actuation mechanism which enables the handling of micron-sized particles and cells. Here, we look at different acoustic excitation methods and the underlying principles that allow acoustofluidic systems to manipulate particles for sample preparation and as point-of-care diagnostic tools. In this thesis, three systems are developed to perform particle manipulation both in liquid and air based batch process systems. Firstly, an open bulk acoustic wave system, allowing the ease of external gripping mechanisms is developed to perform size-deterministic separation of 3 μm and 10 μm particles. The task of particle separation is further explored using a different underlying principle and actuation method, and separation of 3.1 μm and 5.1 μm is achieved utilising surface acoustic waves, a different excitation mechanism that enables operation at relatively higher frequencies. Finally, optimisation of an acoustic resonator in air is carried out and serves as a building block for a complete 3-dimensional (3D) acoustic trapping microgripper to be used for individualised particle transport and inspection. Throughout this thesis, a case is made for acoustic based methods to be utilised in developing essential batch process systems for sample preparation and diagnostics.

Monash University

Declaration for thesis based or partially based on conjointly published or unpublished work

General Declaration

In accordance with Monash University Doctorate Regulation 17.2 Doctor of Philosophy and Research Master's regulations the following declarations are made:

I hereby declare that this thesis contains no material which has been accepted for the award of any other degree or diploma at any university or equivalent institution and that, to the best of my knowledge and belief, this thesis contains no material previously published or written by another person, except where due reference is made in the text of the thesis.

This thesis includes 3 original papers published in peer reviewed journals. The core theme of the thesis is batch process particle manipulation within acoustofluidic systems. The ideas, development and writing up of all the papers in the thesis were the principal responsibility of myself, the candidate, working within the Laboratory for Micro Systems (LMS), Department of Mechanical and Aerospace Engineering, Faculty of Engineering, under the supervision of Assoc. Prof. Adrian Neild and Dr. Tuncay Alan.

The inclusion of co-authors reflects the fact that the work came from active collaboration between researchers and acknowledges input into team-based research.

In the case of Chapters 3-5 my contribution to the work involved the following:

Thesis chapter	**Publication title**	**Publication status**	**Nature and extent of candidate's contribution**
3	Separation of particles using acoustic streaming and radiation forces in an open microfluidic channel	Published	Design and fabrication of devices, experimentation, development, results analysis, interpretation and writing.
4	Batch process particle separation using surface acoustic waves (SAW): integration of travelling and standing SAW	Published	Design and fabrication of devices, experimentation, numerical modelling, development, results analysis, interpretation and writing.
5	Optimisation of an acoustic resonator for particle manipulation in air	Published	Design and fabrication of devices, experimentation, numerical modelling, development, results analysis, interpretation and writing.

I have not renumbered sections of submitted or published papers in order to generate a consisten ion within the thesis.

Signed:

Name: C Devendran

Date: 30th November 2015

Publications and Outcomes

Articles in peer-reviewed journals

1. Citsabehsan Devendran, Ian Gralinski, and Adrian Neild. Separation of particles using acoustic streaming and radiation forces in an open microfluidic channel. *Microfluidics and Nanofluidics*, 17(5):879-890, 2014. [31]

2. Citsabehsan Devendran, Duncan R. Billson, David A. Hutchins, and Adrian Neild. Optimisation of an acoustic resonator for particle manipulation in air. *Sensors and Actuators, B: Chemical*, 224:529-538, 2016. [32]

3. Citsabehsan Devendran, Nipuna R. Gunasekara, David J. Collins, and Adrian Neild. Batch process particle separation using surface acoustic waves (SAW): integration of travelling and standing SAW. *RSC Adv.*, 6:5856-5864, 2016. [33]

Conference proceedings

1. Citsabehsan Devendran, Priscilla Rogers, Ian Gralinski, and Adrian Neild. Particle Manipulation and Separation in an Open Microfluidic Chamber. *2013 International Congress on Ultrasonics*, DOI:10.3850/978-981-07-5938-4_ P0146.

2. Adrian Neild, Priscilla Rogers, Ian Gralinski, Citsabehsan Devendran, Robert Walker and Tuncay Alan. Particle Manipulation in the Presence of Fluid Interfaces. *2013 International Congress on Ultrasonics*, DOI:10.3850/978-981-07-5938-4_ P0145, 2013.

3. Citsabehsan Devendran, Duncan R. Billson, David A. Hutchins, Tuncay Alan, and Adrian Neild. Acoustic resonator optimisation for airborne particle manipulation. *Physics Procedia*, 70:6-9, 2015. Proceedings of the 2015 ICU International Congress on Ultrasonics, Metz, France. [34]

Chapter 1

Introduction

1.1 Microfluidics

"Microfluidics is a multidisciplinary field that integrates various scientific fields ranging from engineering to biochemistry with the manipulation of tiny volumes of fluid at the sub-millimeter scales." [35]

In this chapter, the concept of microfluidics and subsequently the birth of Lab on a Chip (LOC) are to be introduced. This is followed by a brief overview of the outline and layout of the thesis.

1.1.1 The microfluidic paradigm and the birth of Lab on a Chip

The inception of microelectronics has given birth to the miniaturisation of technology and is considered the most significant enabling technology of the last century. [36] The ability to fabricate such small devices with the use of photolithography and other microfabrication techniques has indirectly given rise to the study of microfluidics. What was once considered impossible to realise experimentally, let alone commercially, just about half a century ago, is now one of the fastest growing fields in science, thanks to the semiconductor industry. [35]

In a wider perspective, microfluidics is a physical study of fluid at a very small scale, generally at the sub-millimeter scale (i.e. femtoliter (fL) to microliter (μL) volumes). [37] The ability to precisely manipulate fluids at these small scales allows us to take advantage of scaling laws that give rise to interesting phenomena that are sometimes highly beneficial. As a result of operating at such small scales, flow is generally in a laminar regime, which in turn makes handling of such samples easy and mixing highly controllable. In addition, the high surface tension and inter-facial forces along with capillary forces are highly desirable to perform certain tasks. [35] Although, the exploration of microfluidics is relatively new as an engineering study, evolution has long exhibited microfluidic systems in nature that surround us in our everyday life, such as the vascular system of a plant or the cardiovascular system in our body which efficiently transports essential components.

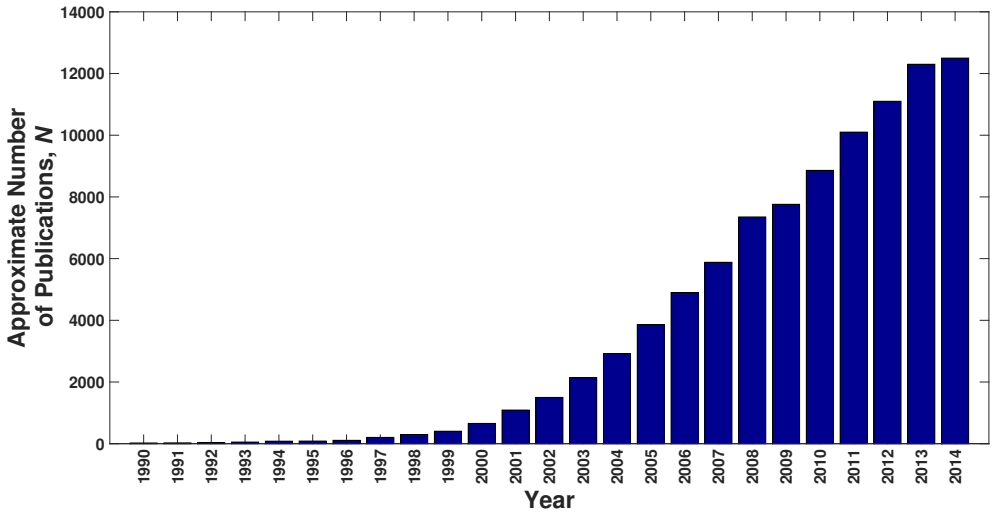

Figure 1.1: Approximate number of publications related to microfludics in recent years based on Google Scholar's database (Keyword: microfluidics)

The immense potential that arises from microfluidics has lead to the integration of multiple scientific fields such as engineering, physics, chemistry, nanotechnology, biotechnology and biochemistry. Since the conception of microfluidics, a widespread of techniques and processes have been developed for applications ranging from cartridges for ink jet printers, flow cytometry [38] to DNA analysis. [39, 40] Furthermore, the potential of operating at the micro scale has accelerated the development of new drugs and delivery technologies as well with the incorporation of microelectromechanical systems (MEMS) [41], thus, garnering an increased interest in microfluidics (see Fig. 1.1). These developments and the huge potential associated with it have given rise to the Lab on a Chip (LOC) concept whereby, individual laboratory procedures that are required to perform certain procedures such as blood diagnostic can be miniaturised integrated into a microchip. LOC devices are generally regarded as a subset of MEMS and Micro Total Analysis Systems (μTAS).

As a concept, LOC systems aim to achieve a small, compact, efficient and complete portable systems for various applications. [42] In this thesis however, the focus will be towards development of biomedical diagnostic and detection devices. Realisation of this concept would allow, point-of-care diagnostics anywhere in the world especially in remote and poor regions to be carried out in an efficient and cost-effective manner. The benefits that stem from such a tool or technique is immense as the increased sensitivity attribute associated with these systems decrease the detection lower limit, allowing for earlier diagnosis of diseases. In addition, the time-scale at which appropriate treatment can be administered is significantly reduced, thus, saving countless lives and reducing treatment costs, which is highly beneficial especially in resource and financially deprived regions. [43]

It should be noted, although, there are countless advantages by scaling down fluidic systems, there are a few disadvantages that are present as a result of operating at these

size scales. Drawbacks, such as the physical effects arising from interfacial forces, surface roughness and chemical interactions, are more dominant at these length scales. As a result, microfluidic processes sometimes need to utilise techniques that overcome these effects, thus, adding complexity as compared to conventional laboratory procedures. In addition, integration of multiple individual processes on a single chip platform proves to be difficult with current technological developments. Therefore, increased research and further development of techniques are essential to eradicate these drawbacks in the near future and allow for the integration and ability to build upon with layers of complexity as required by certain tasks, thus the focus of this thesis. Here, the integration of a few individual tasks (i.e. particle concentration and sorting) is to be performed simultaneously while ensuring high operational efficiency, thus, reducing issues that may arise when developing a complete system on a chip.

Further elaboration and an in-depth review of the development of Lab on a Chip systems is presented in Chapter 2 (Section 2.1).

1.2 Thesis Overview

The scope of this thesis has been to exploit the advantages and practicality that stem with the use of batch process systems in microfluidics. Various external forcing mechanisms are reviewed and acoustic manipulation is found to be the favourable option for particle and cell handling, thus the main scope of this thesis. Acoustophoretic techniques are used to manipulate particles within batch process systems to achieve separation and concentration of suspended particles as required for sample preparation. Furthermore, optimisation of an acoustic resonator in air is carried out as a building block of an acoustic trapping microgripper to selectively inspect and transport individual particles (i.e. batch process platform) via a non-contact approach.

1.2.1 Chapter 2: Background, Theory and Fabrication

In Chapter 2, a thorough literature review and the background theory on microfluidic particle manipulation and more specifically acoustophoretic particle manipulation is done. An in-depth discussion of the relevant background theory of acoustic manipulation along with a brief overview of the fabrication methods used throughout this thesis is included.

1.2.2 Chapter 3: Separation of particles using acoustic streaming and radiation forces in an open microfluidic channel

In this chapter (Chapter 3), a batch process system is developed to perform particle separation and collection using bulk acoustic waves (BAW) excitation. Particles of two distinct sizes (3 μm and 10 μm) are succesfully separated using two different forcing mechanisms simultaneously, namely, acoustic radiation forces (ARF) and acoustic streaming induced

drag forces. Previously, Rogers et al [44] successfully separated 6 μm and 31 μm particles using a similar approach. A deeper understanding of the system lead to new techniques being implemented considering factors that further improve separation efficiency. This system, not only demonstrates an improvement in the size ratio from 5.16 to 3.33 but with a high purity of 99% 3 μm particles from 10 μm particles. The separated particles can be easily removed with the use of a micro-sampling pipette (capillary force; i.e. passive extraction method) as it is an open system. Furthermore, finite element modelling is carried out to describe the physics of the system. The computational modelling suggests the potential ability to tune the system in order to separate particles of different sizes by scaling the size of the system. Publication of results [31] from this study is included in this thesis chapter.

1.2.3 Chapter 4: Batch Process Particle Separation using Surface acoustic waves (SAW)

Here, in Chapter 4 an extension to batch-wise size-deterministic separation methods is demonstrated using surface acoustic waves (SAW) as the excitation mechanism. The system developed for the first time, utilises a combination of standing surface acoustic wave (SSAW) and travelling surface acoustic waves (TSAW) to achieve selective particle separation based on particle size. The use of SAW allows for higher frequencies to be used as opposed to BAW, hence, pushing the fluid wavelength (λ_f) towards the size of the particle. The combination of both forcing mechanism that scales differently to particle radius, r (i.e. $F_{TSAW} \propto r^6$ [45] and $F_{SSAW} \propto r^3$ [46]) allows for deterministic particle sorting as the relative importance of each mechanism is size dependent. Furthermore, a sweep over a range of frequencies in a cyclical manner enhances the effect of the TSAW dominated particles (i.e. larger particles). In addition to that, the sweep of frequencies allows for the motion of SSAW dominated particles (i.e. smaller particles) beyond one wavelength, thus resulting in the collection of particles in a smaller region leading to an enhanced separation efficiency. Finite element analysis is carried out to help explain the size deterministic nature of this mechanism and therefore leading to the tunability of the system to separate particles of various sizes by changing the frequency range of excitation. As the frequency, f is increased, the apparent particle size, a (i.e. $a = r/\lambda_f$) increases as well, therefore shifting the dominant forcing mechanism from SSAW to TSAW. Publication of the results is included in this chapter demonstrating the separation of two sets of particles from each other. Experiments show the separation of 7 μm from 5.1 μm particles and 5.1 μm from 3.1 μm particles respectively by changing the frequency range of excitation. A manuscript on this work has been submitted for review and is included in this thesis chapter.

1.2.4 Chapter 5: Optimisation of an acoustic resonator for particle manipulation in air

This chapter (Chapter 5) will discuss the optimisation of an acoustic resonator for particle manipulation for operation in air. The use of acoustics to handle delicate synthetic and biological particles is highly desirable as it does not damage the sample when exposed to an extended period of excitation. Therefore, here a microgripper is proposed to manually manipulate micron-sized (order of 10^{-6} m) particles individually to allow for bath-wise examination. Previous studies have been conducted levitating relatively large (order of 10^{-3} m) droplets [47,48] and objects. [49,50] However, to achieve individual micron-sized particle manipulation, an increase in the frequency of excitation form the low kHz range (i.e. typically used currently) to the high kHz and even MHz range is required. Thus further consideration of attenuation (i.e. loss of acoustic energy) in air should be considered as it exhibits an exponential relationship with frequency. To address this, optimisation of a layered resonator design (thickness of individual layers and material properties) along with careful consideration of the frequency of operation was conducted. Finite element and numerical modelling was utilised to aid the design of the layered acoustic resonator. Furthermore, consideration of acoustic attenuation as a function of frequency indicates an optimal operational range that is found to be also dependent on the size of the transducer, therefore, allowing for the ability to tune the system. Publication of results [32] included in this chapter propose a method to obtain an optimum frequency of excitation which is size dependent. In addition, numerical analysis suggests that the optimal thickness of the piezoelectric layer (Pz26 used in experiments) should be $\approx 0.254\lambda_{PZT}$ together with a matching layer thickness $\approx 0.5\lambda_{ML}$ for relatively high acoustic impedance materials. It was also found, when relatively high acoustic impedance materials are used, the selection of material becomes less significant but individual layer thickness still play a major role in transmitting the maximum acoustic energy into the air gap. Based on the knowledge obtained from the finite element and numerical analysis, a layered resonator was fabricated, which lead to the successful trapping of solid micron-sized (83 μm and 14 μm) particles individually. Levitation and trapping of individual particles at these size scales has not been performed before. A method to optimise an acoustic resonator serves as an important building block to a complete 3-dimensional (3D) acoustic trapping microgripper that can be used to examine and transport individual micron sized particles.

1.2.5 Chapter 6: Conclusion and Future Work

Chapter 6, a summary of the contribution to the field of batch process analysis platforms using acoustofluidic principles by the research presented in this thesis is discussed. Finally, suggested future work to be carried out along with further potential contributions to the field of microfluidics and more specifically acoustofluidics in the future is presented.

Chapter 2

Background, Theory and Fabrication

2.1 Lab on a Chip

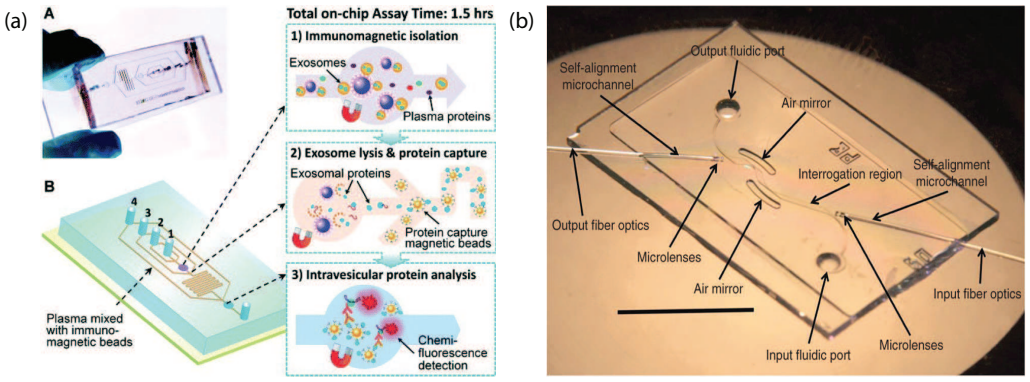

Figure 2.1: Typical Lab on a Chip (LOC) systems (a) Integrated microfluidic exosome analysis directly from human plasma. Reproduced under a Creative Commons Attribution-Non Commercial 3.0 Unported Licence from [1] as published by The Royal Society of Chemistry. Copyright 2014. (b) Optical photograph of a completed photonic Lab on a Chip (PhLoC)(Scale bar= 1 cm). Reprinted by permission from Macmillan Publishers Ltd: Nature Protocols [2]), Copyright 2011.

Arguably, Manz et al [51] introduced and established the concept of miniaturized total chemical analysis systems (μTAS). Following that, companies were founded utilising these concepts for life science applications. Naturally, rapid prototyping enabled by borrowed technology from microelectronic fabrication processes, boosted academic research and gave birth to the terminology of Lab on a Chip (LOC). [52] The concept of LOC systems are based on replicating the performance of a complete diagnostic process conducted in a laboratory (as shown in Fig. 2.1) by integrating various miniaturised components that are significantly smaller than that of their typical bulkier, full scale counterpart. The effect of scaling down the size, many essential parameters are relatively enhanced, therefore increasing its robustness significantly. Although, primarily, LOC systems are utilised for diagnostic purposes, the concepts are transferable to a wide range of other applications as well. The early involvement of industry, foreseeing a new industrial sector based on μTAS,

helped create a synergy between industry and academia that reinforced the expansion of practical applications. [53] Over the last couple of decades, LOC based devices have demonstrated its immense potential and benefits for many applications, such as point-of-care diagnostics, [54–57] analytical chemistry, [5, 58–60] cell culture, [3] environmental monitoring, [7, 42, 61, 62] genomic research [63–65] and pharmaceutical drug development. [66–68] There are various benefits that arise from LOC type technologies and platforms, to name a few,

- Handling of small sample volumes and reduced wastage
  - Diagnostic assays can shift from using hundreds of microliters of reagents to nanoliter volumes as a direct result of microfabricated arrays
  - Smaller quantity of sample is required to perform a similar analysis
- Reduction in processing time, thus, fast turnaround time
  - Integration of multiple steps speeds up analysis time and reduction of labor associated with the need to transfer sample
  - Small distances and volumes increase reaction times significantly
- Reduced operational and production costs
  - Reduction in production time
  - Reduced consumption of costly reagents by a factor of 10^3-10^4 [53]
  - Manufacturing cost can be significantly reduced enabled by mass-fabrication process technology allowing for disposable chips
- Increased sensitivity
  - Scaling down increases the sensitivity of systems as a result of favourable enhancement of parameters

A typical LOC is comprised of multiple components such as pumps, [69] valves, [70] mixers, [71, 72] sorters, [73] reactors [6, 74] and sensors. [75] Particle and/or cell separation and concentration is a fundamental procedure that is required by many biological and industrial processes. This is generally achieved in a continuous throughput manner using multiple different techniques. Many of these devices are developed to exploit the favourable physics at these size scales and operate using the principle of balancing drag forces induced by the fluid flow and an external forcing field such as magnetic, [76, 77] optical, [78, 79] electrical (dielectrophoresis (DEP)), [80–82] acoustophoretic, [83–86] and even using the force induced by the flow profile of the fluid itself. [87, 88] Each method mentioned above (discussed more in-depth in Section 2.1.2) applies a different force on the particle depending on their size, shape, electric and or mechanical properties, thus resulting in different particle spatial behaviour. This leads to selective particle separation and handling without the need of a contact approach, which can damage sensitive and fragile particles and cells. However, these continuous throughput devices require externally generated continuous flow, conventionally using a pump which in turn limits the practicality and versatility of deploying these methods in an out of laboratory setting.

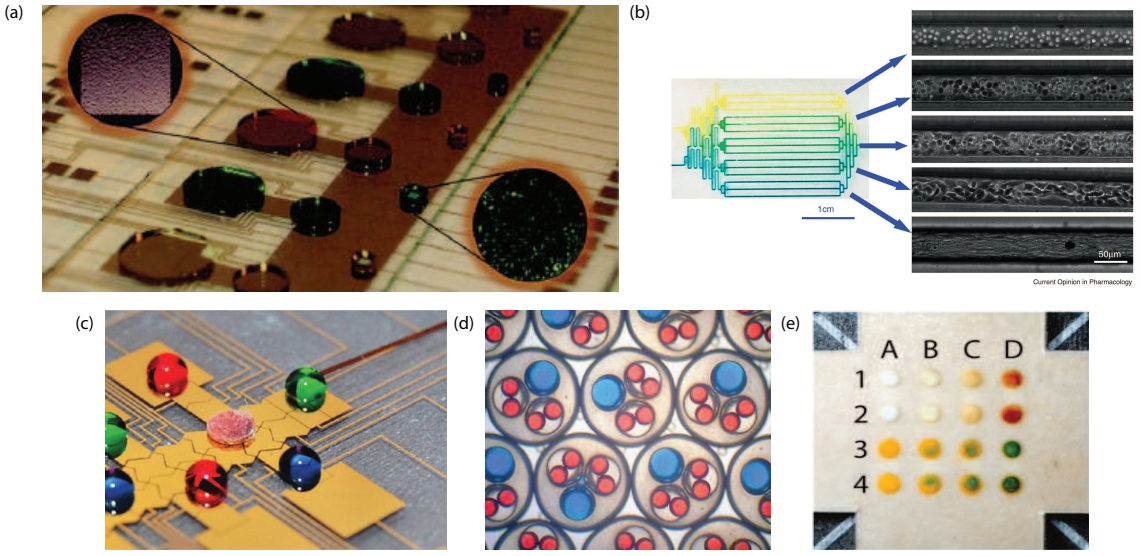

Figure 2.2: Examples of microfluidics based systems (a) Digital microfluidic platform developed for complete mamalian cell culture. Reproduced in part from [3] with permission of The Royal Society of Chemistry. (b) A microfluidic organ-on-a-chip for tissue culture. The top view of the device (left) shows an array of parallel microfluidic channels, which can be loaded with different cells, growth factors, or drugs (here visualized with different food dyes). The phase contrast images on the right exemplify the results of different cell culture conditions (rat cardiofibroblasts) on the same chip. Reprinted from [4] Copyright 2013, with permission from Elsevier. (c) Dried blood spot analysis by digital microfluidics coupled to nanoelectrospray ionization mass spectrometry. Reprinted with permission from [5]. Copyright 2012 American Chemical Society. (d) Optical micrograph of monodisperse sextuple component triple emulsions containing one W/O single emulsion and two O/W/O double emulsions (O:Oil;W:Water). Reproduced in part from [6] with permission of The Royal Society of Chemistry. (e) An example of a paper based microfluidic chip; a three-dimensional μPADs for running parallel assays and standards. Here used to analyse different samples of artificial urine. Reproduced from [7].Copyright 2008 National Academy of Sciences, USA.

Furthermore, when posed with the problem of extremely scarce supply of sample quantity, microfluidics enables another solution in the form of batch processing micro-liter (μL) scale samples. Batch process as the name implies allows batch wise examination and sample preparation without the need of large sample quantities as required by conventional laboratory procedures and even continuous flow microfluidic systems, thus rendering alternative choices impractical. In addition, it increases the diagnostic detection efficacy which is important in biological processes. [89–91] The small quantities required is as a direct result of the significant reduction in dead space within microfluidic chambers dictated only by the design size and limitations of the system as well as fabrication techniques available. These systems also allow for the added benefit of capillary filling as opposed to pumping mechanisms required to drive fluid through continuous systems, which further increase energy requirements and dead space volume. Adding to the reduction in additional components (i.e. pumps) and reduced sample volumes, batch processes further reduce the consumption of costly reagents, time investment and lower operational costs. Despite the overwhelming necessity and advantages posed by batch process analysis techniques, there

have been comparatively few studies conducted for particle separation within static fluid systems (i.e. small fraction of publications involving microfluidics; see Fig. 1.1) . Therefore, there is a huge need to exploit the benefits that emerge with the use of this highly practical analysis platform for a variety of different biological and industrial applications. Majority of medical diagnostic techniques is in essence a batch process, in that individual samples are handled in small batches separately, thus, the main scope of this thesis.

2.1.1 Scaling effects

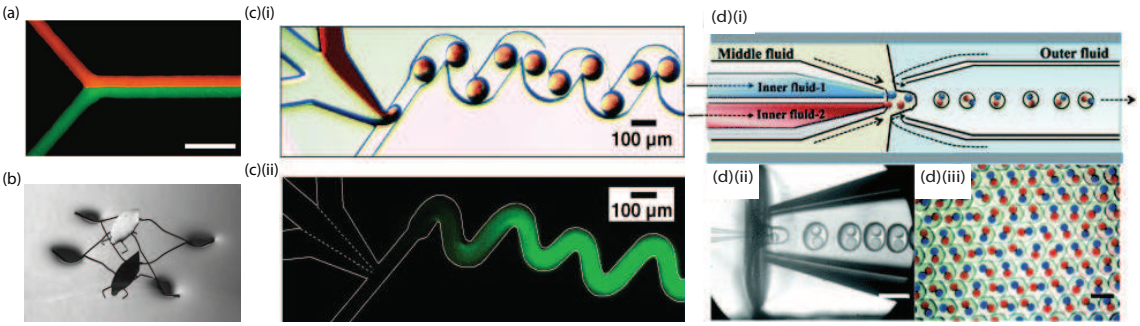

Figure 2.3: Examples of phenomena observed when the characteristic length scales are reduced. (a) Two fluids (i.e. red and green) do not mix in a straight channel due to low Reynolds number (Re=30.6)(Scale bar=0.5 mm). Reprinted by permission from Macmillan Publishers Ltd: Nature Materials [8], copyright 2003. (b) A metallic model "pond skater" (body length 28 mm) standing on a water surface due to relatively in high surface tension (i.e. low Weber number). Reproduced with permission from WILEY [9], copyright 2007. (c) Rapid mixing in droplets by chaotic advection (i) bright-field and (ii) fluorescence microscopy images of plugs moving through winding channels. Reprinted with permission from [10]. Copyright 2003, AIP Publishing LLC. (d)(i) Schematic of a microfluidic capillary device for preparation of multiple component double emulsions using a single-step emulsification making use of the low Weber number of the system. ((ii) and (iii)) Optical microscopy images showing double emulsion generation and monodisperse double emulsions with two different inner drops, one red and one blue. Reproduced in part from [11] with permission of The Royal Society of Chemistry.

LOC and other microfluidic systems mainly derive their advantages as a result of operating at very small scales which offers a range of benefits. By scaling down the size of these systems to the size scale of the analyte (i.e. cells, large biomolecules, synthetic particles, etc.), it opens up the possibility of utilising different forces and effects to manipulate these samples, which would otherwise be inapplicable. [92] For example, near-field electrical [80] and optical [93] methods would only be able to operate at these size scales to perform individualised particle/cell manipulation on demand. Naturally, early effort in miniaturisation of laboratory procedures consisted of replicating conventional methods, which can be overly complex and not as effective when scaled down, such as centrifugation.

To capture some of the advantages of reduced system size (i.e. the closeness of length scales to the size of particles/cells), manipulation methods are required. The techniques

best suited to the task may well differ to those used at the macro scale due to scaling effects. Therefore, the difference in physics between conventional macro systems and a micro-system should be considered while designing these systems. As a result, exploitation of the different length scales, L within microfluidic systems lead a to variety of interesting phenomena and thus different techniques.

Here, we look at pertinent dimensionless numbers and the effects of scaling the length scales, L.

Reynolds number

The Reynolds number, Re is a dimensionless term that relates inertial to viscous forces and thus, a good description of the relative dominance the forces experienced. It is given by,

$$Re = \frac{\rho U L}{\mu} \tag{2.1}$$

where, ρ, U, and μ are the density, characteristic velocity and the viscosity of the fluid.
As L is decreased, viscous terms become more dominant and as a result, flow is generally in the laminar regime (i.e. very low Re; see Fig. 2.3 (a)). Therefore, issues arising from mixing of fluids is eradicated, giving rise to high controllability of fluid flow without experiencing cross contamination.

Weber number

The Weber number, We is the non-dimensional number that characterises a two-phase flow where an interface between the different phases are is present. It shows the relative importance of inertial to surface forces and is given by,

$$We = \frac{\rho U^2 L}{\gamma} \tag{2.2}$$

where, γ is the surface tension of the interface considered.
Based on Eqn. 2.2, we observe that when L is reduced, the interfacial surface forces become relatively more dominant. As a result, exploitation of these relatively dominant forces (see Fig. 2.3 (c)(i) and (d)) can be used to realise mini bio-reactors within multiple emulsions. [6]

Péclet number

The Péclet number, Pe is the dimensionless number that dictates the relative importance of convection to diffusion. Pe is given as

$$Pe = \frac{UL}{D} \tag{2.3}$$

where, D is the diffusion constant.
Eqn. 2.3 dictates the advective transport rate in comparison to the diffusive transport rate. As L is decreased, the diffusive rate becomes relatively more dominant. This is shown by re-arranging the diffusion length equation,

$$L = \sqrt{2D\tau} \tag{2.4}$$

$$\tau = \frac{L^2}{2D} \tag{2.5}$$

where, τ is the diffusion time.

Capillary Number

The relative effects of viscous forces to surface tension that acts across an interface of two different mediums is given by the Capillary number, Ca. It is defined as:

$$Ca = \frac{\mu U}{\gamma} \tag{2.6}$$

where, μ, U and γ is the dynamic viscosity of the liquid, the characteristic velocity and the surface tension of the fluid.
Although, the Capillary number is independent of the characteristic length, L it is a very important parameter in microfluidic systems. This is due to the fact that the characteristic velocity, U of these systems are generally very small.

Physcical Quantity	**Scaling Law**
Intermolecular Van der Waals Force	L^{-7}
Density of Van der Waals Forces between interfaces	L^{-3}
Time	L^0
Capillary Forces	L^1
Distance	L^1
Flow Velocity	L^1
Thermal power transferred by conduction	L^1
Electrostatic Force	L^2
Diffusion time	L^2
Volume	L^3
Mass	L^3
Gravitational Force	L^3
Electrical Motive Power	L^3
Magnetic force with an exterior field	L^3
Magnetic force without an exterior field	L^4
Centrifugal Force	L^4

Table 2.1: Other physical quantities may need consideration when designing micro/nanofluidic systems. [30]

Consideration of the physical quantities shown in Table 2.1 along with the dimensionless numbers introduced in Section 2.1.1 help design better, more practical microfluidic systems. For instance, the effect of reducing the characteristic length, L reduces the Reynolds number as discussed in Eqn. 2.1 leads to minimal fluidic mixing (see Fig. 2.3 (a))). While this naturally occurring phenomenon is favourable in many instances such as passively isolating different species of fluids (i.e. samples and reagents), controlled and known migration of particles arising from fluid drag forces, reduced cross contamination of samples and ease of inspecting pre-focussed particulate matter within fluid streams, it is sometimes required to very quickly mix two fluid species together with a high degree of control over mixing region and time. To achieve this, inspection of the Péclet number (see Eqn. 2.3) allows us to develop highly predictable diffusion based microfluidic mixers. [94–97]

Furthermore, the exploitation of high capillary forces allows us to substitute certain external pumping mechanisms. The use of capillary based filling via wicking has lead to the branch of microfluidics known as "*paper microfluidics*". [7,98,99] Similarly, the difficulty in delivering discrete volumes at the micro/nanoliter scales poses another issue. However, relatively high surface tension denoted by the Weber number (see Eqn. 2.2) and Capillary number (see Eqn. 2.6) allows discrete droplets of fluids to be delivered into the system and manipulated in a highly controllable manner. [66,100,101]

2.1.2 Actuation Methods

The ability to manipulate suspended matter (i.e. particles/cells) and fluids on-demand within these LOC systems are highly desirable. The requirement of active control on-chip, stimulated the development of multiple different actuation methods that can be implemented within microfluidics LOC systems. From an engineering perspective, the need to replicate the results of the macro-scale conventional laboratory equipment is of a large interest. The effect of scaling down the size of these systems means alternative new methods yield more feasible platforms, as the dominant forces have now been altered. Methods such as optical, magnetic, electrical and ultrasonics are highly applicable at these length scales as they have relatively strong near-field effects that render them impractical over larger scales as the force magnitude decays quickly as a function of increasing length scales. Majority of the forces mentioned are non-contact forces thus allowing for external actuation and therefore, can be isolated from the fluid channels. As a result of isolating the force generators, suspended matter along with the medium its in, would would not be in physical contact with potentially harmful or reactive circuitry and materials, increasing the robustness of these systems.

Manipulation within LOC platforms has been well studied over the past decades and have demonstrated a wide variety of highly applicable processes, including concentration, [82,102,103] particle sorting, [44,78,85,104–106] mixing, [25,107–109] cell patterning and culturing [26,110,111] and cell lysis. [112,113] There are a wide range of techniques

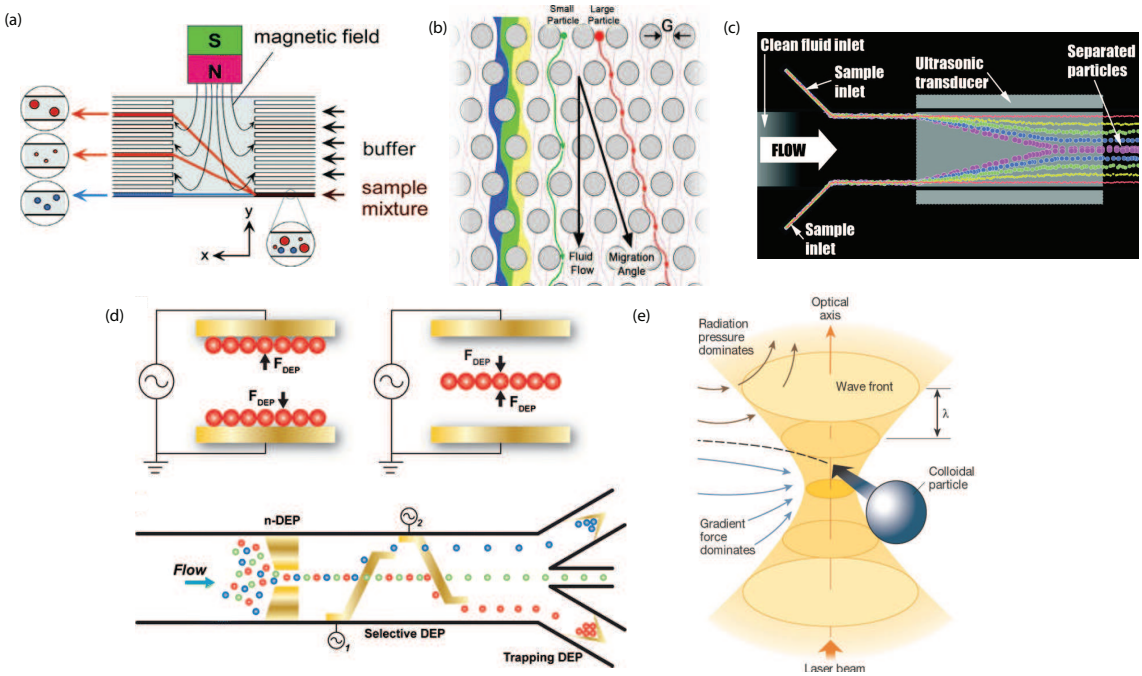

Figure 2.4: Schematics exhibiting examples of actuation methods used for particle sorting within microfluidic systems. (a) The use of magnetophoresis to selectively sort particles based on their magnetic properties. Reprinted with permission from [12]. Copyright 2004 American Chemical Society. (b) Passive sorting method using hydrodynamic forces, whereby deterministic lateral displacement technology is used to separate particles based on size. Reprinted with permission from [13]. Copyright 2009, AIP Publishing LLC. (c) Acoustophoresis used to separate particle based on their mechanical properties and size using acoustics. Reprinted with permission from [14]. Copyright 2007 American Chemical Society. (d) The use of electrical actuation, specifically dielectrophoresis (DEP) to selectively sort particles based on their dielectric properties using an A/C signal. Reproduced under the Creative Commons Attribution Noncommercial License from [15]. (e) High intensity lasers known as optical tweezers used to manipulate single particles with a non-invasive method. Reprinted by permission from Macmillan Publishers Ltd: Nature [16], copyright 2003.

and actuation methods that can be utilised to perform these tasks. Although, there are numerous different methods that can be employed, the optimum method depends heavily on the procedure or task at hand. Therefore, the chosen technique to be employed would depend on the advantage and disadvantages of each particular method available. Factors that should be considered when choosing to employ a certain technique are throughput requirements, force magnitude, force localisation ability, flexibility of the system, ease of integration and as well as the economic aspect associated with fabrication and assembly costs. In the following subsections, different potential actuation methods are described in more detail.

Magnetic

The control of particle motion under the influence of an external magnetic field is termed "magnetophoresis". [114] The appealing aspect of magnetic control of particles is its inexpensive and gentle cell/biological separation nature. [115] When applied by an external magnetic field, natural or induced paramagnetic species within the sample or individual cells leads to selective sorting or separation as a result of interaction with the field. Therefore, magnetic cell separation allows for desirable features such as high specificity and sensitivity. In a scenario whereby inherent magnetic properties are non-existent, magnetic labelling can be carried out by attaching magnetic particles to the cell surface [116] or by inserting nanoparticles within the cell. [117] The effective force that acts on a suspended particle within a magnetic field is given by, [115]

$$\begin{aligned} \mathbf{F_{eff}} &= \mathbf{F_p} - \mathbf{F_f} \\ &= \chi_p V H \frac{dB}{d\mathbf{r}} - \chi_f V H \frac{dB}{d\mathbf{r}} \\ &= (\chi_p - \chi_f) V H \frac{dB}{d\mathbf{r}} \\ &= \Delta\chi V H \frac{dB}{d\mathbf{r}} \end{aligned} \tag{2.7}$$

where, subscripts "p" and "f" denote particle and suspended medium respectively. V is the particle volume χ_p and χ_f volume magnetic susceptibility of the particle and suspending fluid respectively. In addition, H and B are the applied and local magentic field respectively. The relationship between H and B is given by,

$$\mathbf{B} = \mu_0 \mathbf{H} \tag{2.8}$$

where $\mu_0 = 4\pi \times 10^{-7}$ T m A^{-1} is the magnetic permeability of free space.

Magnetophoresis has demonstrated particle sorting for medical diagnostics in a on-chip continuous free flow system, [118] cell manipulation using nanowires, [119] to move and control drops (containing low concentration of paramagnetic particles) on a superhydrophobic surface, [120] and for detection of magnetically labelled cells [114] to name a few examples.

Although the use of magnetophoresis offers many advantages, there are certain limitations that is associated with this technique. Disadvantages includes the need for existing or the addition of magnetic species, high susceptibility of the throughput rate and relatively weak forces in applications of interest.

Optical

The use of high intensity laser beams that induce a high potential gradient leads to the development of optical tweezers first introduced by Ashkin *et al*, [121] which provide means

of a non-invasive dynamic control of very small particles (size range: 10s of nm to 10s of μm) such as bacteria, viruses and motor molecules. [122] A highly focused laser beam is created using a high numerical aperture microscope objective. Objects that are dielectric in nature are attracted to the focal point where the photon energy is at a maximum. Momentum transfer from the photon to the object (i.e. particle) as a result of refraction that occurs at the boundary of the particle and surrounding medium gives rise to a radiation pressure, which is in accordance to the law of conservation of momentum.

Light can be considered as a series of photons propagating through a medium due to its electromagnetic wave nature. As a result, each photon has a momentum as given by,

$$P_{mom} = \frac{h_P}{\lambda_{light}} \tag{2.9}$$

where, P_{mom} is momentum, h_P is Planck's constant and λ_{light} is the wavelength of light.

For simplicity sake, we consider a spherical particle, with a diameter D. If D is larger than or close to that of λ_{light} it is said to be in the Mie regime and conversely, when D is much smaller than λ_{light}, it is in the Rayleigh regime (relatively independent of the particle shape). [122] Depending on the size of the particle, the forces exerted on these particles differ and as a result the formulation differs as well due to the nature of electromagnetic scattering.

For a case where $D \ll \lambda_{light}$, the Rayleigh regime particle experiences a scattering force given by, [121]

$$F_{scattering} = n_m \frac{\sigma \langle S \rangle}{c} \tag{2.10}$$

where, n_m is the refractive index of the surrounding medium, $\langle S \rangle$ is the time-averaged Poynting vector, c is the speed of light and σ is the particle's cross-section.

$$\sigma = \frac{8}{3}\pi (kr)^4 r^2 \left(\frac{n^2 - 1}{n^2 + 2} \right)^2 \tag{2.11}$$

r is the particle's radius, n the refractive index of the particle and k the wave vector of the light used.
and a gradient force given by,

$$F_{gradient} = \frac{1}{2 n_m \epsilon_0 c} \alpha \nabla I(\vec{r}) \tag{2.12}$$

where, α is the polarizability and I is the light intensity.

Conversely, if a particle is larger or close to λ_{light} (i.e. $D \geqslant \lambda_{light}$), the scattering force is given by, [122]

$$F_{scattering} = \frac{n_m P_{ray}}{c}\left\{1 + R\cos(2\theta_i) - \frac{T^2[\cos(2\theta_i - 2\theta_r) + R\cos(2\theta_i)]}{1 + R^2 + 2R\cos(2\theta_r)}\right\} \tag{2.13}$$

and the gradient force by,

$$F_{gradient} = \frac{n_m P_{ray}}{c}\left\{R\sin(2\theta_i) - \frac{T^2[\sin(2\theta_i - 2\theta_r) + R\sin(2\theta_i)]}{1 + R^2 + 2R\cos(2\theta_r)}\right\} \tag{2.14}$$

where, P_{ray} is the power for a single ray, $R_{Fresnel}$ and $T_{Fresnel}$ is the Fresnel reflection and transmission coefficients respectively; θ_i and θ_r is the incident and refraction angle.

The Fresnel coefficients are given by,

$$\begin{gathered} R_{Fresnel} = \frac{1}{2}\left\{\left(\frac{\tan(\theta_i - \theta_r)}{\tan(\theta_i + \theta_r)}\right)^2 + \left(\frac{\sin(\theta_i - \theta_r)}{\sin(\theta_i + \theta_r)}\right)^2\right\} \\ \text{and} \\ T_{Fresnel} = 1 - R_{Fresnel} \end{gathered} \tag{2.15}$$

For a particle to pulled towards the focal point, the gradient force, $F_{gradient}$ has to be dominant over the scattering force, $F_{scattering}$.

Using optical tweezers, studies have shown individualised particle manipulation, [123] sorting of biologicals, [79] sorting within a reconfigurable three-dimensional optical lattice, [78] and mechanical characterization of red blood cells. [124]

However, despite the overwhelming advantages offered using optical tweezers, low throughput as particles/ cells are individually manipulated, cell damage due to high intensity laser beams, expensive and difficult implementation as complex instrumentation are required, sensitive integration pose drawbacks that reduce the robustness of this method.

Electrical

When a particle subjected to and interacts with an electric field, it experiences a lateral force. [125] For particle manipulation, dielectrophoresis (DEP) [126] is a common electrical technique utilised. As a result of a dielectric polarization induced in a suspended particle within an alternating electrical field, $\mathbf{E}$ with spatial inhomogeneities (i.e. $\nabla\bar{\mathbf{E}} \neq 0$), it experiences a non-zero force when time-averaged. This non-zero time-averaged force is given by, [81, 126]

$$\langle F_{DEP}\rangle = 2\pi r^3 \epsilon_m K\left(\epsilon_p, \epsilon_m, \omega\right)\nabla(\mathbf{E}\cdot\mathbf{E}) \tag{2.16}$$

where, r is the particle radius, $\epsilon_m$andϵ_p are the complex permitivities of the particle and medium respectively; whereas $K\left(\epsilon_p, \epsilon_m, \omega\right)$ is the frequency dependent Clausius-Mossotti factor given by,

$$K\left(\epsilon_p, \epsilon_m, \omega\right) = \frac{\epsilon_p(\omega) - \epsilon_m(\omega)}{\epsilon_p(\omega) + 2\epsilon_m(\omega)} \tag{2.17}$$

where ω is the angular frequency.

DEP is a popular option amongst the available actuation methods within microfluidic systems due to its capability to be integrated with high-throughput systems. However, DEP based systems have severe drawbacks in the form of localised heating and high voltage requirements as a result of relatively low forces, which in turn can be damaging to the cells and biologicals within the sample.

Passive

Passive methods of cell or particle separation rely heavily on carefully designed geometry and internal forces to achieve sorting. [88] Multiple different passive techniques are available to sort particle such as, adhesion based methods, [127] pinched flow fractionation (PFF), [87,128,129] field flow fractionation (FFF), [130] hydrodynamic filtration (HDF), [131, 132] biomimetic separation [133–135] and with the use of physical obstructions within the flow field by introducing pillars, [88, 136] weirs [105] and other objects. Utilisation of pillars to impede and divert the flow into different streamlines, introducing a set of distinct outcomes and is a common particle separation technology known as deterministic lateral displacement (DLD). DLD facilitates particle sorting based on size utilising a specific arrangement of pillars throughout the channel. The arrangement of pillars dictate the critical particle diameter that can be separated (i.e. separation between particles larger from particles that are smaller than that of the critical diameter).

The majority of these passive methods rely on the laminar flow regime (i.e. low Re number) which is dictated by the dominant viscous effects that is present in most microfluidic devices as discussed in Section 2.1.1. As a result, if we consider the incompressible Navier-Stokes equation we have,

$$\rho\left(\frac{\partial v}{\partial t} + v \cdot \nabla v\right) = -\nabla p + \eta \nabla^2 v \tag{2.18}$$

where, ρ, v, p and η refer to the fluid density, velocity, pressure and viscosity respectively. Since, inertial effects are negligible due to the viscous dominant nature of microfluidic systems, we disregard the $(v.\nabla v)$ non-linear term. The equation is now reduced yielding the Stokes equation,

$$\rho\frac{\partial v}{\partial t} = -\nabla p + \eta \nabla^2 v \tag{2.19}$$

Consideration of the fluidic hydrodynamic resistance, R_{hyd}, the flow rate, Q, the Re and Pe number is essential in designing a passive system to achieve particle sorting.

For a pressure driven flow, the relationship between the flow rate and the hydraulic resistance is given by,

$$Q = \frac{\Delta p}{R_{hyd}} \tag{2.20}$$

where, Δp is the pressure difference along the channel. For a simple rectangular microchannel with width (w), height(h) and length (l), the hydraulic resistance is given by,

$$R_{hyd} = \frac{12\eta l}{wh^3} \tag{2.21}$$

It should be noted, the hydraulic resistance differs depending on shape and size. These formulations can be found in various fluid dynamics textbooks.

The benefit of using this technique is that implementation is simple, cheap and has a high throughput, making it a popular choice. However, passive methods rely heavily on channel designs, particle size and shape. As a result, passive systems generally lack robustness, as these systems cannot be altered between each run, thus, lacking tunability. Furthermore, it often encounters problems associated with channel clogging especially when employed within deterministic lateral displacement (DLD) systems.

Acoustic

Acoustic actuation is used as the preferred method for particle sorting throughout this thesis owing to the advantages and versatility offered utilising this technique. The use of acoustic actuation along with a detailed literature review within microfluidic systems will be discussed in-depth in Section 2.2.

Comparison

Although each one of the techniques discussed in this section has a vast number of benefits, limitations dictate which method is most suitable for a particular task. Therefore, techniques such as the passive methods discussed, lacks tunability and require a high degree of modulation of the flow rate and on chip gating. Thus, the potential use of this technique in microfluidic sorting would be limited to only a distinct set of samples. In addition, techniques such as the electrical and magnetic methods rely heavily on the complex electrical permittivity difference ($\Delta\epsilon$) and relative magnetic susceptibility ($\Delta\chi$). Despite optical tweezers offering a high degree of control of individualised non-invasive particle transport, this technique along with the electrical methods, have the potential of damaging cells or biological particulate as a result of localised heating associated with these approaches. On the other hand, although acoustic manipulation has drawbacks in the form of integration difficulties and a comparatively high lower size limit of particles that can be manipulated, though, it has been shown to not yield cell damage over a prolonged period of exposure [110, 137] which is highly desirable.

With the recent use of surface acoustic waves (SAW) in microfluidic devices, the ability to increase the excitation frequencies, therefore, reducing the lower particle size limit that can be manipulated and ease of integration onto a chip, open up the prospect of overcoming some key drawbacks posed by using acoustic actuation. Furthermore, acoustics has demonstrated its versatility when applied in microfluidic systems. These applications vary from mixing, [109] concentration, [138] atomization, [139] pumping, [140] droplet production, [66] and sorting. [141]

2.2 Acoustics and Acoustofluidics

Acoustics is the study of sound wave propagation within a medium (i.e. gas, liquid or solid). Sounds waves are essentially mechanical pressure waves that propagate through a medium with a certain amplitude (i.e. pressure level) and frequency (i.e. pitch). The application of acoustics are prominent in almost every aspect of a modern society, providing building blocks for systems addressing tasks such as noise control, musical acoustics, acoustic signal processing, bio-acoustic, sonar and various other devices. Ultrasound or ultrasonics is a subset of acoustics that has no distinct difference in physical properties as compared to that of audible sound with the exception of its frequency range. Frequencies of sounds that exceed 20 kHz (i.e. above the audible range of a healthy, young adult) is characterised as ultrasound. Applications of ultrasound are vast just like its lower frequency counterpart being implemented in various systems such as acoustic microscopy, non-destructive testing (NDT), medical ultrasound, sonography, ultrasonic cleaning, sonochemistry and ultrasonic particle manipulation and characterisation. Ultrasonic particle manipulation and characterisation in microfluidic systems falls under the study which is generally known today as acoustofluidics.

"Acoustofluidics" is the term given to the study of acoustic based manipulation or forcing of particles within microfluidic systems. [24] The gentle nature of this actuation method, depends purely on the particle's inherent mechanical properties to migrate particles based on the generated force fields, is an appealing option and therefore attracted attention of various research groups from around the world. Since its inception, acoustophoretic based devices have included microparticle filters, cell sorting, cell differentiation, food analysis and many more. Its dependence on various factors such as size, shape, density and compressibility gives rise to a robust and highly practical technique for cell or particle separation, thus the preferred method of actuation throughout this thesis.

Within acoustofluidics, there are a few key factors that need to be considered while designing these systems. Firstly, the consideration of energy dissipation in terms of attenuation is something that is generally overlooked when designing these liquid based microfluidic systems, as the path length of these propagating acoustic waves are minimal and therefore does not play a major role in the design process. However, when operating in an air based microfluidic system, attenuation (Section 2.2.1) is an important factor that needs to be considered, especially at high frequency (100s of kHz and MHz range) of operations. Furthermore, consideration of the forces (Section 2.2.2) that act upon a particle that is subjected to an acoustic field is essential in developing a system to perform a particular task. Finally, the use of piezoelectrics (Section 2.3) and excitation methods (Section 2.4) used in microfluidic systems is also discussed, as it provides techniques in establishing the desired acoustic fields for purposes of particle manipulation. These factors will be discussed in more detail within this chapter (Section 2.2 through to Section 2.4).

2.2.1 Attenuation

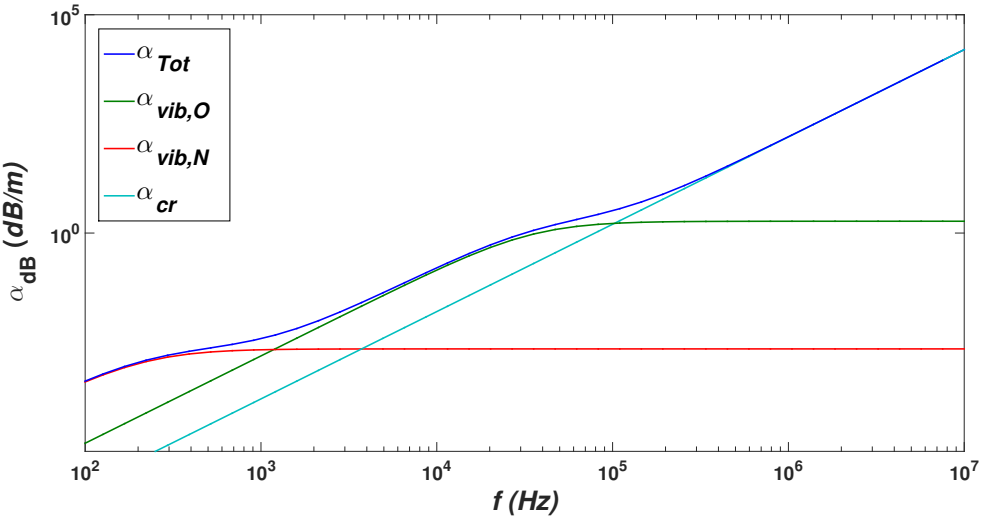

Figure 2.5: Plot of absorption coefficient, α_{dB} in air against frequency, f and its dependence on absorption by Nitrogen, N_2, Oxygen, O_2 and classical losses due to temperature, pressure and frequency. Relative humidity of 45 % at 20° C. Plot reproduced based on equations in [17]

Acoustic attenuation is the measure of energy loss of a propagating pressure wave within a medium. Although, acoustic attenuation is desirable in certain scenarios such as noise reduction (i.e. noise barriers and concert hall designs), it can pose a serious problem when energy retention is vital (i.e. minimal energy loss). Therefore, an understanding of acoustic attenuation and minimisation of energy dissipation is important in the design process, especially for high frequency microfluidic devices as shown in Fig 2.5. In this section, attenuation is discussed in the context of air based losses due to the nature of minimal influence within liquid based microfluidic devices. Knowledge of acoustic attenuation is used in designing an air based acoustic resonator as discussed in Chapter 5. It is shown that consideration of acoustic energy loss in terms of attenuation plays a major role in the design process for the mentioned application.

Theory

As a sound wave propagates through a fluid, absorption and scattering of the wave combined give rise to acoustic energy loss. This loss or attenuation level is assumed to be dominated by temperature of the propagating medium. [17] This decay in pressure level is found to be exponential and for a plane wave propagating over a distance, x is given by,

$$P_{aco}(x) = P_{aco,0}e^{-\alpha x} \tag{2.22}$$

where, P_{aco} is the acoustic pressure in *Pascals* (Pa), $P_{aco,0}$ is the initial pressure at $x = 0$ and the frequency dependent α is the attenuation coefficient in a particular medium, with

units Np.m^{-1}. Attenuation is generally expressed in *Nepers* (Np), which is a natural logarithmic unit that denotes the reduction in wave amplitude to 1/e of the initial amplitude. Attenuation is also described in terms of decibels and is given by,

$$\begin{aligned} \Delta PL &= 20\log\frac{P_{aco}}{P_{aco,0}} \\ &= 20\log e^{\alpha s} \\ &= -8.686\alpha s \end{aligned} \tag{2.23}$$

where,

$$\alpha_{dB} = 8.686\alpha \tag{2.24}$$

where the attenuation level, α_{dB} is in dB.m^{-1}

In the case, where the fluid medium is a homogeneous gaseous medium, absorption of energy from an ultrasonic wave in various gases such as CO_2, N_2 and H_2 has been studied. [142, 143] Subsequently, absorption in atmospheric air was investigated. [144–146] In the following years, comprehensive models were developed to accommodate more than just shear viscosity and thermal conductivity (i.e. classical absorption). Models considering vibrational, rotational and translational energies of gas molecules in atmospheric air was developed. [146]

There are two main forms of absorption losses. Firstly, in the form of classical losses associated with a conversion of kinetic energy of molecules into heat and secondly, relaxation losses due to the conversion of kinetic translational energy into the internal energy of the molecules internal energy itself. [17] Classical losses that is mainly due to the viscous and heat conduction losses, known as Stokes-Kirchhoff losses is given by,

$$\alpha_{cl} = 4.845 \times 10^{-8} \left(\frac{T/T_0}{T + 110.4}\right) f^2 \left(\frac{P_0}{P}\right) \quad \text{in} \quad \text{dB.m}^{-1} \tag{2.25}$$

where, T is the measured temperature, T_0 is the reference temperature (293.15 K), f is the frequency in Hz, P is the measured pressure and P_0 is the reference pressure (i.e. 101.325 kPa). Relaxation losses are due to two main factors, rotationally excited and vibrationally excited molecules. As the rotational absorption is also a function of temperature, pressure and frequency similar to that of classical losses, the two equations can be combined and written as,

$$\alpha_{cr} = 15.895 \times 10^{-11} \left(\frac{(T/T_0)^{\left(\frac{1}{2}\right)}}{(P/P_0)}\right) f^2 \quad \text{in} \quad \text{dB.m}^{-1} \tag{2.26}$$

The vibrational absorption component, however, depends on the particular constituents in the atmosphere in addition to temperature, pressure and frequency. As air is generally composed of four major components namely, oxygen (O), nitrogen (N), carbon dioxide (CO_2) and water vapour (H_2O). Furthermore, Bass *et al.* [145] showed that vibrational energy transfer reactions involving CO_2 can be ignored. Therefore, only the

interaction between nitrogen, oxygen and water vapour needs to be considered. The total acoustic absorption in atmospheric air can be expressed as sum as described by,

$$\alpha_{dB} = \alpha_{cr} + \alpha_{vib,O} + \alpha_{vib,N} \tag{2.27}$$

where $\alpha_{vib,O}$ and $\alpha_{vib,N}$ (in dB.m^{-1})are the vibrational absorption caused by oxygen and nitrogen respectively and is given by,

$$\alpha_{vib,O} = 1.110 \times 10^{-1} \frac{e^{-2239.1/T}}{f_{r,O} + \left(f^2/f_{r,O}\right)} \left(\frac{T_0}{T}\right)^{\left(\frac{5}{2}\right)} f^2 \tag{2.28}$$

$$\alpha_{vib,N} = 9.480 \times 10^{-1} \frac{e^{-3352.0/T}}{f_{r,N} + \left(f^2/f_{r,N}\right)} f^2 \tag{2.29}$$

where $f_{r,O}$ and $f_{r,N}$ are the maximum absorption frequencies (in Hz) for their respective gases and dependent on water vapour content. Their relationship is given by, [17]

$$f_{r,O} = \left(\frac{P}{P_0}\right) \left\{24 + \left(4.41 \times 10^4\right) h \left[12 \frac{(0.05 + h)}{(0.391 + h)}\right]\right\} \tag{2.30}$$

$$f_{r,N} = \left(\frac{P}{P_0}\right) (9 + 200h) \tag{2.31}$$

where, h is the molar concentration of water vapour in percent.

Based on Equations 2.22 and 2.27, the total absorption coefficient in atmospheric air and the total pressure level decay over a given length can be estimated for a given frequency, temperature and relative humidity to assist design of ultrasonic microfluidic air based systems. The consideration of acoustic energy loss in terms of attenuation lead to the finding of an optimum frequency of operation for a layered resonator design used for particle manipulation in air as discussed in Chapter 5.

2.2.2 Acoustic Forces

When a particle or droplet is suspended within a vibrating medium (i.e. fluid or gas), it experiences a non-linear force that produces a net movement of the object arising from the non-zero second order time-averaged terms, depending on its physical properties, the fluid medium and resultant pressure field. The presence of the particle within this vibrating fluid causes an exertion of three main types of forces, namely, acoustic radiation forces (ARF) [46,147,148], acoustic streaming induced drag forces [149–152] and Bjerknes forces [153,154]. Theses forces along with the formulations required will be discussed in detail, with the exception of Bjerknes forces. Discussion on Bjerknes forces are not included within this thesis as it does not play an integral role in the methods used to achieve particle manipulation within the developed systems discussed.

Acoustic Radiation Forces

By vibrating a fluid volume, a resultant pressure field is observed. As a result of introducing a particle within this fluid medium, a net force is experienced by the particle known as acoustic radiation force (ARF). There are three different scenarios that give rise to the resultant force, namely the interaction with the incident sound wave and the particle, the scattered sound wave off the particle and finally the sound wave within the particle due to transmittance. These inter-related scenarios affect the resultant pressure field which is highly dependent on the shape, size and physical properties of the particle itself. As these vibrations are oscillating at very high frequencies (i.e. kHz or MHz), we observe the time-averaged effects only. As the excited vibrations are harmonic oscillations, the first-order pressure and velocity terms time-average to a zero value as shown in Equation 2.33.

We let the $\langle X \rangle$ be the time-average over a full harmonic oscillation,

$$X = \sin(\omega t) \tag{2.32}$$

therefore,

$$\begin{aligned} \langle X \rangle &= \frac{1}{T_{osc}} \int_0^{T_{osc}} \sin(\omega t) dT_{osc} \\ &= 0 \end{aligned} \tag{2.33}$$

where, T_{osc} is the period of oscillation, t is time and ω is the angular frequency of oscillation.

However, the second-order time-averaged pressure term is a non-zero term as shown in Equation 2.35,

$$X^2 = \sin^2(\omega t) \tag{2.34}$$

therefore,

$$\begin{aligned} \langle X^2 \rangle &= \frac{1}{T_{osc}} \int_0^{T_{osc}} \sin^2(\omega t) dT \\ &= \frac{1}{T_{osc}} \int_0^{T_{osc}} \frac{1}{2} \left[1 - \cos\left(2\omega t\right)\right] dT_{osc} \\ &= \frac{1}{2} \end{aligned} \tag{2.35}$$

In order to obtain the second-order pressure and velocity fields, we need to find a relationship between the second-order and first-order terms. For simplicity, we assume a spherical sphere of a particular material property when deriving the equations that dictate the forces acting on the particle throughout this thesis. Therefore, we employ the perturbation theory to obtain the second-order governing equations in terms of the first-order pressure,P and velocity fluctuations,v. [155]

We let,

$$P = P_0 + P_1 + P_2 \tag{2.36a}$$

$$\rho = \rho_1 + \rho_2 + \rho_3 \tag{2.36b}$$

$$v = 0 + v_1 + v_2 \tag{2.36c}$$

where, $P_1 = \rho_1 c_0^2$ is given by the (isentropic) derivative $c_0^2 = (\partial P/\partial \rho)_s$. Subscripts 0, 1 and 2 denote the order of the expression (i.e. initial, first and second-order) and ρ is the density.

We also assume time-harmonic fields, thus,

$$P_1 = P_1(x)e^{i\omega t} \tag{2.37a}$$

$$\rho_1 = \rho_1(x)e^{i\omega t} \tag{2.37b}$$

$$v_1 = v_1(x)e^{i\omega t} \tag{2.37c}$$

It is also noted that, the physical real-valued time-average $\langle f \;\; g \rangle$ of two harmonically varying fields f and g that has complex components, as given by the real-part rule is

$$\langle f \;\; g \rangle = \frac{1}{2} Re\left[f(x) \;\; g^*(x) \right] \tag{2.38}$$

where, the asterisk denotes the complex conjugate.

Now, if we consider the thermodynamic equation of state by expressing P in terms of the density, ρ (Equation 2.39a) the continuity equation for density (Equation 2.39b) and the Navier-Stokes equation for the velocity field, v (Equation 2.39c) we have,

$$P = P(\rho) \tag{2.39a}$$

$$\frac{\partial \rho}{\partial t} = -\nabla \cdot (\rho v) \tag{2.39b}$$

$$\rho \frac{\partial v}{\partial t} = -\nabla P - \rho (v \cdot \nabla) v + \eta \nabla^2 v + \beta \eta \nabla (\nabla \cdot v) \tag{2.39c}$$

First-order terms of the governing equation in Equation 2.39b and 2.39c,

$$\frac{\partial \rho_1}{\partial t} = -\rho_0 \nabla \cdot v_1 \tag{2.40a}$$

$$\rho_0 \frac{\partial v_1}{\partial t} = -\nabla P_1 + v_1 \nabla \cdot \rho_0 v_1 + \eta \nabla^2 v_1 + \beta \eta \nabla (\nabla \cdot v_1) \tag{2.40b}$$

Second-order terms of the governing equation in Equation 2.39b and 2.39c,

$$\nabla \langle \rho_1 v_1 \rangle = -\rho_0 \nabla \cdot \langle v_2 \rangle \tag{2.41a}$$

$$\left\langle \rho_1 \frac{\partial v_1}{\partial t} \right\rangle + \rho_0 \langle (v_1 \cdot \nabla) v_1 \rangle = -\nabla \langle P_2 \rangle + \eta \nabla^2 \langle v_2 \rangle + \beta \eta \nabla (\nabla \cdot \langle v_2 \rangle) \tag{2.41b}$$

If we assume an inviscid fluid, as it is far from walls, (i.e.$> 5\delta_v$) therefore, $\eta \approx 0$ and can be neglected. The boundary layer thickness or viscous penetration depth, δ_v is given as, $\delta_v = \sqrt{\frac{2\nu}{\omega}}$. Where, ν is the kinematic viscosity.

Using Equation 2.40b and Equation 2.41b, along with $P_1 = \rho_1 c_0^2$ we get,

$$\langle P_2 \rangle = \frac{1}{2}\kappa_0 \langle P_1^2 \rangle - \frac{1}{2}\rho_0 \langle v_1^2 \rangle \tag{2.42}$$

where the fluid compressibility, κ_0 is given by,

$$\kappa_0 = \frac{1}{\rho_0 c_0^2} \tag{2.43}$$

Now, that we have obtained an expression of the second-order time-averaged pressure in terms of the first-order known terms, we can formulate a numerical solution for the radiation force acting on the particle. The acoustic radiation force is given by the momentum flux equation,

$$\mathbf{F_{rad}} = \int_S \sigma_T \mathbf{n} dS \tag{2.44}$$

where, σ_T is the stress acting on the particle within the pressure field, $\mathbf{n}$ is the normal vector and $\mathbf{F_{rad}}$ is the radiation force acting on the particle as a result of the vibrating pressure field.

The integral is taken over the surface, S of a particle moving in response to the applied force. Thus, the surface is a function of time $S = S(t)$. To accommodate for this fluctuating surface, we add a convective momentum flux term compensating for this fluctuation, thus, compensating for the error. [156] The force, in total, becomes

$$\mathbf{F_{rad}} = \int_{S_0} \sigma_T \mathbf{n} dS - \int_{S_0} \rho \langle (\mathbf{vn}) \cdot \mathbf{v} \rangle dS \tag{2.45}$$

where σ_T is given by the second-order time-averaged pressure as shown in Fig. 2.42,

$$\sigma_T = -\frac{1}{2\rho_0 c_0^2}\langle P_1^2 \rangle + \frac{1}{2}\rho_0 \langle v_1^2 \rangle \tag{2.46}$$

Finally, we arrive at

$$\mathbf{F_{rad}} = \frac{1}{2}\rho_0 \int_{S_0} \left[\langle \mathbf{v_1^2} \rangle - \frac{1}{\rho_0^2 c^2}\langle P_1^2 \rangle \right] \mathbf{n} dS - \rho_0 \int_{S_0} \langle (\mathbf{n} \cdot \mathbf{v_1}) \mathbf{v_1} \rangle dS \tag{2.47}$$

For cases where the compressible particle with radius, r much smaller than that of the acoustic wavelength, λ_{aco} (i.e. $r \ll \lambda_{aco}$) and is present within a standing wave field, an analytical solution can be found. [157,158] This analytical expression is commonly known as Gor'kov's potential [46], and the equation can be used to analytically predict the motion and collection location of the suspended particles. The force, $\mathbf{F_{rad}}$ acting on this small, spherical particle in an unbounded domain can be calculated by,

$$U_{Gor'kov} = 2\pi r^3 \rho_f \left(\frac{1}{3} \frac{\langle P_1^2 \rangle}{\rho_f^2 c_f^2} f_1 - \frac{1}{2} \langle v_1^2 \rangle f_2 \right)$$
$$f_1 = 1 - \frac{\kappa_p}{\kappa_f} \quad , \quad f_2 = \frac{2\left(\rho_p - \rho_f\right)}{2\rho_p + \rho_f} \tag{2.48}$$

where,

$$\mathbf{F_{rad}} = -\nabla U_{Gor'kov} \tag{2.49}$$

where, subscripts f and p denote the fluid and particle respectively.

The direction and the force that dictate the motion of the particle depends on the material properties is given by the acoustic contrast factor, Φ

$$\begin{aligned} \Phi &= \frac{1}{3} f_1 + \frac{1}{2} f_2 \\ &= \frac{1}{3} \left[\frac{5\rho_p - 2\rho_f}{2\rho_p + \rho_f} - \frac{\kappa_p}{\kappa_f} \right] \end{aligned} \tag{2.50}$$

whereby, a positive Φ is dictates the motion of a particle towards the local second-order time-averaged pressure node (i.e. at location where $\langle P_2 \rangle \approx 0$ or local minimum) and the contrary is true for a negative contrast factor, where motion is towards the second-order time-averaged pressure anti-node (i.e. location where $\langle P_2 \rangle$ is a maximum or local maximum).

Acoustic Streaming Induced Drag Forces

Streaming is a phenomenon that corresponds to a net flow within a fluid medium that is generally dominated by an oscillatory flow. [24] There are two main types of streaming arising from sound waves. One is known as 'quartz wind' or Eckart streaming as is a result of a spatial attenuation of a beam of plane travelling wave. The pressure and velocity decay over a distance in the wave propagation direction, resulting in a net force, thus a net flow in that direction, when the time-averaged non-linear effects are considered. This classification of streaming is described in further detail in [19] and will not be discussed in much detail here, as it is not within the scope of this thesis. Secondly, the effect of sound waves interacting with a fluid interface, also give rise to acoustic streaming. This type of streaming is generally observed within the viscous boundary layer, δ_v on the surface. Although the medium in the bulk fluid vibrates irrotationally, it vibrates rotationally (i.e. with vorticity) within this viscous boundary layer as it needs to conform to the no-slip boundary condition of the wall. This classification of streaming known as the 'Schlichting streaming' [19] and drives the bulk flow in the region outside δ_v known as Rayleigh streaming [149] as shown in Fig. 2.6(a). Although, acoustic streaming is often viewed as problematic in many scenarios where streaming generation is inadvertent, when employed correctly, it can serve as a useful tool within microfluidic devices that generally operate in low Reynolds number flows.

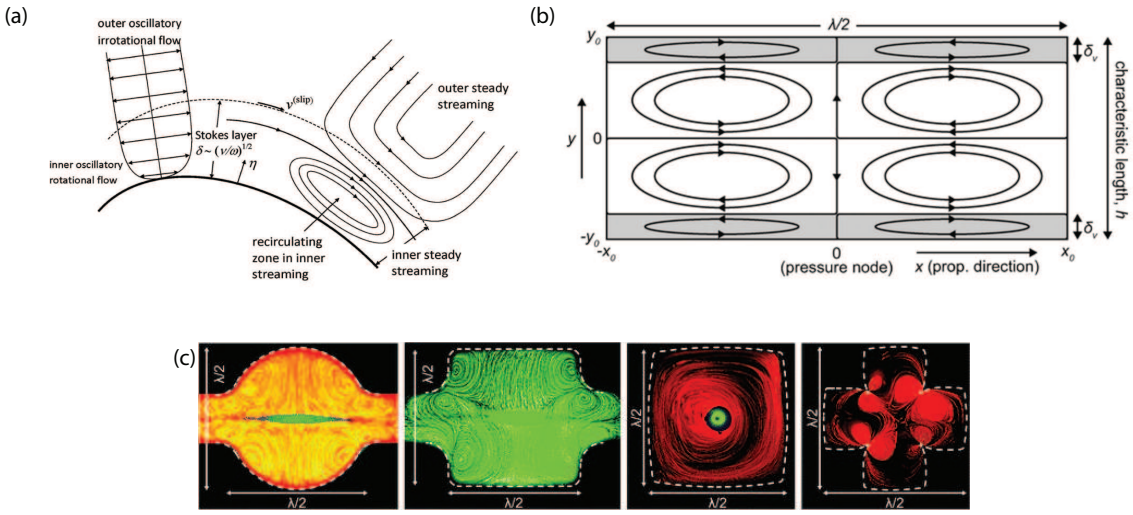

Figure 2.6: (a) Schematic depicting the inner streaming region, 'Schlichting streaming' and the outer steady streaming region, 'Rayleigh streaming'. Reproduced in part from [18] with permission of The Royal Society of Chemistry. (b) A cross-sectional schematic depicting the Rayleigh (outside the δ_v region) and Schlichting (within δ_v region) streaming regions in relation to the pressure node and anti-node locations within a resonant system. (c) An overlay of a series of images visualising various acoustic streaming patterns within different resonant cavity geometries. (b-c) Reproduced in part from [19] with permission of The Royal Society of Chemistry.

If we consider the continuity equation for a compressible fluid and the momentum equation (Navier-Stokes equation), we have

$$\frac{\partial \rho}{\partial t} + \nabla \cdot (\rho \mathbf{v}) = 0 \tag{2.51a}$$

$$\rho \left(\frac{\partial \mathbf{v}}{\partial t} + \mathbf{v} \cdot \nabla \mathbf{v} \right) = -\nabla p + \eta \nabla^2 \mathbf{v} + \left(\beta' + \frac{1}{3} \eta \right) \nabla \left(\nabla \cdot \mathbf{v} \right) \tag{2.51b}$$

it should be noted that, $\beta' + \frac{1}{3}\eta$ was expressed as $\beta\eta$ in Equation 2.39c. If we combine the left-hand side of Equation 2.51b (equated to a body force, $\mathbf{F}$) and Equation 2.51a we arrive at,

$$\mathbf{F} = \frac{\partial \left(\rho \mathbf{v} \right)}{\partial t} + \rho \left(\mathbf{v} \cdot \nabla \right) \mathbf{v} + \mathbf{v} \nabla \cdot \rho \mathbf{v} \tag{2.52}$$

where Equation 2.52, $\mathbf{F}$ can be expressed in two terms, $\mathbf{F_0}$ and $\mathbf{F_{Reynolds}}$, [159]

$$\mathbf{F_0} - \mathbf{F_{Reynolds}} = \frac{\partial \left(\rho \mathbf{v} \right)}{\partial t} + \rho \left(\mathbf{v} \cdot \nabla \right) \mathbf{v} + \mathbf{v} \nabla \cdot \rho \mathbf{v} \tag{2.53a}$$

$$\mathbf{F_0} = \frac{\partial \left(\rho \mathbf{v} \right)}{\partial t} \tag{2.53b}$$

$$-\mathbf{F_{Reynolds}} = \rho \left(\mathbf{v} \cdot \nabla \right) \mathbf{v} + \mathbf{v} \nabla \cdot \rho \mathbf{v} \tag{2.53c}$$

Here, once again we employ the perturbation approach with small disturbances similar to that in Equation 2.36. Here, we also take the time-averages terms to obtain the time

independent effect as previously demonstrated in Equations 2.33 and 2.35. It should be noted that, $\mathbf{F_0}$ time-averages to zero in steady state and therefore, $\mathbf{F} = -\mathbf{F_{Reynolds}}$. Thus, we arrive at the time-averaged time-independent second-order equations,

$$\begin{aligned}\langle \mathbf{F} \rangle &= \langle \rho_0 \left(\mathbf{v_1} \cdot \nabla \right) \mathbf{v_1} + \mathbf{v_1} \nabla \cdot \rho_0 \mathbf{v_1} \rangle \\ &= \rho_0 \langle \left(\mathbf{v_1} \cdot \nabla \right) \mathbf{v_1} + \mathbf{v_1} \nabla \cdot \mathbf{v_1} \rangle\end{aligned} \tag{2.54a}$$

$$\langle \mathbf{F} \rangle = -\nabla \langle P_2 \rangle + \left(\beta' + \frac{1}{3}\eta \right) \langle \nabla \left(\nabla \cdot \mathbf{v_2} \right) \rangle + \eta \langle \nabla^2 \mathbf{v_2} \rangle \tag{2.54b}$$

Equation 2.54a is the Reynolds stress and is the driving force (i.e. body force) and is equivalent to Lighthill's formulation [151]. Based on Equations 2.54, we are able to evaluate the second-order steady state velocity field (i.e. acoustic streaming velocity) based on the first-order velocity and pressure fields.

The motion of the particle that has an initial velocity $\mathbf{u}$, will experience a drag force as a result of this steady-state streaming velocity field is then given by the Stokes drag formula,

$$\mathbf{F_{drag}} = 6\pi\eta r \left(\langle \mathbf{v_2} \rangle - \mathbf{u} \right) \tag{2.55}$$

and as a result the motion of the particle can be predicted.

2.3 Piezoelectric Materials as an Actuator

As mentioned in Section 2.2 piezoelectric materials are a widely used method to excite these systems. The theory of piezoelectricity is well understood and also allows for robust and precise control, therefore, a preferred means of excitation. A piezoelectric material is classified as a crystalline material that exhibits a linear electromechanical interaction between the mechanical and the electrical state without a center of symmetry. [160] The piezoelectric effect is a reversible process, whereby, a crystalline structure is able to convert a mechanical strain into an electrical signal and *vice versa*. Owing to its property, piezoelectric materials are widely used to operate as actuators and sensors in various different applications. Ultrasonic particle manipulation is no exception and has extensively adopted piezoelectric materials to excite acoustofluidic systems with an acoustic field. Materials that possess high piezoelectric constants, such as piezoelectric ceramics are required for efficient and practical operation. In this thesis, two types of piezoelectric ceramics are used, namely Pz26, a modified lead zirconate titanate (PZT) element (manufactured by Ferroperm Piezoceramics), used in the bulk acoustic wave systems (Section 2.4.1, Chapter 3 and 5) and lithium niobate ($LiNbO_3$), used in the surface acoustic wave systems (Section 2.4.2 and Chapter 4). The manufacturing process of these piezoelectric ceramics are not covered in this thesis as it is not in line with the scope of this thesis and were bought from manufacturers, ready to be used.

The use of piezoelectric ceramics in particle manipulation has been extensive in many different bulk acoustic devices used for particle manipulation, [44, 161, 162] cell manipulation, [86,163] levitation in air, [49,164,165] and mixing of fluids [109] to name a few. Surface acoustic wave devices primarily use a rotated $LiNbO_3$ (128° Y-cut X propagating) crystal to excite the system for purposes of particle concentration, [166, 167] to manipulate individual particles, [28] droplet production and manipulation, [66, 100, 168] and many more. Applications of piezoelectric ceramics will be discussed in more detail in the applications subsections as part of the literature review in Section 2.4.

2.3.1 Theory

The onset of an electrical polarization when a material is subjected to mechanical stress is known as "*direct piezoelectric effect*" and when deformation of a material is observed as a result of an applied electrical field it is termed as the "*inverse piezoelectric effect*". [169] As the focus of this thesis is to induce vibration in a fluid chamber, only the second phenomenon will be discussed throughout. If a piezoelectric element is considered, the piezoelectricity arises due to the interaction between the Coulomb forces and the elastic restoring force that is an intrinsic property of the material itself. [170] Therefore, the form of the constitutive relation can be quantified using the resulting strain and electric polarization. [169]

For simplicity, a one-dimensional model is analysed. A piezoelectric element, has an intrinsic polarization density, P_{piezo}. [24] The resulting displacement (i.e. extension/ contraction or shear) is dependent on the orientation (parallel or orthogonal) of the applied electrical field, $\mathbf{E}$. In line with application for particle manipulation, the linear theory of piezoelectric materials utilising the first-order approach is suitable, therefore, described in this thesis. As a result, non-linear strain displacement terms can be neglected.

Constitutive relations is given by relating the electrical quantities ($\mathbf{E}$, $D_{electric}$) with the mechanical quantities (S, T_{piezo}) as follows.

The electric field of a given deformed unit cell at a point r_{cell} away from the middle of a unit cell can be written as, [169]

$$\begin{aligned} \mathbf{E} &= \frac{2q\left(2\delta l_1 - \delta l_2\right)}{2\pi\epsilon_0 r_{cell}^3} \\ &= \frac{2q\delta l}{2\pi\epsilon_0 r_{cell}^3} \end{aligned} \tag{2.56}$$

where the dipole moment, p_{dipole} is given as

$$p_{dipole} = 2q\delta l = 2qlS \tag{2.57}$$

where, $S = \delta l/l$ is the longitudinal strain, q is the charge ($q = 1.6 \times 10^{-19}$ C), ϵ_0 is the permittivity of free space ($\epsilon_0 = 8.85 \times 10^{-12}$ F/m [Farads per metre]), δl and l are the change in length and initial length respectively. Assuming, the element contains N molecules per unit volume, the electric polarization density, which is the dipole moment per unit volume is written as,

$$P_{piezo} = Nq = 2qlNS = eS \tag{2.58}$$

where, e is by definition the piezoelectric stress constant ($e = 2qlN$). Therefore, accommodating for the polarization the electric displacement $D_{electric}$ is given by,

$$D_{electric} = \epsilon\mathbf{E} + eS \tag{2.59}$$

Similarly, when an external electric field is applied, the Hooke's law has an additional stress term, $-e\mathbf{E}$ and is now written as,

$$T_{piezo} = cS - e\mathbf{E} \tag{2.60}$$

In order to develop a constitutive relationship between the four variables ($\mathbf{E}$, $D_{electrical}$, S, T_{piezo}), we begin by assuming,

$$T_{piezo} = T_{piezo}(S, \mathbf{E}) \quad \text{and} \quad D_{electric} = (S, \mathbf{E}) \tag{2.61}$$

then using Taylor's expansion for small fields, we have

$$T_{piezo} = \left(\frac{\partial T_{piezo}}{\partial S}\right)_{\mathbf{E}} S + \left(\frac{\partial T_{piezo}}{\partial \mathbf{E}}\right)_{S} \mathbf{E} \tag{2.62a}$$

$$D_{electric} = \left(\frac{\partial D_{electric}}{\partial S}\right)_{\mathbf{E}} S + \left(\frac{\partial D_{electric}}{\partial \mathbf{E}}\right)_{S} \mathbf{E} \tag{2.62b}$$

Therefore, constants that are evaluated at precise experimental conditions are required, such as at constant (zero) electrical field

$$c^{\mathbf{E}} = \left(\frac{\partial T_{piezo}}{\partial S}\right)_{\mathbf{E}} \quad \text{and} \quad e^{\mathbf{E}} = \left(\frac{\partial D_{electric}}{\partial S}\right)_{\mathbf{E}} \tag{2.63}$$

or at constant (zero) strain as,

$$e^{S} = \left(\frac{\partial T_{piezo}}{\partial \mathbf{E}}\right)_{S} \quad \text{and} \quad \epsilon^{\mathbf{E}} = \left(\frac{\partial D_{electric}}{\partial \mathbf{E}}\right)_{S} \tag{2.64}$$

where, e^{S} and $e^{\mathbf{E}}$ are the inverse piezoelectric constant and the direct piezoelectric constant respectively. Where,

$$-e^{S} = e^{\mathbf{E}} = e \tag{2.65}$$

Therefore, Equations 2.59 and 2.60 can be rewritten as,

$$T_{piezo} = c^{\mathbf{E}} S + e\mathbf{E} \tag{2.66a}$$

$$D_{electric} = eS + \epsilon^{S}\mathbf{E} \tag{2.66b}$$

Using similar arguments, we can also deduce,

$$S = s^{\mathbf{E}} T_{piezo} + d\mathbf{E} \quad \text{and} \quad D_{electric} = dT_{piezo} + \epsilon^{T_{piezo}}\mathbf{E} \tag{2.67a}$$

$$S = S^{D_{electric}} T_{piezo} + gD_{electric} \quad \text{and} \quad \mathbf{E} = -gT_{piezo} + \beta^{T_{piezo}} D_{electric} \tag{2.67b}$$

and,

$$T_{piezo} = c^{D_{electric}} S - hD_{electric} \tag{2.68a}$$

$$\mathbf{E} = -hS + \beta^{S} D_{electric} \tag{2.68b}$$

where, d is the piezoelectric charge constant in [C/N], g is the piezoelectric voltage constant in [V. m/N] and β at constant T_{piezo} or S is the propagation constant at constant stress or stress respectively. h is given as $h = e/\epsilon^{S}$.

If a one-dimensional analysis of a two-terminal piezoelectric substrate excited by a voltage, $V_{excitation}$ sandwiched between two mediums (i.e. backing material and matching layer for instance), a transfer matrix that describes the forces, $F_{\#}$ exerted on either side of the substrate can be written as,

$$\begin{bmatrix} F_{side,1} \\ F_{side,2} \\ V_{excitation} \end{bmatrix} = -i \begin{bmatrix} Z_{pz}cot\left(\beta_{pz}l\right) & Z_{pz}csc\left(\beta_{pz}l\right) & \frac{h}{\omega} \\ Z_{pz}csc\left(\beta_{pz}l\right) & Z_{pz}cot\left(\beta_{pz}l\right) & \frac{h}{\omega} \\ \frac{h}{\omega} & \frac{h}{\omega} & \frac{h}{\omega}C_0 \end{bmatrix} \begin{bmatrix} v_{side,1} \\ v_{side,2} \\ I \end{bmatrix}$$

where, subscripts $side, 1$ and $side, 2$ refer to the medium on the left and right of the substrate respectively. Z_{pz} is the acoustic impedance of the piezoelectric element given by, $Z_{pz} = A_{area}\sqrt{\rho_{pz}c^D}$, where ρ_{pz} is the density of the piezoelectric element and c^D is the piezoelectric stiffened elastic constant and is given by,

$$c^D = c^E\left(1 + \frac{e^2}{c^E\epsilon^S}\right) = c^E\left(1 + K^2\right) \tag{2.69}$$

where, c^E is the elastic constant and K^2 is the piezoelectric coupling factor. β_{pz} is the wavenumber in the piezoelectric element and is given by, $\beta_{pz} = \omega/c_L^D$, where, the stiffened longitudinal velocity, $c_L^D = \sqrt{E^D/\rho_{pz}}$. C_0 is the clamped zero capacitance given by,

$$C_0 = \frac{\epsilon^S A}{l} \tag{2.70}$$

This matrix can be adopted when designing a layered resonator for use in microfluidic systems by defining the velocities, $v_{\#}$ and forces, $F_{\#}$ in terms of the medium properties (i.e. density and speed of sound). It should be noted that a more general formulation, where a one-dimensional propagation through a two-electrode arbitrarily oriented layered piezoelectric substrate was developed by Nowotny and Benes. [171] However, in this thesis a simplified transfer matrix can be used and therefore the formulation in Equation 2.3.1 adopted from [169] was utilised to optimise a layered resonator for operation in air as discussed in Chapter 5.

2.4 Excitation Methods

Within acoustofluidic systems, two major types of excitation methods are utilised to establish the desired acoustic fields within the fluid medium. These methods are known as bulk acoustic waves (BAW) (Section 2.4.1) and surface acoustic waves (SAW) (Section 2.4.2). Utilisation of a particular methods is warranted by the application or task at hand as each method has their advantages and disadvantages. The major difference between the two methods, is that for BAW systems, the entire fluid volume (i.e. channel or chamber) is vibrated or resonated, whilst, SAW based devices have a localised acoustic field that is dictated solely by the resonance of patterned inter-digital transducers (based on the intended frequency of operation) and not the channel or chamber geometry. In this section, the theory associated with these actuation methods, fabrication and applications within developed microfluidic systems will be discussed.

2.4.1 Bulk Acoustic Waves

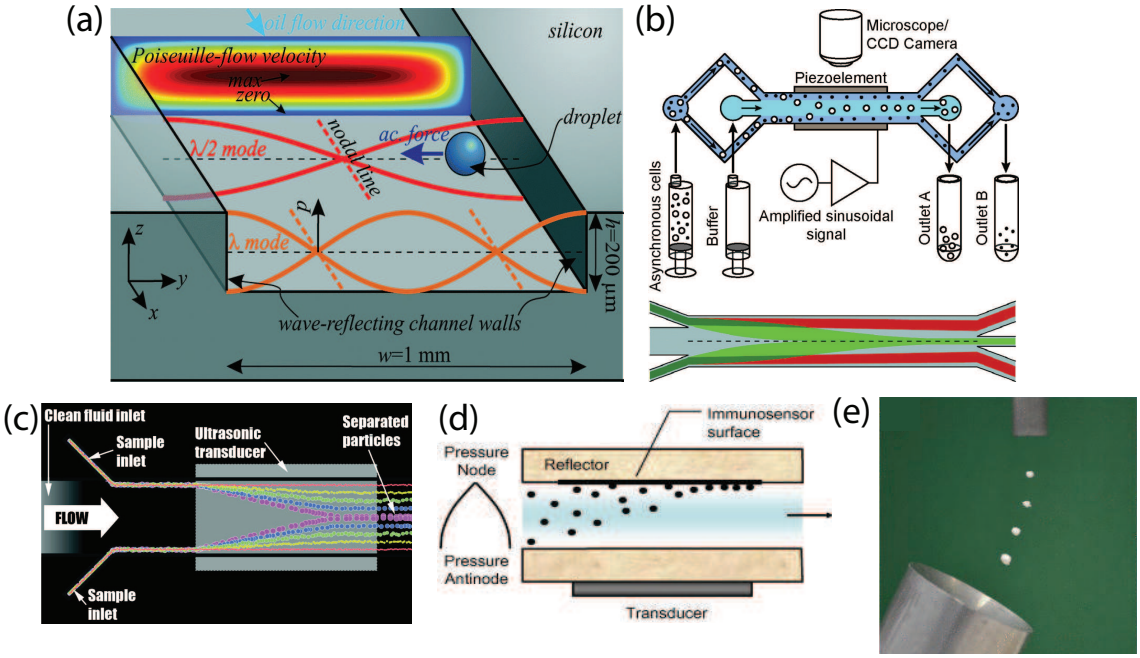

Figure 2.7: Examples of bulk acoustic wave based systems for particle manipulation. (a) Schematic of a BAW systems used to manipulate droplets suspended within a fluid medium and representation of half and full acoustic wavelength modes. Reproduced under a Creative Commons Attribution 3.0 Unported Licence from [20]. (b) Schematic of a complete acoustophoretic cell synchronisation system utilising BAW to sort large cells from small cells (minimal effect by the acoustic field). Reprinted with permission from [21]. Copyright 2007 American Chemical Society. (c) Continuous free flow BAW based size deterministic particle separation based on the balance between exposure time and forces exerted on particles of various size. Reprinted with permission from [14]. Copyright 2007 American Chemical Society. (d) Schematic of a quarter wave resonator used for particle filtration. Reprinted from [22], Copyright 2008, with permission from Elsevier. (e) A non-resonant acoustic levitator for particle manipulation in air. Reprinted with permission from [23]. Copyright 2015, AIP Publishing LLC.

As the name indicates, bulk acoustic wave based devices are systems whereby, the bulk of the fluid medium is resonated by a vibration. Thus, the mode of vibration is strongly dictated by the geometry of the device itself. Due to its geometry dependent nature, early on, BAW devices generally operated in multi node resonance modes and were in centimetre dimensions or larger. [172,173] Over time, with advancements in micro-fabrication techniques, these dimensions were reduced to millimetre sizes and smaller, therefore, increasing the frequency of operation.

Theory

When designing a system that utilises BAW, we consider the geometry of the system. Commonly, the width of a channel is considered for a continuous free flow system as such shown in Fig. 2.7 (a) to (c). In contrary, within batch process systems, where a two-dimensional field is required, both the channel width and length needs to be considered or the height is to be considered if a vertical wave is established as shown in Fig. 2.7 (d). Essentially, the dimension that is parallel to the wave propagation direction is important in the design process. In order to establish a resonant mode or resonance, the characteristic channel or chamber dimensions should be a multiple of half-wavelength. It should be noted, this is only the case if the channel or chamber alone dictates the field. However, if a resonant reflector that imposes a pressure release boundary condition as discussed by Hill *et al* is used, the chamber can be designed to establish a quarter wavelength acoustic field that pushes suspended particles towards the reflector surface. [22, 162, 174] A great benefit of decreasing the size of the system is the increase in the frequency of operation. By increasing the frequency, the radiation forces associated increases as well, therefore, efficient particle manipulation can be achieved. [148] The primary axial force, F_{ax} acting upon a particle in suspension is given by,

$$F_{ax} = 4\pi r^3 E_{ac} k_{wave} \sin(2k_{wave}x)\Phi \tag{2.71}$$

where, r is the particle radius, E_{ac} is the acoustic energy density, x is the particle position in the wave propagation direction,Φ is the acoustic contrast factor as given in Equation 2.50 and k_{wave} is the wave number given by,

$$k_{wave} = \frac{\omega}{c_f} = \frac{2\pi f}{c_f} \tag{2.72}$$

where, f is the frequency and c_f is the speed of sound of the fluid medium.

The acoustic energy density, E_{ac} is given by,

$$E_{ac} = \frac{P_a^2}{4\rho_f c_f^2} = \frac{1}{4}\rho_f v_a^2 \tag{2.73}$$

where, P_a and v_a are the absolute pressure and velocity fields.

Equation 2.71 can be written in terms of a velocity potential amplitude, Ψ_a instead of the acoustic energy density as below, [148]

$$F_{ax} = \Psi_a^2 \rho_f \pi \left(k_{wave} r\right)^3 \Phi \sin\left(2k_{wave} x\right) \tag{2.74}$$

where, the velocity potential, ψ is defined as,

$$\psi = \Psi_a e^{i(\omega t \mp k_{wave} x + \theta)} \tag{2.75}$$

where, t is time, the $\mp$ dictates the propagation direction either in the positive x or negative x direction respectively and θ is the phase of the wave at its initial condition.

The wavelength of a system is given by rearranging the velocity of an oscillating wave equation to arrive at,

$$\lambda_f = \frac{c_f}{f} \tag{2.76}$$

Therefore, the channel dimensions are fabricated based the wavelength, λ_f or multiples thereof depending on requirements of the system.

Design and Fabrication

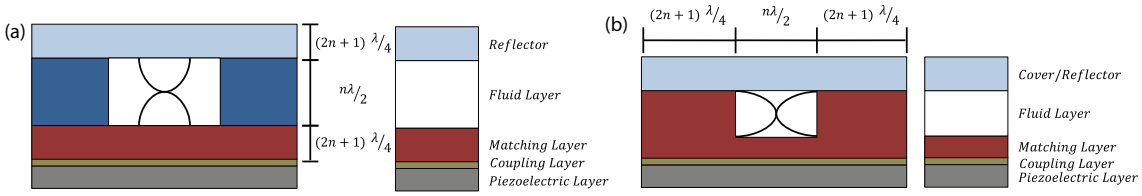

Figure 2.8: Schematic diagram of different resonator configurations along with the ideal dimensions (n is an integer multiple) and the orientation of the standing wave depicted for a (a) layered resonator and a (b) transversal resonator. Dimensions adopted from [24].

There are two major types of transducer designs or configurations that are generally associated with bulk acoustic waves, namely, layered resonator as used in Chapter 5 and a transversal resonator as used in Chapter 3.

A layered resonator typically consists of a piezoelectric element (i.e. transducer), a coupling layer, a matching layer, the fluid layer and a reflector. Each of these layers play a major role in building an efficient resonator. Firstly, as discussed in Section 2.3, the piezoelectric layer excites (i.e. generates the sound wave) the resonator based on an input A/C signal. The coupling layer serves as an adhesive layer and also transmits the generated sound wave from the transducer to the next layer. Next follows the matching layer (also known as the carrier layer or transmission layer), which acts as a good acoustic transmission layer and also forms the bottom of the resonating chamber. The fluid layer where the suspended particle or cells are manipulated is then sandwiched between the matching layer and the reflector as shown in Fig. 2.8 (a). Typical dimensions (i.e. thickness of individual

layers) that are used for optimum energy transmission into the fluid medium are included. As shown in Fig. 2.8 (a), the fluid layer here is given as multiples of half-wavelength (i.e. $\frac{n\lambda}{2}$). However, quarter-wavelength fluid layers can be designed albeit less efficient, by altering the design criteria of the reflector layer to ensure it acts as a pressure release boundary. [22, 162, 174]

Consideration of the material selection for each individual layer, especially the matching layer should be taken into account as well, to ensure maximum energy transfer. At an interface, part of the energy is transmitted and another part is reflected depending on the material properties and incident angle, thus, strongly influencing the amount of damping and efficiency of the device at a particular resonance mode. If we consider a normal incidence, the reflected energy, R_{energy} and transmitted energy, T_{energy} are given by, [24]

$$R_{energy} = \frac{(Z_2 - Z_1)^2}{(Z_2 + Z_1)^2} \tag{2.77a}$$

$$\begin{aligned} T_{energy} &= 1 - R_{energy} \\ &= \frac{4Z_1Z_2}{(Z_2 + Z_1)^2} \end{aligned} \tag{2.77b}$$

where, $Z_i = \rho_i c_i$ are the characteristic impedances of the two materials respectively and dictate the energy transfer characteristics of the system. Therefore, materials that are impedance matched with each other allow for efficient device operation and should be used if possible.

In contrast to layered resonators, a transversal resonator operates such that the standing wave orientation is perpendicular to that of the incident actuation as shown in Fig. 2.8 (b). The fluid layer or channel width would correspond to that of a half wavelength. A major benefit of using transversal resonators as opposed to layered resonators is that focusing of particles occur in plane with the resonator chip. Focusing the particles in this plane allows for ease of visual observation and also allows for easy integration with other microfluidic components.

Applications

Bulk acoustic waves have been extensively used in the development of various microfluidic applications since its inception in acoustofluidics. Its applications range from filtration to medium exchange for cells or biologicals. Despite its wide range of applications, this section will discuss the utilisation of BAW for particle manipulation with the purpose of concentration and separation or sorting exclusively in line with the scope of this thesis.

Ultrasonic particle filtration systems has been of major interests as a component for bioreactor systems and therapeutic protein production. [24] Early on, these devices were relatively large (i.e. on the order of multiple wavelengths) [175] and progressively were

reduced in size to half -wavelength resonators. [176] This was later simplified to a quarter-wave resonators by Townsend *et al* [177] and Hill *et al.* [22] Although quarter-wavelength resonators are less energy efficient than their half-wavelength counterpart, the use of these systems simplify the detection and sensing process as particles move towards the surface, thus, the need of a stream to be split into two (i.e. one stream containing the concentrate and another the clarified stream) as opposed to half-wavelength resonators where the clarified stream is on either side of the concentrate stream.

Concentration of particles of a particular species is also of large interest for sensing and detection applications. The enrichment and concentration of a stream containing a single species of particles have been developed using continuous flow acoustophoresis. [178–180] Simultaneous sorting and concentration of particles have also been studied for similar applications when two or more species of particles or cells are present within the sample. Systems such as split-flow thin (SPLITT) fractionation were developed to separate two species of particles when exposed to an external force field. [181] This system is based on the principle that larger particles will be more affected by the external force field and will migrate more in comparison to the smaller particles, therefore, moving the larger particles beyond the flow splitter. Johnson and Feke [182] built the first acoustic based SPLITT fractionator. Lenshof *et al* [183] applied a similar concept to separate larger leukocyte cells from the smaller platelets. The concept of utilising the force contrast between two particles of different sizes has since been applied to other acoustophoretic based devices to sort more than two species of particles as shown in Fig. 2.7 (c). [14, 184] Furthermore, the exploitation of negative contrast factor particles such as lipid has been used within acoustic based sorting devices. [163] Utilisation of bulk acoustic waves techniques to perform cell washing and mixing [185] of yeast cells within a SPLITT separator. This was followed by Petersson *et al* [186] developed a device to perform carrier medium exchange of blood cells using acoustophoretic forces.

Concentration of particles within chambers and channels for purposes of inspection has also been demonstrated within static fluid medium for batch processing. Particle positioning within lines in a chamber [187] and in channels to be used with a microgripper. [161,188] Patterning of particles and cells in clusters within a 2-dimensional field, [189] positioning of particles within an octagonal sonotweezer, [190] and in a full 3-dimensional sound field. [191] The use of acoustic streaming induced drag forces to enhance particle separation while concentrating particles with the use of acoustic radiation forces within a static fluid medium is explored in Chapter 3.

The use of BAW can be extended to air based systems and is not limited to liquid systems. A need for a non-contact approach in handling sensitive particles (i.e. cells and reactive elements) is evident as conventional methods involving frictional gripping may lead to sample damage. Furthermore, problems arising due to stiction as a result of high surface area to size ratio associated with microparticles. The employment of a non-contact

approach eradicates issues associated with conventional manipulation techniques. While acoustic manipulation in liquid systems have been extensively investigated, there are only a handful of reported studies on the use of acoustics within air based systems for particle trapping and transport. An extensive literature review is carried out in Chapter 5 looking into particle manipulation in air using acoustics. As reported, it has been a challenge to levitate and trap individual particles that are very small and denser than water in air. The smallest reported individual particle manipulated in previous studies are down to the size of 500 μm. [49] In Chapter 5, it is proposed that the use of high frequencies (in the range of MHz) are to be used so that very small particles (as small as 14.8 μm) can be individually manipulated. [32]

2.4.2 Surface Acoustic Waves

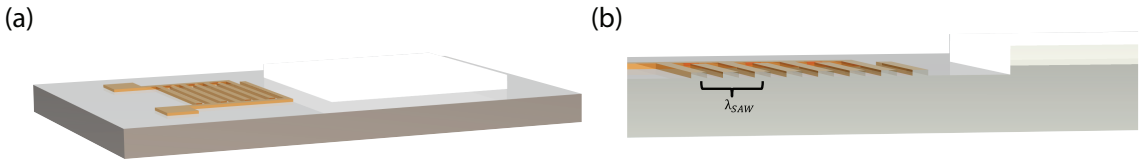

Figure 2.9: ((a) A typical SAW based system along with the transducer (IDTs; in gold) setup and fluid chamber (in white). (b) A cross-section image depicting the spacing of the IDT fingers

In 1885, Lord Rayleigh first introduced the theory of surface waves. [192] Here, he proposed to investigate the characteristics of a wave on a free surface of a infinite homogeneous isotropic elastic solid, such that the disturbances are confined to a small region comparable to that of the wavelength. He went on to draw comparisons with deep-water waves, with the exception that the restoring forces are dependent on the "elastic resilience" (i.e. elastic forces of the solid) instead of gravity and surface tension as in liquids. Due to the nature of surface wave propagation which predominantly spreads in two dimensions only, amplitude decays occurs at a slower rate with distance as compared to bulk elastic waves. [24] At its inception, surface waves was seen as significant in understanding seismology. However, with the application of microfabrication techniques and piezoelectrics, the scales of these systems have decreased and thus been applied to various different fields such as surface testing, electronic filters and sensors [193] as well as microfluidics.

A major difference between SAW and BAW is that the acoustic wave generation within the fluid medium is exclusively within the vicinity of the wave generation rather than the entire fluid volume being resonated. SAW based acoustic devices also offer a major advantage of operating at much higher frequencies as compared to BAW devices, which allows for much better control of particle manipulation. Generation of SAW, utilising two opposing interdigital transducers (IDTs) allows for the formation of standing surface acoustic waves (SSAW) independent of channel geometry. The inherent nature of SAW means the wave propagation is restricted to the surface, hence, energy dissipation is

low, making it more efficient than that of BAW devices.

Theory

To generate a SAW, a series of IDTs are patterned on a piezoelectric substrate as shown in Fig. 2.9. When an A/C signal is applied across the patterned array of IDTs, a surface displacement is observed due to the piezoelectric nature of the substrate as discussed in Section 2.3 (a). These IDTs are patterned with a certain design to ensure efficient generation of a SAW propagating along the surface and transmitting into the intended fluid volume. The IDTs are designed to ensure the emanating SAW is reinforced by each finger pair. Therefore, the width of each finger and the spacing of between them are designed in accordance to the intended operational frequency. The frequency, f_{SAW} is given by,

$$f_{SAW} = \frac{c_{SAW}}{\lambda_{SAW}} \tag{2.78}$$

where, c_{SAW} is the phase velocity of the piezoelectric substrate which differs based on the direction of propagation [194] and λ_{SAW} is the resonant SAW wavelength produced.

The most basic design of IDTs for use in acoustofluidics constitute of $\frac{1}{4}\lambda_{SAW}$ wide fingers and patterned with a gap between finger pairs of the same dimensions. Pre-dominantly, lithium niobate ($LiNbO_3$) is used as the piezoelectric element as it has favourable characteristics such as its high spontaneous polarization and electromechanical coupling coefficients [195, 196] and low acoustic attenuation [197]. A propagating SAW along a surface will radiate energy at an angle when it encounters a fluid-solid interface. This angle is known as the Rayleigh angle, θ_R and is defined as the angle of propagation into the fluid from the normal to the substrate, given by the Snell's law, [24]

$$\theta_R = \sin^{-1}\left(\frac{c_f}{c_{SAW}}\right) \tag{2.79}$$

This transmitted wave is known as the leaky Rayleigh wave as the Rayleigh wave leaks energy into the fluid medium as it travels along the fluid-solid interface. It should be noted that attenuation along a solid-gas interface occurs but is relatively small and therefore can be neglected. The attenuation coefficient,α_{LR} of the leaky Rayleigh wave due to radiation of a compression wave along a fluid-solid interface is given by, [198]

$$\alpha_{LR} = \frac{\rho_f c_f}{\rho_{substrate} c_{SAW} \lambda_{SAW}} \quad \text{in} \quad \mathrm{m}^{-1} \tag{2.80}$$

where, $\rho_{substrate}$ is the density of the piezoelectric substrate. It should be noted that there is an additional energy loss due to frictional losses [198] but is typically small and therefore, often neglected.

In addition to consideration of attenuation within the liquid and IDT finger spacings, the number of finger pairs also play an integral role in ensuring efficient operation. Besides the reinforcing the propagating wave, the additional IDT pairs alter the electrical impedance of the system. In a similar way, whereby, acoustically impedance matched systems operate optimally, an electrically impedance matched circuit ensures maximum energy transfer from the external power source (i.e. signal generator and power amplifier) to the IDTs and therefore, maximum power transmission to the piezoelectric substrate and thus, the fluid medium. It should be noted, the number of finger pairs is not critical for operation as systems would still function, albeit not optimally.

It is also worth noting that there are other designs of IDTs which are used for various different applications in acoustofluidics as shown in Fig. 2.10. Each of these IDT configurations result in a different displacement field and thus a different pressure field within the fluid medium. The normal or straight IDTs are most commonly used in microfluidic devices as it is the most efficient design in terms of operation. This configuration operates at a single frequency as dictated by the uniform finger width and spacings as shown in Fig. 2.10 (a), thus making it easy to define the displacement and resultant pressure field. Focused or curved IDTs [199] consists of pairs of annular electrodes and can operate at a single frequency or multiple frequencies as well but directs the propagating wave and energy to a small focal point. This high acoustic intensity region that is desirable in certain applications such as micro-droplet production. [66] The slanted IDTs on the other hand, consists of a varying finger width along its length, allowing for the generation of narrow SAW beams of varying frequencies. [200] Chirped IDTs [28] similarly allow for variation but in terms of frequency of operation, where a range of frequencies can be excited as opposed to a single frequency. This is as a direct result of the variation in finger widths throughout the IDT set as shown in Fig. 2.10 (d). Due to the benefit of operating over a range of frequencies, chirped IDTs allow for a sweep of frequencies to be used which is highly beneficial for migrating particles beyond a wavelength as discussed in Chapter 4. It is worth noting, the configuration of chirped IDTs can be integrated with that of curved IDT designs to emanate a propagating wave with a high spatial amplitude gradient (i.e. focal point) over a range of frequencies.

A typical SAW based acoustofluidic device uses at least one set of IDTs to produce an acoustic field within the intended fluid medium. In such a scenario, a travelling surface acoustic wave (TSAW) is observed where the fluid volume comes in contact with the wave's propagation path. The forces, experienced by a particle within an acoustic field is given by the general formulation as in Equation 2.47. For a more specific formulation, Yosioka and Kawasima formulated the acoustic radiation force acting on a small compressible particle ($r \ll \lambda_{aco}$) within a plane progressive wave (i.e. travelling acoustic wave) and is given as,

$$F_{TSAW} = 4\pi r^2 \left(k_f r\right)^4 \left(\frac{I_{aco}}{c_f}\right) \Phi \tag{2.81a}$$

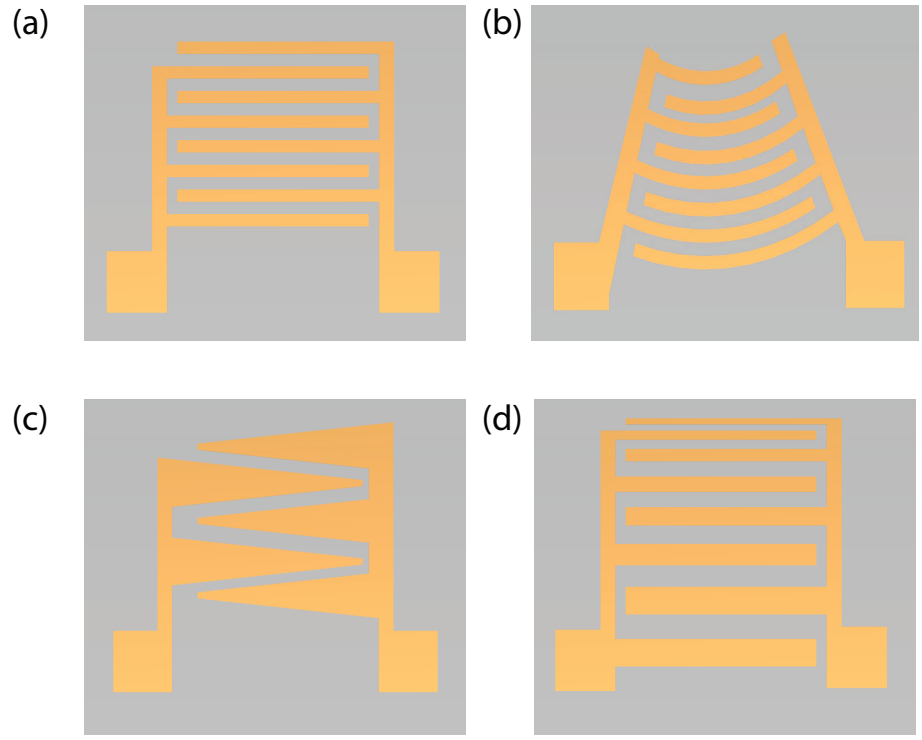

Figure 2.10: Schematic of different IDT configurations(a) Normal or straight (b) Focused or curved (c) Slanted (d) Chirped

where,

$$I_{aco} = \frac{\rho_f c_f k_f^2}{2} \tag{2.81b}$$

where, I_{aco} is the intensity of the incident acoustic wave and $k_f = \frac{2\pi}{\lambda_{aco}}$ is the wavenumber in the fluid medium.

In the case where two opposing IDT sets are used and operated at the same frequency, a standing surface acoustic wave (SSAW) can be established. In this case, the forces exerted upon a small ($r \ll \lambda_{aco}$) compressible spherical particle is given by Gor'kov's equation (see Equation 2.48) or Yosioka's formulation (see Equation 2.71) as they behave in the same manner as a particle within an acoustic field and is independent of the excitation method.

Fabrication

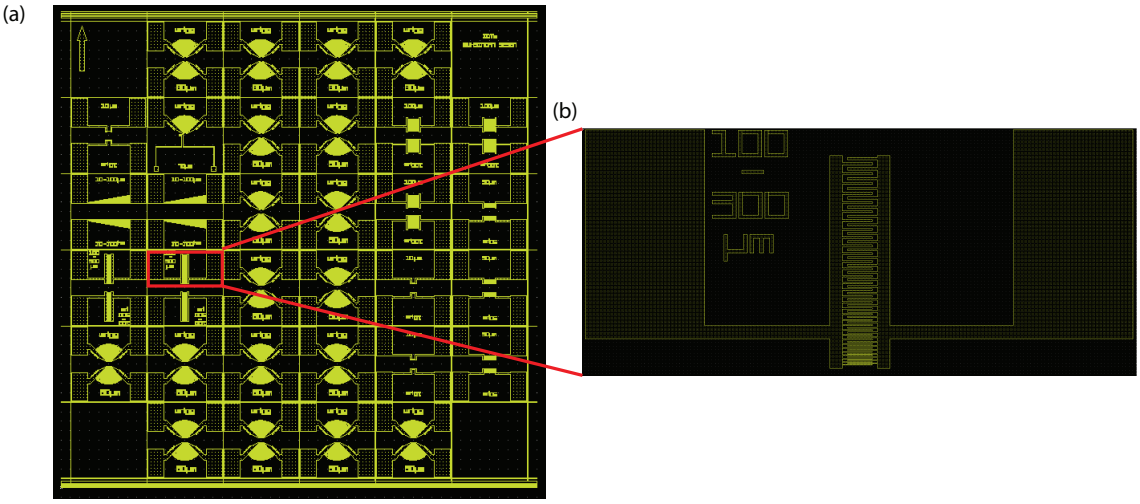

Figure 2.11: (a) An example mask design created using the LayoutEditor^{TM} software and (b) a zoomed in section of a 100 to 300 μm chirped IDT design.

SAW based acoustofluidic devices are a direct result of microfabrication techniques that allow the fabrication of micron-sized to sub-micron features which are essential to the functionality of these devices. A typical SAW based acoustofluidic device consists of a piezoelectric substrate, patterned with IDTs bonded to a microfluidic channel or chamber that would contain the fluid medium. This section will describe the specific procedures carried out to reliably fabricate and construct these devices. For the work carried out in Chapter 4 where SAW was the excitation method used, a 0.5 mm thick, 128° Y-cut X-propagating $LiNbO_3$ wafer was utilised. This particular crystal cut offers a large electromechanical coupling coefficient [201] and is commonly used in most SAW based acoustofluidic devices.

An operational SAW device is comprised of the IDTs and contact pads for electrical connection (as shown in Fig. 2.11) deposited on a piezoelectric substrate. A good electrical conductor is chosen for patterning the required IDT designs; gold (Au) and aluminium (Al) are suitable metals for this application. In addition, a thin (5-10 nm) metal adhesion layer (chromium, Cr and titanium, Ti generally used) is deposited between the conductor and the piezoelectric substrate. The thickness of the conducting metal varies depending on design considerations and can be up to 1 μm thick. The process of patterning the $LiNbO_3$ begins with spin coating the piezoelectric wafer with a layer of photoresist, followed by heat treating (i.e. pre-bake) it to remove any remaining solvents within the photoresist. A photomask containing the required designs is then used to selectively block regions of the spin coated wafer from exposure of the ultraviolet (UV) light. This process is known as photolithography. After exposure, the wafer is developed with an appropriate developer bath to dissolve the regions exposed to the light in the case of a positive photoresist and the inverse is true for a negative photoresist (as used in Fig. 2.12 (b)).

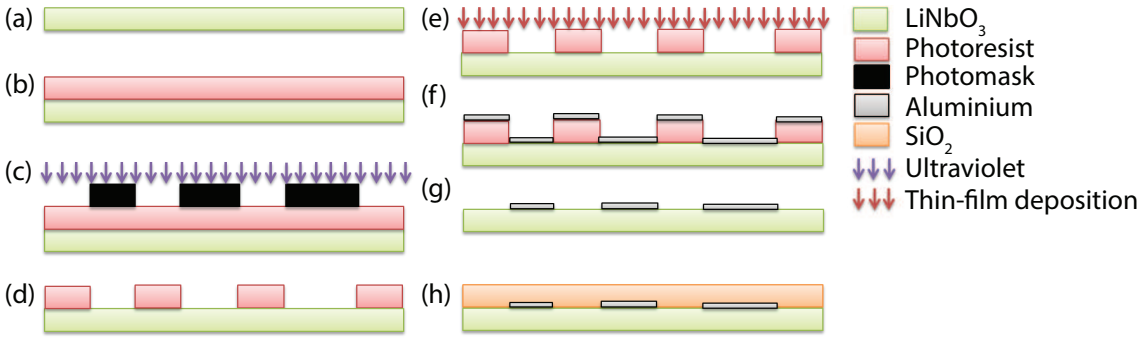

Figure 2.12: Process diagram of SAW device fabrication. (a) Start with a $LiNbO_3$ wafer (b) $LiNbO_3$ spin coated with a negative photoresist before (c) a photomask is aligned and the wafer is exposed to ultraviolet (UV) light. (d) The masked regions are then dissolved followed by (e) metal deposition using e-beam thin-film deposition, resulting in (f) a uniform layer of metal deposited. (g) Lift-off is performed to remove the unwanted metal regions and the remaining photoresist. (h) Finally, a thin layer of SiO_2 is deposited.

Once the desired regions of photoresist has been removed, the required metals are deposited in a process called evaporation or thin-film deposition as shown in Fig. 2.12 (e). Here a layer of constant thickness (as required) is deposited on the developed wafer. The method of evaporation used within this thesis is a high-vacuum e-beam evaporation, whereby, an electron beam is used to heat the metal to a point where "evaporation" occurs. The thickness of the deposited metal depends and can be controlled on both, the metal temperature and the exposure time. Once, the metal deposition is done, the application of a solvent is used to dissolve the remaining photoresist and any metals that were not deposited straight onto the substrate itself (i.e. the regions of the remaining photoresist after the developer bath). This process is called "lift-off", as it lifts off any metals not deposited on the substrate as shown in Fig. 2.12 (g). When and if it is possible, a thin layer of silicon dioxide, SiO_2 is deposited on top of the deposited metals and substrate. This serves two purposes, to protect the metal electrodes from corrosion and to enhance the bonding strength between the PDMS channels and the piezoelectric substrate. However, it should be noted that this step is not always possible as it reduces the functionality of the IDTs for certain applications such as DEP. Finally, as multiple designs and devices are patterned on a single $LiNbO_3$ wafer (see Fig. 2.11 (a)), each device is cut or diced along a pre-defined line using a high-speed ($\approx$ 30,000 rpm), small width (30 μm) cutting tool.

The second component to a SAW based acoustofluidic device is the chamber or channel that contains the fluid medium. Here once again, we use photolithography (see Fig. 2.13 (b))to create the micron-sized features on a silicon wafer. It should be noted that the features created are the inverse of the channel or chamber design in a manner that is analogous to a film negative. This is because the features created on the silicon wafer serve as a mould for the final channels or chambers. After photolithography, the silicon wafer is developed in a developer bath to dissolve the non-crosslinked photoresist regions, similar to that done in the SAW device fabrication process. This is followed by etching into the silicon itself using deep-reactive ion etching (DRIE), whereby a repeated process of etchant

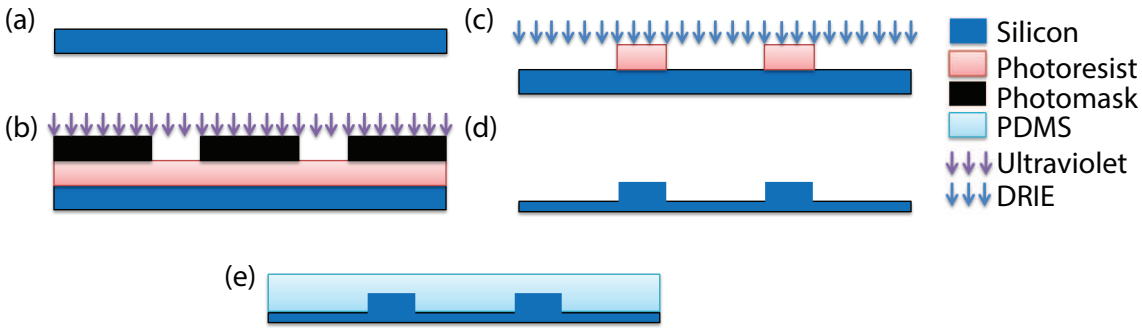

Figure 2.13: Process diagram of the PDMS mould fabrication. (a) Start with a silicon wafer that is (b) spin coated with photoresist and aligned with a photomask and exposed to ultraviolet light. (c) After dissolving the unwanted photoresist, the silicon wafer is etched using DRIE. (e) Finally, the mould is filled with PDMS to transfer the channel or chamber patterns.

(sulfur hexafluoride, SF_6) and a passivation layer (perfluorocyclobutane, C_4F_8) plasma over multiple cycles to achieve the required etch depth, with an isotropic, near vertical wall as shown in Fig. 2.13 (d). As the photoresist is not resistant to the etching process but etches away at a much slower rate than that of the silicon, the minimum thickness of the photoresist layer is integral to ensure that it is able to withstand the entire etching process. If a relatively deep etch is required, it may be more practical to use a Cr mask, which can be patterned on using the same method as carried out for the lift-off process. The etched silicon mould is then casted with a thermoset polymer known as polydimethylsiloxane (PDMS). PDMS is common amongst microfluidic devices as it boasts a variety of favourable characteristics such as ease of transferring patterns with nm size resolutions, gas permeability (increases its biocompatibility) and its inherent optically transparent nature that eases visualisation. The poured PDMS is then degassed (to remove the air bubbles introduced during the mixing of the PDMS base and curing agent) and allowed to set. The time duration of setting can be reduced by application of heat.

Finally, once these two components are fabricated, the SAW device and the chamber is joined together through a bonding process. The inlets and outlets of the chambers and channels are ported as it eases the removal of PDMS from these regions as opposed to after bonding. Oxygen plasma treatment of the substrate surface (i.e. $LiNbO_3$) and the surface of the PDMS is important to achieve a strong, waterproof bond between the $LiNbO_3$ and the PDMS block with the channel imprint. Exposure to the oxygen plasma activates the PDMS surface on the imprint side resulting in a hydroxyl, -OH surface which forms a strong hydrogen bond with the SiO_2 coated $LiNbO_3$ surface, thus, forming a permanent waterproof seal when the two components are brought into contact. The moulded PDMS is carefully aligned with the piezoelectric substrate to operate in the intended manner (i.e. location of IDT in relation to the chambers or channels).

Applications

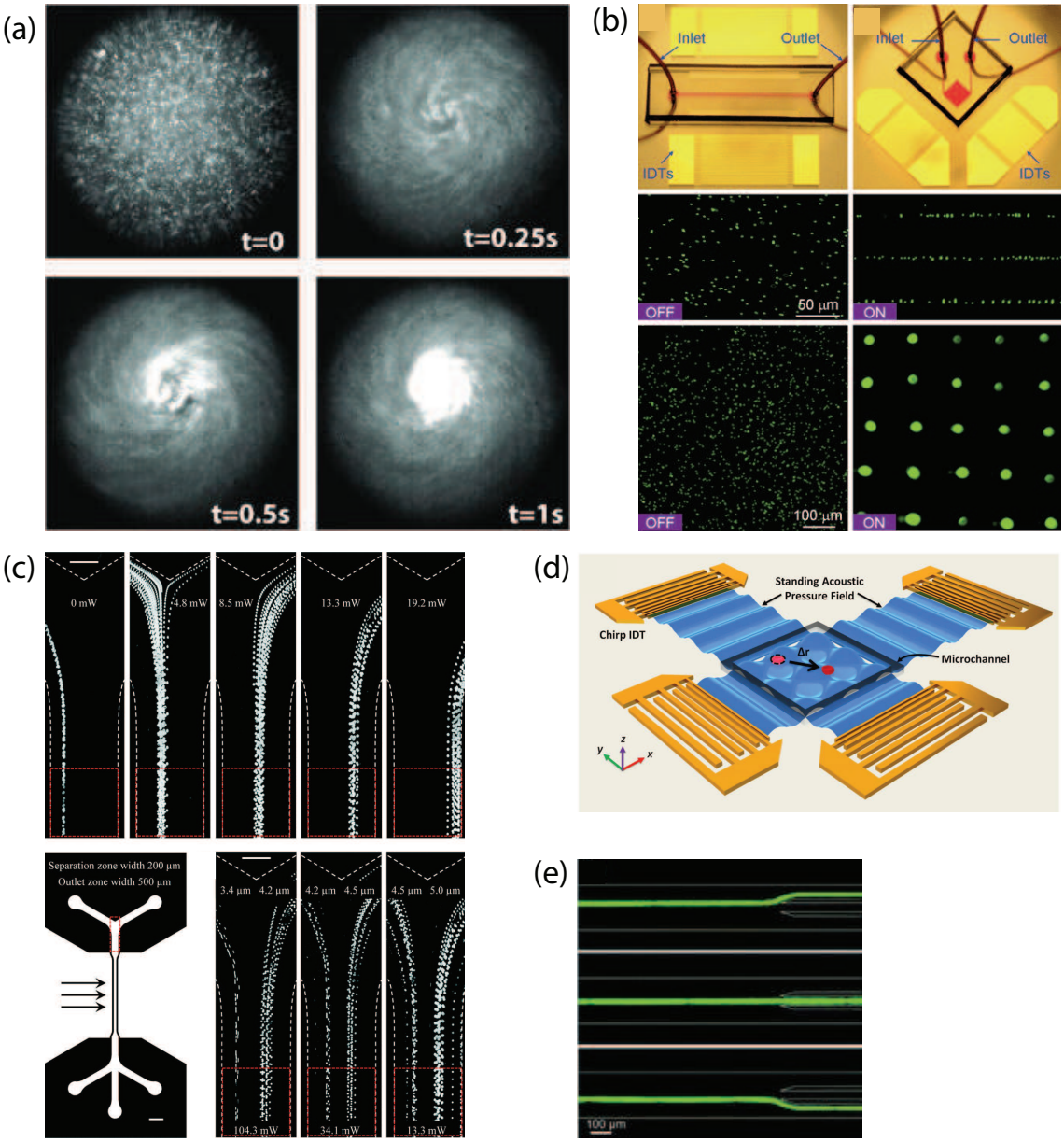

Figure 2.14: (a) Sequential images depicting the concentration of particles utilising TSAW induced acoustic streaming forces. Reprinted with permission from [25]. Copyright 2008, AIP Publishing LLC. (b) SSAW based particle concentration of particles in lines (1D collection; two parallel IDTs) and clusters (2D colelction; two orthogonal IDTs). Reproduced in part from [26] with permission of The Royal Society of Chemistry. (c) Sorting of particles with submicron size differences based on a TSAW system. Reproduced in part from [27] with permission of The Royal Society of Chemistry. (d) A SSAW acoustic tweezer system allowing for precise particle translation and control. Reproduced from [28]. Copyright 2012 National Academy of Sciences, USA. (e) A continuous flow cell sorting system using a tunable SSAW. Reproduced in part from [29] with permission of The Royal Society of Chemistry.

Phenomena such as acoustic radiation forces and acoustic streaming are the basis mechanisms of most SAW based microfluidic devices. These forces can be used individually or simultaneously to manipulate particles, biological cells and fluid interfaces within microfluidic systems. Acoustofluidic SAW systems have been used to demonstrate applications such as atomization of bulk fluids, [139, 202, 203] fluid mixing, [25, 204, 205] fluid translation [140], pumping, [206] particle/cell concentration, [25,26] and sorting. [27,207] Similar to the applications section of BAW (Section 2.4.1), the focus of discussion here will primarily be focused on particle/cell concentration and sorting techniques enabled by SAW, in line with the scope of the thesis. Both, TSAW and SSAW, have been used to demonstrate particle concentration and sorting independently.

Shilton *et al* [25] placed a droplet containing microparticles such that a portion of the droplet's width is in line with the TSAW. The resultant rotational pattern induced by acoustic streaming produces a high shear gradient that results in particle concentration in the center of the chamber as shown in Fig 2.14 (a). TSAWs have also been utilised to demonstrate particle deflection. Skowronek *et al* [208] characterised the onset of deflection occurs when the critical value $\xi_c \cong 1.28 \pm 0.20$, where the dimensionless parameter,ξ is given by,

$$\begin{aligned} \xi &= k_f r \\ &= \frac{2\pi r}{\lambda_{aco}} \end{aligned} \tag{2.82}$$

Utilising this relationship, TSAW has successfully demonstrated sorting of sub-micron particle size differences (see Fig. 2.14 (c)), [27] and size-selective particle sorting in an anechoic chamber. [207] Furthermore, density [209] and adhesive [90, 210] property based sorting within sessile droplets has been reported. In 2014, Schmid *et al* [211] showed using TSAWs, fluorescence activated continuous sorting of cells can be performed.

On the other hand, SSAW based systems have been employed over a range of particle collection, trapping and sorting applications. Particle alignment into parallel lines and clusters [26] within a 2D field as shown in Fig. 2.14 (b). Furthermore, two-dimensional single cell patterning [212] has been achieved by driving the excitation frequency close to that of the cell size, therefore, the inability to host more than one cell in a single acoustic well. In continuous systems, particle focusing for flow cytometry, [213] purification, [214] cell enrichment [215] and bacteria separation [216] have been realised as well utilising SSAW. Furthermore, a virtual deterministic lateral displacement device that consists of only a single set of IDTs to perform size deterministic separation within a SSAW field. [217]

Despite the extensive work carried out and demonstrated using SAW based devices for particle concentration and sorting, there has been very little work carried out for diagnostic purposes whereby only a very small amount of sample size is available. Besides, work carried out in sessile droplets, [25,90,209,210] investigation into bath process systems has been sparse. Simultaneous concentration and sorting of particles with a few micron

size difference has rarely been reported. In Chapter 4, a method that simultaneously employs TSAW and SSAW is proposed to concentrate and sort particles based on size within a static fluid system, requiring minimal sample volume.

Chapter 3

Batch Process Particle Separation using Bulk Acoustic Waves

3.1 Overview

Despite extensive research into size deterministic particle sorting within acoustofluidic continuous flow systems, investigation into static (i.e. batch process) fluid systems has been very limited. As discussed in Chapter 2 (Section 2.1), batch process systems are essential when sample volumes are scarce. In this chapter, emphasis was placed on establishing a method of separating particles of distinct sizes from each other within a batch system. Thus, the need for larger sample volumes within conventional continuous flow particle sorting systems for can be eradicated. A BAW system is proposed to separate two distinct particle sizes from each other within an initially mixed sample volume. The proposed system consists of a wetted rectangular open chamber, containing the mixed particle sample and utilises combination of acoustic radiation forces and acoustic streaming induced drag forces as the underlying mechanism of sorting. Acoustic radiation forces (ARF) are responsible for the concentration of the larger particles to a stable collection location at the bottom, chamber-liquid interface and the streaming induced drag forces help migrate the smaller streaming dominated particles to the upper stable locations at the liquid-air interface. FEA modelling suggests the critical separation size can be tuned based on scaling the size of the system, altering the dominance of ARF and streaming induced drag forces for a particular particle size. Experimentally, 3 μm particles were successfully separated from 10 μm particles with a 99% purity. Finally, the extraction of the separated 3 μm particles is demonstrated using a micro-sampling pipette.

3.2 Publication

Monash University

Declaration for Thesis Chapter 3
Declaration by candidate

In the case of Chapter 3, the nature and extent of my contribution to the work was the following:

Nature of contribution	**Extent of contribution**
Design and fabrication of devices, experimentation, development, results analysis, interpretation and writing	75%

The following co-authors contributed to the work:

Name	**Nature of contribution**	**Extent of contribution**
Ian Gralinski	Numerical modelling	20%
Assoc. Prof. Adrian Neild	Project Supervision	N/A

The undersigned hereby certify that the above declaration correctly reflects the nature and extent of the candidate's and co-authors' contributions to this work.

Candidate's Signature: [redacted]

Candidate's Name: Citsabehsan Devendran

Date: 30th November 2015

Main Supervisor's Signature: [redacted]

Main Supervisors's Name: Assoc. Prof. Adrian Neild

Date: 30th November 2015

Microfluid Nanofluid (2014) 17:879–890
DOI 10.1007/s10404-014-1380-4

RESEARCH PAPER

Separation of particles using acoustic streaming and radiation forces in an open microfluidic channel

Citsabehsan Devendran · Ian Gralinski · Adrian Neild

Received: 28 June 2013 / Accepted: 2 March 2014 / Published online: 12 March 2014

Abstract In this study, a method to separate particles, within a small sample, based on size is demonstrated using ultrasonic actuation. This is achieved in a fluid, which has been deposited on a flat surface and is contained by a channel, such that it has a rectangular wetted area. The system utilises acoustic radiation forces (ARFs) and acoustic streaming. The force field generates two types of stable collection locations, a lower one within the liquid suspension medium and an upper one at the liquid–air interface. Acoustic streaming selectively delivers smaller particles from the lower locations to the upper ones. Experimental data demonstrate the ability to separate two sets of polystyrene microparticles, with diameters of 3 and 10 μm, into different stable locations. Methods to reduce migration of larger particles to the free surface are also investigated, thereby maximising the efficiency of the separation. Extraction of one set of 99 % pure particles at the liquid–air interface from the initial particle mixture using a manual pipette is demonstrated here. In addition, computational modelling performed suggests the critical separation size can be tuned by scaling the size of the system to alter which of ARFs and acoustic streaming-induced drag forces is dominant for given particle sizes, therefore presenting an approach to tunable particle separation system based on size.

Keywords Acoustic radiation force · Particle manipulation · Ultrasonic standing wave · Open fluid · Sorting

1 Introduction

The concept of lab-on-a-chip devices necessitates research into technologies, which can deliver microscale components capable of pumping (Woias 2005), acting as valves (Rife et al. 2000), mixing (Tan and Neild 2012), sensing (Gattiker et al. 2008), acting as small-scale reactors (Gau et al. 1999) and sorting (Nam et al. 2011) amongst others. In the case of the latter, particle sorting, it is necessary to apply forces to microparticles suspended in a fluid. There are several mechanisms by which this is possible, including dielectrophoresis (Shafiee et al. 2010), optophoresis (Landenberger et al. 2012) and acoustophoresis (Petersson et al. 2005; Franke et al. 2010). In each case, the force contrast between the particle and suspension media causes the field, be it electrical, optical or acoustic, to exert forces on the particles driving them to the force potential global minimum and local minima. Whilst each approach offers advantages, this work will examine the use of acoustic forces due to the multiple potential minima which can be achieved (allowing stable separation of particles) and the ease with which a self-contained system can be fabricated.

The presence of an acoustic field in a fluid volume in which particles are suspended causes the exertion of three main types of forces. Firstly, the interaction of the acoustic field with the particle (assuming there is a mismatch in the acoustic properties) results in a force acting on a particle, known as the acoustic radiation force (ARF). This force, when time averaged over the period of an acoustic cycle, is nonzero; hence, net movement of the particle occurs

Electronic supplementary material The online version of this article (doi:10.1007/s10404-014-1380-4) contains supplementary material, which is available to authorized users.

C. Devendran · I. Gralinski · A. Neild (✉)
Laboratory for Micro Systems, Department of Mechanical and Aerospace Engineering, Monash University, Clayton, VIC 3800, Australia

(Gor'kov 1962). ARFs have been used to position suspended particles within a range of microfluidic systems, usually using standing waves. The results include the positioning of particles into planes in an acoustic filter (Hill et al. 2008; Glynne-Jones et al. 2012), lines in a channel (Neild et al. 2006), clumps in a microfluidic chamber (Shi et al. 2009a; Oberti et al. 2007), patterning in different geometries (Bernassau et al. 2013) or ultrasonic cages in a full 3D sound field (Manneberg et al. 2008). It has been shown that there are no direct or delayed damaging effects on cells handled in an acoustofluidic system (Hultström et al. 2007; Bazou et al. 2011) as a result of the employed acoustic field. The second type of forcing mechanism arises due to acoustic streaming; nonlinear terms in the Navier–Stokes equation give rise to body forces, which act on the fluid volume. Again these forces time-average to a nonzero value over an acoustic cycle, but as they act on the fluid, the result is steady fluid motion (Nyborg 1965). Suspended particles experience forces from the fluid motion in the form of drag. Acoustic streaming has been shown to be present in systems near vibrating plates, membranes, cylinders and spheres, in a Kundt's tube and near oscillating gas bubbles (Nyborg 1958). In terms of microfluidic systems, it is most widely used for mixing (Yaralioglu et al. 2004; Sritharan et al. 2006) rather than particle handling. The third forcing mechanism is termed the Bjerknes force or secondary ARF; this is an interparticle force that originates from the scattering of pressure field radiated by an oscillating particle or bubble and can be either attractive or repulsive (Leighton 1994). It has been used in the context of microfluidics to gather nanoparticles from solution by attraction to trapped microparticles (Hammarström et al. 2012).

Sorting of particles using ARFs has been demonstrated based on differences in the speed of sound and the mass density between particles and the surrounding fluid (Gupta et al. 1995; Petersson et al. 2007). A particle that is stiffer and denser than the suspending medium (i.e. positive acoustic contrast factor) will migrate to the nearest pressure node in a standing wave, whilst one that has a negative acoustic contrast factor will be trapped at the pressure antinode. This leads to particles of different types collecting in different stable locations. Particle sorting based on size is also achievable using ARFs, but typically all particles with a higher density and stiffness than the suspended medium move towards the pressure nodes. Hence, to achieve sorting in this case, it is necessary to stop the manipulation prior to all particles arriving at the node; in this way, sorting can be achieved based on the speed of migration towards the node (Johnson and Feke 1995).

If two mechanisms can be used which have a different relationship with a certain parameter (e.g. radius or density), then the combination of those two mechanisms can be used to separate particles with respect to that parameter. One such approach is the combination of acoustic streaming and Bjerknes forces, both of which occur in proximity to an acoustically excited oscillating bubble. This approach can cause selective particle trapping based on size or density, with the larger or denser particles being attracted to the bubble via dominant Bjerknes forces and the smaller or less dense particles being dominated by the streaming-induced drag force; hence, they follow the fluid streaming pattern (Rogers and Neild 2011).

A second approach using acoustic streaming-induced drag and ARFs has recently been demonstrated (Rogers et al. 2013). Size-based sorting was achieved, with populations of different sizes migrating to different stable locations. Specifically 6- and 31-μm particles (ratio 5.16) were separated into multiple lines in an open fluid volume contained by a rectangular chamber (Rogers et al. 2013). The work presented here is also focused on the utilisation of ARFs and acoustic streaming in an open fluid volume and brings both the understanding and the implementation of this approach to a new level. We are able to show that a sample consisting of an average of 99 % 3-μm particles (also contains $\leq$1 % of 10-μm particles) can be extracted from a mixed sample solution. This demonstrates that this method can be used to obtain purified solutions by an open system (cross-sectional view; sides and bottom enclosed with a top liquid–air interface), which has the advantage of low sample volume (no volume losses in pipes and syringes), no flow requirements and ease of access. To achieve this, the separation of particles as a function of how the channel is filled (i.e. the use of a pre-wetting buffer solution) and the actuation duration is examined. Through the optimal combination of these effects that high fidelity selective collection is possible. In addition, through modelling the system, it is possible to study the underlying mechanics and explore how the system can be tuned to separate different pairs of particle sizes. The ability to separate particles of small size differences and potential to tune the system to separate particles of different sizes based on requirements within open microfluidic devices leads to practical applications in sample preparation for biological and pharmaceutical drug testing. By placing a small sample on a prepared substrate, an almost pure portion of the smaller particles can be separated and extracted for further analysis, without volume losses associated with syringe pumps and pipes required for enclosed systems.

2 Methodology

2.1 Fabrication

To investigate the use of streaming and ARF as a method of separating particles into different stable locations based on

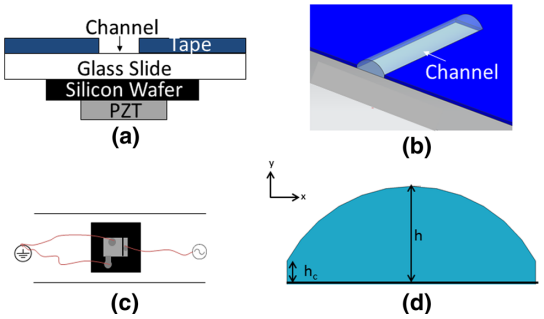

Fig. 1 **a** Cross-section schematic of the system consisting of a PZT (5.0 mm × 5.0 mm × 0.5 mm), silicon wafer (7.0 mm × 7.0 mm × 0.4 mm), glass slide (76.2 mm × 25.4 mm × 1.0 mm) and a channel (10.0 mm × 1.0 mm × 0.1 mm). **b** Perspective view of fluid-filled channel. **c** Electrical connections to the PZT. **d** Fluid profile of maximum height 0.4 mm (h), and channel height 0.1 mm (h_c)

their size, an open fluidic channel excited by an ultrasonic field was used. Subsequent modelling details how this achieves separation, but first the device itself will be described.

The test apparatus consisted of a 1-mm-thick glass slide (25.40 mm × 76.20 mm) on its underside was a square piece of 0.40-mm-thick silicon wafer (7.0 mm × 7.0 mm) attached with epoxy. The silicon wafer is used to increase visual contrast of the polystyrene particles when subjected to ultrasonic actuation. Beneath the silicon wafer, a piezoelectric transducer (Ferroperm PZ-26, lead zirconate titanate, PZT) (5.0 mm × 5.0 mm × 0.50 mm) was adhered using epoxy. A thin line of silver conductive paint was drawn from beneath the silicon wafer to an area outside the proximity of the attached PZT before adhesion to establish an electrical connection between these two points. Electrical wires were connected to the electrodes (PZT machined to produce a partition, i.e. discontinuity) using conductive paint as shown in Fig. 1. This fabrication technique is similar to that used by (Neild et al. 2007) the intention, being that the asymmetry of excitation allows the preferred establishment of asymmetric pressure fields. The channel was created using tape (vinyl masking tape); when fully filled, the fluid bulged due to surface tension as depicted in Fig. 1b where the excited electrode is parallel to the channel length (channel dimensions are included in Fig. 1).

2.2 Modelling

COMSOL multiphysics version 4.3, a finite element modelling package, was used to model the behaviour of the system presented here. A 2D cross-section of the fluid in the channel was modelled, similar to (i.e. does not illustrate the corner fillets) that shown in Fig. 1d, with channel dimensions 1.0 × 0.1 mm^2 (W × H). The fluid volume bulged above the top of the channel by 0.3 mm. One difference in the model compared to the fabricated device was that the top corners of the chamber had 0.01-mm fillets; it was found that this alteration was required for the model to converge.

In the model, the pressure acoustics module, laminar flow and particle tracing modules were used for the results presented here. A perturbation approach was taken to second order for the calculated velocity field given by $v = v_1 + v_2$, where v_2 is the acoustic streaming velocity. The pressure acoustics module was used to calculate the first-order pressure and velocity fields p_1 (in which the time component of p_1 is expressed as $e^{i\omega t}$), and $v_1 = -\nabla p_1/i\omega\rho_f$ [v_1 term is derived from the linear equation of the sound field: $p = \rho_f(\partial\phi/\partial t)$ and $v = -\nabla\phi$ (Gralinski et al. 2012)], where $i = \sqrt{-1}$, ω is angular frequency and ρ_f the fluid density. These were then used to calculate the body forces applied in the laminar flow module, as described by Nyborg (1965).

$$\langle \boldsymbol{f} \rangle = -\rho_f \langle (v_1 \cdot \nabla) v_1 + v_1 (\nabla \cdot v_1) \rangle \tag{1}$$

where angle brackets $\langle \cdot \rangle$ represent a time average and $\boldsymbol{f}$ is the body force. However, if looking at distances very close to the wall (i.e. approximately the viscous penetration depth, here 2 μm), a modified expression is required. This is because the first-order fields are not accurately described in these regions. This modification was implemented in COMSOL by multiplying the calculated body forces by the factor $1 + g(n)/2$, following Nyborg's parallel plate solution (Nyborg 1965). This scaling function is given by

$$g(n) = e^{-2n} - 3e^{-n}\cos n + e^{-n}\sin n \tag{2}$$

where $n = y/\delta$, η is the fluid viscosity, y is distance from the solid channel boundaries and the viscous penetration depth δ is given by

$$\delta = \sqrt{2\eta/\omega\rho_f} \tag{3}$$

The body forces are essentially unchanged for the region where $n > 5$, corresponding to a distance of approximately 2 μm from the walls for the system studied here. Once calculated, the body forces were applied in the laminar flow module to predict the acoustic streaming, v_2. The modification only produces valid results outside the viscous boundary layer (Lei et al. 2013). It is worth noting that using this approach it was possible to reproduce the results of Muller et al. (2012) with <1 % difference in streaming velocity and with less memory used in this method of solution. It is also noteworthy that the simulation method employed here is equivalent to that used in a recent paper by Lei et al. (2013). One drawback of this method is that it is only valid outside the boundary layer, i.e. >2 μm from the walls. In this work, however, the motion of particles in the bulk of the fluid was of interest.

Table 1 Particle, fluid and tape properties used in the models

Dyed polystyrene microspheres			
Density[a]	ρ_p	1,507	[kg m^3]
Speed of sound	c_p	2,350	[m s^1]
Mean diameter (3 μm)[a]	D_3	3.26	[μm]
Mean diameter (10 μm)[a]	D_{10}	10.02	[μm]
Water			
Density	P_f	998	[kg m^3]
Speed of sound	c_f	1,495	[m s^{-1}]
Viscosity	n	0.893	[mPa s]
Hydrophobic tape			
Density	p_t	225	[kg m^3]
Speed of sound[b]	c_t	2,100	[m s^{-1}]

[a] From particle data sheet provided by Sigma-Aldrich (manufacturer)

[b] Calculated using $c = \sqrt{E/\rho_t}$

For the pressure acoustics module, the bottom surface had a time-harmonic acceleration of the form $\omega^2 d_0 \sin(kx)$, where d_0 is a typical solid displacement on the order of a few nanometres and $k = 2\pi/\lambda$ is the wavenumber such that one wavelength fits across the channel. The top surface of the fluid was a pressure release boundary ($p = 0$), and the side walls of the channel were set as impedances ($Z = \rho_t c_t$). For the laminar flow module, all the solid interfaces were set as no-slip conditions and the fluid–air interface was set as a slip condition. The relevant properties of the particles and fluid are listed in Table 1.

Once the first-order (acoustic pressure) and second-order (laminar flow) fields were calculated, the particle tracing module was used to model the behaviour of the particles. The forces imposed on the particles were ARFs, drag due to streaming and the buoyancy-corrected weight force. The ARFs were defined using Gor'kov's formulation (Gor'kov 1962).

$$\langle U \rangle = 2\pi\rho_f R^3 \left(\frac{f_1}{3\rho_f^2 c_f^2} \langle p_1^2 \rangle - \frac{f_2}{2} \langle v_1^2 \rangle \right) \tag{4}$$

where $\langle U \rangle$ denotes the time-averaged force potential of a particle, c is the speed of sound, the subscripts f and p refer to fluid and particle properties, respectively, and R is the radius of the particle. The acoustic contrast factors f_1 and f_2 are given by

$$f_1 = 1 - \frac{\rho_f c_f^2}{\rho_p c_p^2} \tag{5}$$

$$f_2 = \frac{2(\rho_p - \rho_f)}{2\rho_p + \rho_f} \tag{6}$$

and the force is the negative gradient of the force potential $\boldsymbol{F}_{\mathrm{ARF}} = -\nabla\langle U \rangle$. The drag force was implemented using Stokes drag given by

$$\boldsymbol{F}_{\mathrm{drag}} = 6\pi\eta R(\langle v_2 \rangle - \boldsymbol{u}) \tag{7}$$

where $\boldsymbol{u}$ is the velocity of the particle.

The buoyancy-corrected weight force is given by

$$W_b = (\rho_p - \rho_f) V g$$

where V is the volume of a particle and g the acceleration due to gravity.

Finally, a 3D model of the system was not feasible to produce due to the large computational requirements for such an endeavour (up to 15 GB of RAM was used for these 2D models).

3 Experimental testing

Particle behaviour under a range of different parameters is explored through experimentation and compared to simulations. The experimental set-up (i.e. the piezoelectric unit as described in Sect. 2.1) is driven at the resonance frequency that results in the same mode found in the simulations using a frequency generator (Stanford Research Systems Model No. DS345) and power amplifier (Amplifier Research Model No. 25A1250A). The amplitude was varied to further investigate its effects on the separation yield. Imaging was performed using a stereo microscope (SZX16, Olympus) attached with a CCD camera (KP-D20AU, Hitachi) and data were captured using WINFast video capture card and Showbiz DVD2 software. Since no active cooling was fitted in the set-up, the system's temperature was measured using a FliR i7 thermal imaging camera. Later, the video was analysed by taking still images, and particle counting was performed using a pixel counter (ImageJ 1.46r). Extraction of intended particles was later carried out once the excitation is switched off. This was done manually using a microsampling pipette (1–5-μL PYREX® disposable microsampling pipette).

4 Results and discussions

4.1 Modelling

The fluid layer was excited at a resonance frequency of 1.919 MHz as determined by an eigen frequency analysis. Figure 2 shows the simulated forces acting on the suspended particles, as well as the particle trajectories in such a force field. The ARF is expressed as the sum of two parts in Eq. 4, of which $\langle p^2 \rangle$ dominates for the particles used in this work; hence, we can consider the collection of particles by first seeking minima in $\langle p^2 \rangle$ and then within these regions seeking maxima in time-averaged first-order velocity squared, $\langle \boldsymbol{v}_1^2 \rangle$ (Gralinski et al. 2012). Figure 2a

Microfluid Nanofluid (2014) 17:879–890

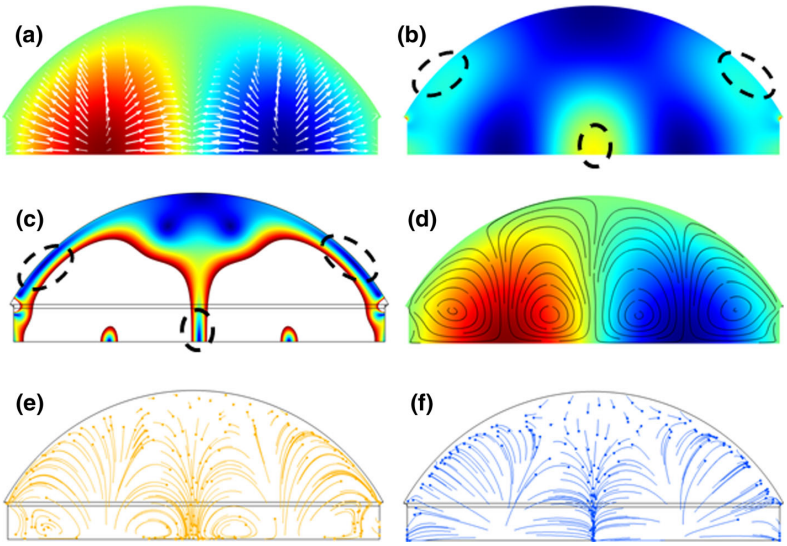

Fig. 2 **a** Plot showing the oscillation pressure (surface plots) $\langle p_1 \rangle$ and the ARF (*arrows*, range 0–0.4 MPa). **b** Plot of time-averaged first-order velocity squared $\langle v_1^2 \rangle$, showing particle collection regions (pressure is close to zero), and these are highlighted with *dashed ellipses* (range 0–0.04 m^2/s^2). We refer to the location at the base as the central node; the other two locations are at the liquid–air interface. **c** Plot of the magnitude of the ARF field scaled to show the structure of maxima and minima potential regions more clearly (range 0–0.4 MPa). ARF and acoustic streaming effects included: **d** second-order velocity streamlines are shown superimposed on the pressure field surface. Trajectories of **e** 1-μm particles (at $t = 30$ s) and **f** 10.02 μm (at $t = 0.5$ s) in the total force field (ARF, streaming-induced drag and buoyancy-corrected weight)

shows how the ARF acts to push particles away from pressure antinodes (located on both sides of the pressure node), causing particles to (depending on their initial location) move either to the bottom of the channel in the centre (i.e. the pressure node) or to the perimeter of the fluid volume. Within these locations of minimum pressure variation, particles migrate to locations of maximum $\langle \boldsymbol{v}_1^2 \rangle$. Hence, particles initially located at the periphery of the fluid are pushed up to the free surface, and trapping regions are created at the air–water interface by the weaker $\langle \boldsymbol{v}_1^2 \rangle$ term (see Eq. (4)); these areas are shaded green and light blue in Fig. 2b. By looking at the ARF on a reduced scale (Fig. 2c), it can be seen that there exist trapping locations on the top surface (left and right). Apart from the ARF acting on particles, there were also streaming-induced drag forces. The streaming velocity field (Fig. 2d) causes steady circulation of the fluid and is more dominant for smaller particles (i.e. streaming-induced drag forces are proportional to radius r, whereas ARF is proportional to r^3).

To demonstrate the difference in particle behaviour of different sizes, Fig. 2e, f displays snapshots of the positions of 1- and 10-μm particles and their trajectories from the randomly selected starting positions from which they were released. The trajectories shown for the small particles are not complete (rather cut off at the time of the snapshot); however, it can be seen that they follow a similar path to the streaming flow in the majority of cases. The larger particles, being affected mostly by acoustic radiation and weight forces, tend to collect at the bottom surface; the trajectories are much less curved with particles moving directly to the acoustic force potential minima. An alternative way to distinguish this difference in behaviour between the smaller and larger particles is to examine the streamlines at the centre of the channel. For streaming-dominated particles, the streamlines diverge here as shown in Fig. 2e, whilst they converge for radiation-dominated particles as demonstrated in Fig. 2f.

The simulations demonstrate the presence of two forcing mechanisms when the fluid is excited ultrasonically: ARFs and acoustic streaming. Furthermore, it can be seen that the behaviour of the small particles studied (1 μm) was dictated by acoustic streaming (swirling motion), whilst that of the large particles (10 μm) was dictated by the ARF causing a migration to distinct locations. An examination of how the dominant force for a given sized particle can be affected is presented. The motivation was to find a method in which there is control over the types of particles which can be separated; it would be useful to have different operating conditions or designs which would allow, for example, 3- and 10-μm, or 10- and 30-μm particles to be separated. For this to be the case, the dominant force affecting the particles must change. In the former example,

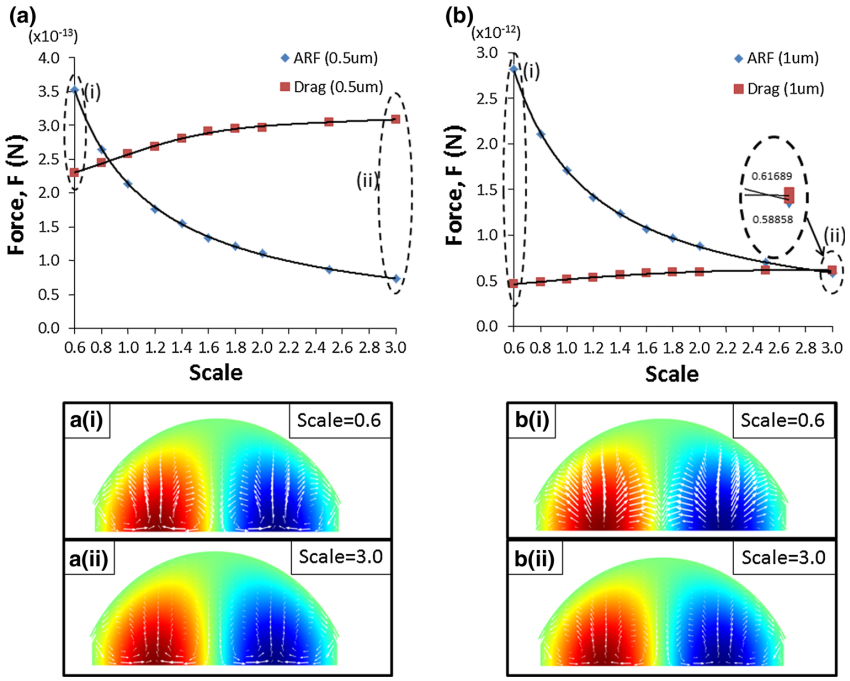

Fig. 3 Plots showing the variation of ARF and streaming-induced drag against the scale (modelled system relative to the original system) for **a** 0.5-μm (streaming dominated, i.e. not much change between scales) and **b** 1-μm particles (ARF dominated to streaming dominated as scale increases). *Insets* below are plots of the total force experienced by a given particle at the specified system scale, showing a change in dominance of either ARF or drag with a maximum scale of *a*(*i*) 25×10^{-5} Pa, *a*(*ii*) 12×10^{-4} Pa, *b*(*i*) 25×10^{-5} Pa and *b*(*ii*) 12×10^{-4} Pa

the 10-μm particles are the larger of the two sizes considered and are dominated by ARFs. For the latter example, the 10-μm particles are the smaller of the two and so require acoustic streaming-induced drag to dominate. Hence, the ratio of which force is dominant needs to be selectable.

In Fig. 3, a plot is given for the simulated maximum magnitude of the ARF and acoustic streaming-induced drag (refer to Eq. 7) exerted on 0.5- and 1-μm-diameter particles against the scale of the system (i.e. the modelled system size relative to the original system). In this plot, the maximum pressure amplitude in all cases was fixed at 0.4 MPa to allow for comparison. It can be seen that radiation forces decrease as the system size is increased, whilst acoustic streaming-induced drag forces increase slowly with system size. When the overall size of the system is increased whilst the pressure magnitude is kept constant, the pressure gradient will decrease, therefore decreasing the ARFs as well. However, it is also noteworthy that radiation forces increases with frequency in the case presented here, namely constant pressure amplitude across all scales. On the other hand, the acoustic streaming relationship with scale is more complicated. Whilst the viscous penetration depth is linked to one over the square root of frequency, as observed in Eq. 3, previous studies have shown that this is not the major factor determining changes in the streaming velocity when the fluid dimensions are far in excess of the penetration depth (Frampton et al. 2003, 2004; Hamilton et al. 2003). Instead, it is necessary to consider both alterations to the body force field (i.e. the forces acting on the fluid) and the fluid geometry to assess the swirling patterns formed in the fluid and the ease with which these patterns can be generated. Our numerical study shows that there is a slight increase in streaming with increasing scale in our system given the criteria of equal maximum pressure.

As the models presented here are in two dimensions, they do not take into account 3D effects, such as resonances along the length of the channel (Hagsäter et al. 2008). However, as will be seen in the experimental results, there were a few distinct sets of clumps of particles at the fluid–air interface along the channel, indicating that a mode with some variations along the length of the channel was being excited. The particle clumps were located in the planes where pressure maxima occurred. These regions are expected to act to translate particles towards fluid velocity maxima located along the free surface, albeit more slowly than the radiation forces produced by the $\langle p_1^2 \rangle$ term (i.e. $\langle p_1^2 \rangle$ dominates $\langle v_1^2 \rangle$). Furthermore, no separation of particles was seen close to the ends of the channel, likely due to the presence of a boundary affecting the pressure field in this region. Nevertheless, the behaviour of particles within the system could be reasonably well understood without consideration of 3D effects.

Microfluid Nanofluid (2014) 17:879–890

4.2 Experimental results

It was found experimentally that the 1-mm-wide channel, when driven at 1.75 MHz, displayed behaviour consistent with the same excited acoustic mode as achieved through simulation, i.e. a single node along the centre of the channel. The difference in frequency when compared to simulation is greater than would be expected in an enclosed chamber due to difficulties in matching between component layers of the device arising from fabrication flaws and matching exact the shape of the open fluid–air interface. However, the acoustic mode used was the same in the simulation and experiments. The 10-μm particles were collected at the nodes of the pressure field, and therefore predominantly in a line along the lower surface of the channel (observed from the top). On the other hand, 1-μm particles are predicted to follow the streaming patterns. It is also noteworthy that the simulations predict ARF potential minima on the upper surface of the fluid as shown in Fig. 2b.

Figure 4a shows the behaviour of 10-μm (blue) copolymer particles. It can be seen that over a short period of time (4 s), they form a line along the centre of the channel from the top view [an arrow is used to highlight these in (ii)] collecting in the central nodal location (as defined in Fig. 2b). In addition, smaller, less tight groupings can be seen either side of this line, and these are particles that migrated to the ARF potential minima at the liquid–air interface (an arrow is used to highlight this in (iv); the location is further described in Fig. 2b). In contrast, Fig. 4b shows the migration of 3-μm (red) copolymer particles. These particles were almost entirely collected at the top surface (very little is seen at the central node running horizontally through the centre of the image). For both particle sizes (and particle parameters used), the ARF potential minima are in the same locations and hence draw particles from the same areas. However, for the large particles, the population was split between the lower and upper surfaces; for the small particles, the majority were located at the upper surface. This cannot be explained by ARF alone; instead, we must also consider fluid motion. The increase in the dominance of acoustic streaming for small particles acts as a transport mechanism to deliver the particles from the lower surface to the upper free surface, where they then get trapped. The simulation doesn't show the trapping of the 1-μm particles considered, rather a continuous swirling, so the movement to the air–water boundary (the upper surface of the fluid) may in addition be aided by mechanisms outside the models limits, as follows: firstly, evaporation, which brings particles to the perimeter of fluid volumes (Shao et al. 2010); secondly, Bjerknes forces, which act between particles in a vibrating fluid (Weiser et al. 1984) due to scattered waves; in this instance, the scattered waves will be reflected by the upper surface (i.e. particle can be attracted to its own reflection); finally, there may be disturbances to the modelled pressure field as the upper water surface has a steady-state distortion which is not considered in the model (such distortion have been shown, in an extreme case, to generate water droplets in oil (Collins et al. 2013). Once on the upper surface, the particle will only be partially submerged (Xu et al. 2009) in the water so streaming-induced drag will become much reduced; hence, ARFs will dominate, and they will remain at the surface due to capillary forces (Li et al. 2008).

The simulations describe the swirling motion of 1-μm particles rather than the 3.26-μm particles used in the experiment. Indeed, the simulations predict that the 3.26-μm particles would behave in a very similar manner to the

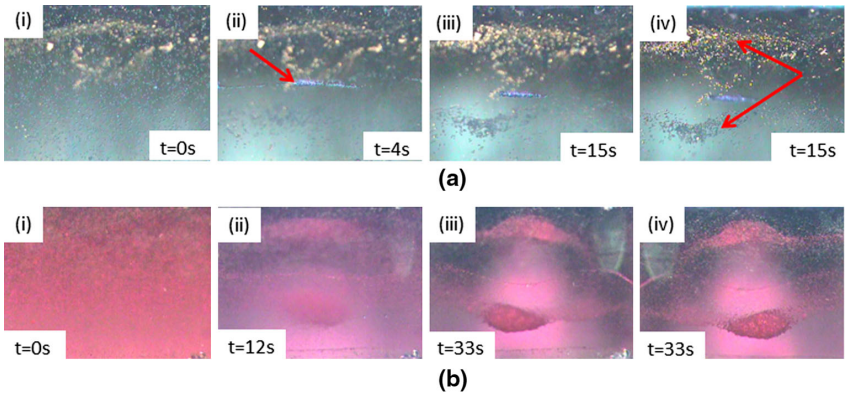

Fig. 4 Time series demonstrating particle collection patterns of **a** 10-μm and **b** 3-μm particles at a driving amplitude of 2.0 V_{pp} (channel *top view*). Figures correspond to (*i*) pre-excitation, (*ii*) during excitation, (*iii*) post-excitation (*bottom* focused) and (*iv*) post-excitation (*top* focused). In **a**, attention is drawn by use of an *arrow* in (*ii*) to the collection of particles along the central node at the base of the fluid volume, whilst in (*iv*), attention is drawn to the two *clumps* formed at the liquid–air interface

10-μm particles for which simulation data have been shown. Hence, it is necessary to model a smaller particle in order to show the streaming-dominated behaviour. In essence, the cut-off between streaming-dominated and radiation force-dominated behaviour occurs at a smaller particle size (<3 μm) in the simulations than in experiments. It is believed that this is due to changes in viscosity of the fluid arising as a result of temperature changes. The device was not temperature controlled, so as it was actuated heating occurred in two ways. Firstly, there have been some local heating within the pressure field due to bulk absorption in areas of high fluid particle motion (pressure antinodes). Secondly, and more significantly, there was bulk heating due to the heat generated in the piezoelectric plate (Johansson et al. 2013). Temperature of the system increased from 18 to 28 °C over a period of 30 s when actuated with a 1.0 V_{pp} signal (from the signal generator). The simulation did not include a method to vary temperature with time; instead, a constant value for the viscosity was used, which is commensurate with a temperature of 20 °C. The effect of underestimating the temperature for modelling parameters is that the viscosity is overestimated, and hence, the boundary layer-driven streaming is underestimated (Barnkob et al. 2012).

To demonstrate the effect of temperature rise and the resulting increase in streaming-based behaviour, experiments were conducted using 10-μm particles at different actuation voltages (0.1, 0.5 and 2.0 Vpp), and the results are shown in Fig. 5, where an actuation frequency of 1.75 MHz was used and the sample volume was 3.75 μL. It can be seen that the ratio between the number of particles on the upper surface (two side clusters on liquid–air interface) to the lower surface (central collection line) increases as the amplitude increases. In the absence of streaming, the expectation would be that the random initial position of each particle will lead them to migrate to the nearest ARF potential minimum. Hence, in each experiment, a similar split between particles on the lower and upper surfaces could be expected. This balance is upset by the presence of streaming, which offers a transport mechanism to take particles from one minima to another. As ARFs and streaming as shown in Eqs. 4 and 7, respectively, are equally dependent on the pressure amplitude, an increase in drive amplitude (in the absence of thermal effects) would not be expected to alter the split of particles between the upper and lower surfaces. However, as the amplitude is increased, the temperature also increases (verified by the thermal imaging camera). Therefore, at higher amplitudes, there is a decreased fluid viscosity (due to temperature increase) and as a result an increased effect of boundary-driven acoustic streaming (Barnkob et al. 2012). Consequently, the relative amplitudes of streaming-

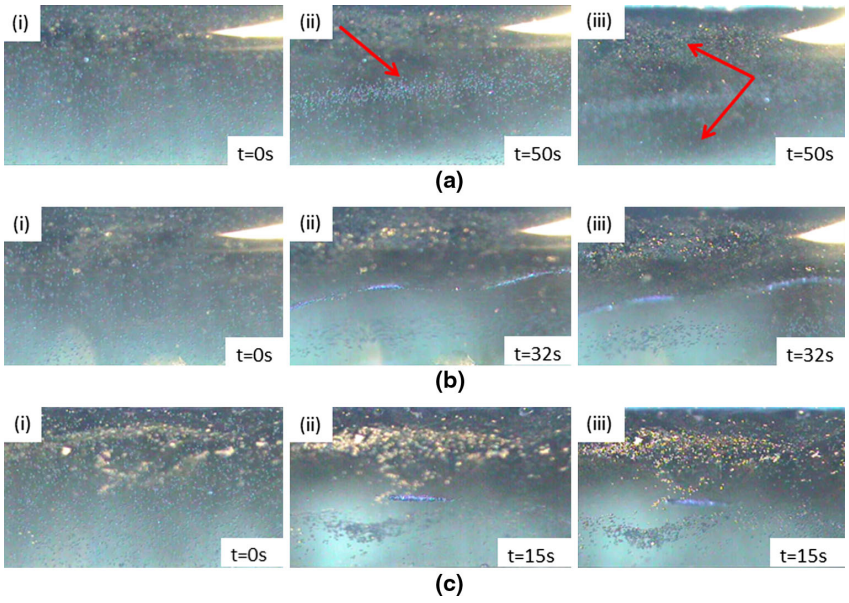

Fig. 5 Time series demonstrating particle collection time and pattern of 10-μm particles at a driving amplitude of **a** 0.1 V_{pp}, **b** 0.5 V_{pp} and **c** 2.0 V_{pp}. Figures correspond to (*i*) pre-excitation, (*ii*) post-excitation (*bottom* focused) and (*iii*) post-excitation (*top* focused). In **a**, *arrows* are used to point out collection at the lower central node (*ii*) and at the liquid–air interface (*iii*), these locations are the same across **b** and **c**. It can be seen that the ratio between the number of particles on the upper surface to that on the lower surface increases as the amplitude increases

induced drag forces and ARF alter, with the former becoming more significant; hence, more particles are moved to the free surface, which is evident in the experimental data. This suggests that operational temperature could offer a second mechanism to tune the system allowing the balance between ARFs and streaming-induced drag to be altered such that the transition between particle behaviour can be selected for optimal sorting. We believe that it is for these temperature-related reasons that the model shows results in which only 1.0-μm particles follow the streaming flow, something which the experiments show with 3.26-μm particles.

Even in the absence of thermal effects, the random distribution of the particles prior to actuation means that some of the 10-μm particles will inevitably migrate to the upper surface, simply due to start location, with particles moving to their nearest force potential minima, thereby decreasing the degree of particle separation. In order to achieve high-yield separation, the number of large particles moving to the upper surface must be minimised, these locations being reserved for the smaller particles. To this end, partially pre-filling the channel with buffer prior to adding the sample was investigated. The buffer contained no suspended particles and wetted the perimeter of the channel. In the case when there was no pre-filling (i.e. mixture of blue 10-μm particles only), 45 % of the particles remained at the desired separation position on the bottom surface of the fluid volume. This increased to 54 % with 1 μL of pre-fill. In addition to the pre-filling, repeated short excitation (each excitation cycle is 3 s), with 3 bursts is used, and 88 % of the blue 10-μm particles are collected at the lower surface (i.e. 53 and 73 % after first and second bursts of excitation, respectively). Reduction in the excitation time reduces the effect of acoustic streaming forces due to reduced thermal effects. In addition, there is less time in which the larger downward sedimentary pull of the larger particles is dominated by streaming drag forces (for those particles far from the pressure node).

Having demonstrated methods to limit the migration of the larger particles to the upper stable collection locations and having shown the tendency smaller particles have for migrating to these locations, the separation yield of the system was examined. Separation between the 3- (red) and 10-μm (blue) particles within a system operating at 1.75 MHz and at an excitation amplitude of 1.0 V_{pp} is shown in Fig. 6b. It can be seen that majority of 3-μm particles are separated from the 10-μm particles (it is noteworthy that <1 % of particles were observed to be at undesired locations at the end of the separation process). The system was also tested with a higher concentration of 10-μm particles (i.e. double the initial suspension volume of 10-μm particles while holding the initial suspension volume of the 3-μm particles constant), as shown in Fig. 6c. It can be seen from both experiments that using the two modifications (i.e. buffer pre-filling and burst signal excitation) established earlier with the 10-μm particles and

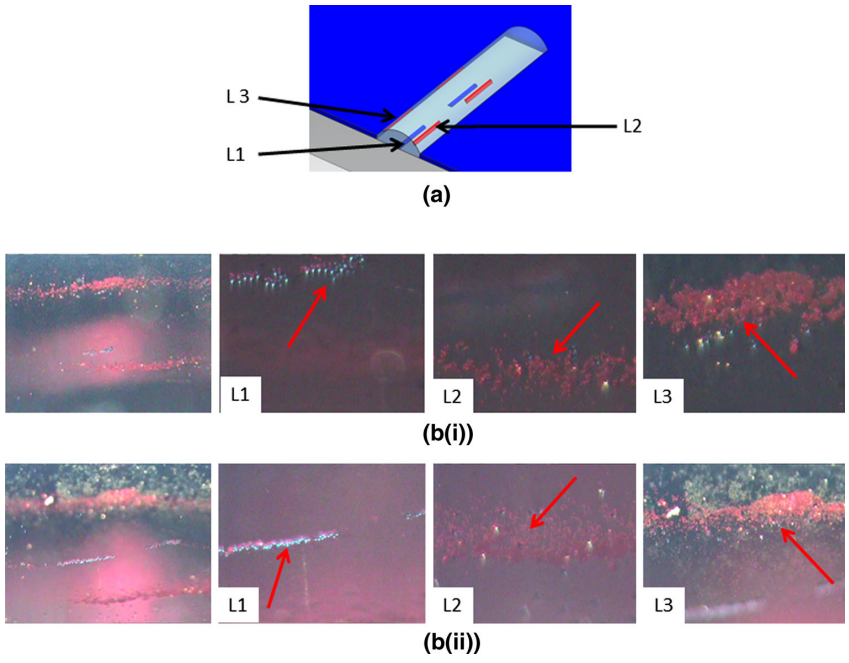

Fig. 6 Images showing the particle separation due to the interaction of ARFs and acoustic streaming-induced drag between 10- and 3-μm particles. In **a**, locations of the particles are depicted, the central nodal point which collects particles at the lower plane is labelled *L1*, the two collection locations on the liquid–air interface are labelled *L2* and *L3*. **b** Particles collected at these three locations (the first image has the whole channel width in view, the latter three are higher magnification views of each collection location, with the location indicated with an *arrow*) when **b(i)** a 1:1 volume ratio (37:1 particle number ratio) pre-filled with 1 μL of DI water and **b(ii)** used a 2:1 volume ratio (18:1 particle number ratio) pre-filled with 1.5 μL of DI water; both experiments used an amplitude of 1 V_{pp}

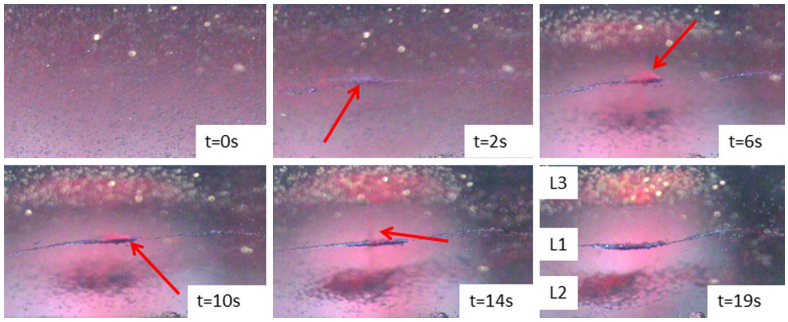

Fig. 7 A series of images over time demonstrates the role of acoustic forces and streaming in the system. 10-µm *blue* particles migrate to the nodes faster, already forming a predominantly *blue* streak along the central node (focussed on the *bottom* of channel) at 2 s. This is followed by the stacking of the smaller 3-µm particles on *top* of these, as shown at 6 and 10 s. Over time the streaming-induced drag forces peel the 3-µm particles to the free surface, as is shown at 14 s (a *thin line* of *red* particles migrates from the central node, upwards in the image perspective), until the collection consist of almost entirely *blue* particles, 19 s. The system was driven at 3.0 Vpp (colour figure online)

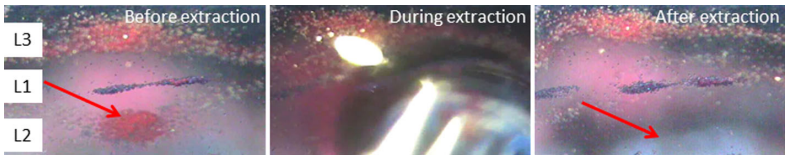

Fig. 8 Images demonstrating the ability to extract an almost pure sample of the smaller 3-µm particles from the free surface using a 1–5-µL PYREX® disposable microsampling pipette. An *arrow* marks the location of extraction in the before and after images

appropriate amplitude, the majority of the larger 10-µm particles are collected at the bottom surface and almost purely 3-µm particles are collected at the free surface. The population distribution of particles has been calculated using still images of the collection locations. For the data shown in Fig. 6b, there was a 50 % split between 3-µm red and 10-µm blue particles at the central node, whilst at the liquid–air interface 99.25 % of the particles were red (initially, there were 37 times as many 3-µm red particles to 10-µm blue particles; the introduction of particles was at a 1:1 5 wt% suspension volume ratio of 3 µm red and 10-µm blue particles). In case of Fig. 6c, the lower collection point at the central node had 27 % red particles, whilst the upper surface had 98.94 % red particles (here, there initially were 18 times as many 3-µm red as 10-µm blue particles). Clearly, the system works highly selectively in its separation of an almost pure population of the small particles. By way of comparison, collection here is able to separate particles of smaller size difference than that showed in Rogers et al. (2013) (i.e. 6 and 31 µm), where a 95 % separation yield is estimated. Shi et al. (2009b) showed that >80 % of larger latex particles (4.17 µm) were continuously separated from the smaller particles (0.87 µm) using standing surface acoustic waves (SSAW), whilst Nam et al. (2011) showed a separation yield of 99 % of red blood cells from platelets employing SSAW. In addition, the collection locations are stable once the excitation switched off is stable (i.e. particles do not migrate away to another location over an extended period of time).

With mixed particle populations, the larger particles migrate to the pressure node at the lower surface as do some of the smaller particles. The larger particles migrate significantly faster. The ARF is proportional to radius cubed in a standing wave field. The effect can be observed in Fig. 7, where the 3-µm red particles are stacked above the blue 10-µm blue particle clump present at this nodal location. As time progresses and streaming increases (from image to image), it can be seen that these outer small particles migrate from this location. The pressure node is also the extremity of the swirling flows established by acoustic streaming, so from this location, the smaller particles are taken around the outer streamlines of the vortex and as such directly to the upper surface of the fluid where they are subsequently trapped. This neatly demonstrates the interaction between streaming and radiation forces presented in this paper.

Once a desired separation yield is achieved and the excitation turned off, a microsampling pipette was used to extract the collected cluster of 3-µm particles as demonstrated in Fig. 8. During extraction, the particles collected on the other side of the top surface appear to be distorted.

However, once the microsampling pipette is retracted from the free surface, the collection of particles returns to their original location. This demonstrates the stability of the collected particles within a system that is no longer under excitation and that almost pure samples of smaller particles can be conveniently removed from a small volume of suspension containing a mixed population.

5 Conclusion

A method to separate particles based on their size has been developed using a single open channel microfluidic system. Computational modelling using COMSOL multiphysics was performed to predict the particle behaviour as a result of the induced acoustic field. Numerical models presented here suggest the ability to tune the separation of particles by scaling the size of the system. In addition to the computational models, experimentation was carried out and results presented. Migration of larger particles to the free surface was significantly reduced by altering the excitation amplitude, the use of short excitation bursts and pre-filling the channel with a buffer (i.e. DI water) prior to the delivery of the particle mixture. Separation between 10- and 3-μm particles was achieved as their difference in migration patterns was exploited at a single frequency, resulting in a simple size-dependant particle separation mechanism employing two mechanisms simultaneously (i.e. ARFs and acoustic streaming-induced drag forces). Furthermore, the separated particles at the free surface could be easily extracted from the system using a microsampling pipette. In addition, the developed system was open, which allowed easy access to particles using external mechanisms such as a microgripper and manual sampling pipettes from a sample of highly concentrated (99 %) smaller particles (3 μm) were easily extracted. Additional advantages of the system are low sample volumes (no volume losses in pipes and syringes) and no flow requirements. Short operation times (15–20 s) added to the versatility of this system and it was not significantly affected by evaporation.

Acknowledgments The authors gratefully acknowledge the support of the Australian Research Council in the form of Grant No. DP110104010.

References

Barnkob R, Augustsson P, Laurell T, Bruus H (2012) Acoustic radiation-and streaming-induced microparticle velocities determined by microparticle image velocimetry in an ultrasound symmetry plane. Phys Rev E 86(5):056307

Bazou D, Kearney R, Mansergh F, Bourdon C, Farrar J, Wride M (2011) Gene expression analysis of mouse embryonic stem cells following levitation in an ultrasound standing wave trap. Ultrasound Med Biol 37(2):321–330

Bernassau AL, Courtney CRP, Beeley J, Drinkwater BW, Cumming DRS (2013) Interactive manipulation of micro particles in an octagonal sonotweezer. Appl Phys Lett 102(16):4101

Collins DJ, Alan T, Helmerson K, Neild A (2013) Surface acoustic waves for on-demand production of picoliter droplets and particle encapsulation. Lab Chip 13(16):3225–3231

Frampton KD, Martin SE, Minor K (2003) The scaling of acoustic streaming for application in micro-fluidic devices. Appl Acoust 64(7):681–692

Frampton KD, Minor K, Martin S (2004) Acoustic streaming in micro-scale cylindrical channels. Appl Acoust 65(11): 1121–1129

Franke T, Braunmuller S, Schmid L, Wixforth A, Weitz DA (2010) Surface acoustic wave actuated cell sorting (SAWACS). Lab Chip 10(6):789–794

Gattiker F, Umbrecht F, Neuenschwander J, Sennhauser U, Hierold C (2008) Novel ultrasound read-out for a wireless implantable passive strain sensor (WIPSS). Sens Actuators A Phys 145–146:291–298

Gau H, Herminghaus S, Lenz P, Lipowsky R (1999) Liquid morphologies on structured surfaces: from micro channels to microchips. Science 283(5398):46–49

Glynne-Jones P, Demore CEM, Congwei Y, Yongqiang Q, Cochran S, Hill M (2012) Array-controlled ultrasonic manipulation of particles in planar acoustic resonator. IEEE Trans Ultrason Ferroelectr Freq Control 59(6):1258–1266

Gor'kov L (1962) On the forces acting on a small particle in an acoustical field in an ideal fluid. Sov Phys Dokl 6:773–775

Gralinski I, Alan T, Neild A (2012) Non-contact acoustic trapping in circular cross-section glass capillaries: a numerical study. J Acoust Soc Am 132(5):2978–2987

Gupta S, Feke DL, Manas-Zloczower I (1995) Fractionation of mixed particulate solids according to compressibility using ultrasonic standing wave fields. Chem Eng Sci 50(20):3275–3284

Hagsäter S, Lenshof A, Skafte-Pedersen P, Kutter JP, Laurell T, Bruus H (2008) Acoustic resonances in straight micro channels: beyond the 1D-approximation. Lab Chip 8(7):1178–1184

Hamilton MF, Ilinskii YA, Zabolotskaya EA (2003) Acoustic streaming generated by standing waves in two-dimensional channels of arbitrary width. J Acoust Soc Am 113(1):153–160

Hammarström B, Laurell T, Nilsson J (2012) Seed particle-enabled acoustic trapping of bacteria and nanoparticles in continuous flow systems. Lab Chip 12(21):4296–4304

Hill M, Townsend RJ, Harris NR (2008) Modelling for the robust design of layered resonators for ultrasonic particle manipulation. Ultrasonics 48(6):521–528

Hultström J, Manneberg O, Dopf K, Hertz HM, Brismar H, Wiklund M (2007) Proliferation and viability of adherent cells manipulated by standing-wave ultrasound in a microfluidic chip. Ultrasound Med Biol 33(1):145–151

Johansson L, Evander M, Lilliehorn T, Almqvist M, Nilsson J, Laurell T, Johansson S (2013) Temperature and trapping characterization of an acoustic trap with miniaturized integrated transducers—towards in-trap temperature regulation. Ultrasonics 53(5):1020–1032

Johnson DA, Feke DL (1995) Methodology for fractionating suspended particles using ultrasonic standing wave and divided flow fields. Sep Technol 5(4):251–258

Landenberger B, Höfemann H, Wadle S, Rohrbach A (2012) Microfluidic sorting of arbitrary cells with dynamic optical tweezers. Lab Chip 12(17):3177–3183

Lei J, Glynne-Jones P, Hill M (2013) Acoustic streaming in the transducer plane in ultrasonic particle manipulation devices. Lab Chip 13(11):2133–2143

Leighton T (1994) The acoustic bubble. Academic Press, London

Li H, Friend JR, Yeo LY (2008) Microfluidic colloidal island formation and erasure induced by surface acoustic wave radiation. Phys Rev Lett 101(8):084502

Manneberg O, Vanherberghen B, Svennebring J, Hertz HM, Onfelt B, Wiklund M (2008) A three-dimensional ultrasonic cage for characterization of individual cells. Appl Phys Lett 93(6):063901–063903

Muller PB, Barnkob R, Jensen MJH, Bruus H (2012) A numerical study of microparticle acoustophoresis driven by acoustic radiation forces and streaming-induced drag forces. Lab Chip 12(22):4617–4627

Nam J, Lim H, Kim D, Shin S (2011) Separation of platelets from whole blood using standing surface acoustic waves in a micro channel. Lab Chip 11(19):3361–3364

Neild A, Oberti S, Beyeler F, Dual J, Nelson BJ (2006) A microparticle positioning technique combining an ultrasonic manipulator and a micro gripper. J Micromech Microeng 16(8):1562

Neild A, Oberti S, Dual J (2007) Design, modelling and characterization of microfluidic devices for ultrasonic manipulation. Sens Actuators B Chem 121(2):452–461

Nyborg WL (1958) Acoustic streaming near a boundary. J Acoust Soc Am 30:329

Nyborg W (1965) Acoustic streaming. Phys acoust 2(Pt B):265

Oberti S, Neild A, Dual J (2007) Manipulation of micrometer sized particles within a micro machined fluidic device to form two-dimensional patterns using ultrasound. J Acoust Soc Am 121:778

Petersson F, Nilsson A, Holm C, Jönsson H, Laurell T (2005) Continuous separation of lipid particles from erythrocytes by means of laminar flow and acoustic standing wave forces. Lab Chip 5(1):20–22

Petersson F, Åberg L, Swärd-Nilsson A-M, Laurell T (2007) Free flow acoustophoresis: microfluidic-based mode of particle and cell separation. Anal Chem 79(14):5117–5123

Rife J, Bell M, Horwitz J, Kabler M, Auyeung R, Kim W (2000) Miniature valveless ultrasonic pumps and mixers. Sens Actuators A Phys 86(1):135–140

Rogers P, Neild A (2011) Selective particle trapping using an oscillating microbubble. Lab Chip 11(21):3710–3715

Rogers P, Gralinski I, Galtry C, Neild A (2013) Selective particle and cell clustering at air–liquid interfaces within ultrasonic microfluidic systems. Microfluid Nanofluid 14(3–4):469–477

Shafiee H, Sano MB, Henslee EA, Caldwell JL, Davalos RV (2010) Selective isolation of live/dead cells using contactless dielectrophoresis (cDEP). Lab Chip 10(4):438–445

Shao FF, Neild A, Ng TW (2010) Hydrophobicity effect in the self assembly of particles in an evaporating droplet. J Appl Phys 108(3):034512–034518

Shi J, Ahmed D, Mao X, Lin S-CS, Lawit A, Huang TJ (2009a) Acoustic tweezers: patterning cells and micro particles using standing surface acoustic waves (SSAW). Lab Chip 9(20):2890–2895

Shi J, Huang H, Stratton Z, Huang Y, Huang TJ (2009b) Continuous particle separation in a microfluidic channel via standing surface acoustic waves (SSAW). Lab Chip 9(23):3354–3359

Sritharan K, Strobl C, Schneider M, Wixforth A, Guttenberg Zv (2006) Acoustic mixing at low Reynold's numbers. Appl Phys Lett 88(5):054102–054103

Tan JN, Neild A (2012) Microfluidic mixing in a Y-junction open channel. AIP Advances 2(3):032111–032160

Weiser M, Apfel R, Neppiras E (1984) Interparticle forces on red cells in a standing wave field. Acta Acustica United Acustica 56(2):114–119

Woias P (2005) Micropumps—past, progress and future prospects. Sens Actuators B Chem 105(1):28–38

Xu L, Ng TW, Neild A (2009) Delicate selective single particle handling with a float-sink scheme. Appl Phys Lett 94(3):034103–034104

Yaralioglu GG, Wygant IO, Marentis TC, Khuri-Yakub BT (2004) Ultrasonic mixing in microfluidic channels using integrated transducers. Anal Chem 76(13):3694–3698

Chapter 4

Batch Process Particle Separation using Surface Acoustic Waves

4.1 Overview

The task of size-deterministic particle separation in batch systems is further explored in this chapter. The aim was to further reduce the particle size difference that can be sorted within static fluids. To realise this, a SAW based system is proposed. The choice of utilising SAW as the excitation mechanism was due to a several key reasons that are vital for achieving the desired separation performance. SAW enables the fundamental sorting mechanism proposed, as it allows the integration of TSAW and SSAW when employed within an acoustically absorbent (i.e. PDMS) chamber. Another key advantage of SAW, is the ability to operate at much higher frequencies, in contrast to BAW systems. As a direct result of operating at higher frequencies, f the acoustic wavelength in the fluid, λ_f is reduced to approach the size of the particle, which plays a key role in tuning the critical separation size. In addition, the size of the system can be further reduced (due to the decreased acoustic wavelength), thus minimising the required sample quantity. Finally, as SAW established acoustic fields are relatively independent of the chamber size and design, a range of frequencies can be utilised, allowing for the employment of a frequency sweep. This enhances the separation efficiency as the SSAW dominated particles are able to migrate beyond a wavelength, thus forming a smaller cluster of particles in the middle of the chamber. FEA modelling demonstrates the underlying sorting mechanism and suggests that by altering the acoustic wavelength employed for a particular particle size, the dominant forcing mechanism experienced by the particles can be tuned between TSAW and SSAW. Finally, two sets of experimental data demonstrate size-deterministic sorting of 5.1 μm from 7 μm particles using a frequency range of 60 MHz to 90 MHz and 3.1 μm from 5.1 μm between a frequency range of 70 MHz to 120 MHz.

4.2 Publication

This publication [33] is reproduced by permission of The Royal Society of Chemistry.

Monash University

Declaration for Thesis Chapter 4
Declaration by candidate

In the case of Chapter 4, the nature and extent of my contribution to the work was the following:

Nature of contribution	**Extent of contribution**
Design and fabrication of devices, experimentation, numerical modelling, development, results analysis, interpretation and writing	80%

The following co-authors contributed to the work:

Name	**Nature of contribution**	**Extent of contribution**
Nipuna R. Gunasekara	Numerical model benchmarking	10%
Dr. David J. Collins	Project Supervision	N/A
Assoc. Prof. Adrian Neild	Project Supervision	N/A

The undersigned hereby certify that the above declaration correctly reflects the nature and extent of the candidate's and co-authors' contributions to this work.

Candidate's Signature:

Candidate's Name: Citsabehsan Devendran

Date: 30th November 2015

Main Supervisor's Signature: [redacted]

Main Supervisors's Name: Assoc. Prof. Adrian Neild

Date: 30th November 2015

RSC Advances

PAPER

View Article Online
View Journal | View Issue

Cite this: *RSC Adv.*, 2016, **6**, 5856

Batch process particle separation using surface acoustic waves (SAW): integration of travelling and standing SAW†

Citsabehsan Devendran,[a] Nipuna R. Gunasekara,[a] David J. Collins[b] and Adrian Neild*[a]

Received 18th September 2015
Accepted 22nd December 2015

DOI: 10.1039/c5ra26965b

www.rsc.org/advances

Acoustic fields offer a versatile and non-contact method for particle and cell manipulation, where several acoustofluidic systems have been developed for the purpose of sorting. However, in almost all cases, these systems utilize a steady flow to either define the exposure time to the acoustic field or to counteract the acoustic forces. Batch-based systems, within which sorting occurs in a confined volume, are compatible with smaller sample volumes without the need for externally pumped flow, though remain relatively underdeveloped. Here, the effects of utilizing a combination of travelling and standing waves on particles of different sizes are examined. We use a pressure field combining both travelling and standing wave components along with a swept excitation frequency, to collect and isolate particles of different sizes in a static fluid volume. This mechanism is employed to demonstrate size-based deterministic sorting of particles. Specifically, 5.1 μm and 7 μm particles are separated using a frequency range from 60 MHz to 90 MHz, and 5.1 μm particles are separated from 3.1 μm using an excitation sweeping between 70 MHz and 120 MHz.

Introduction

Particle and cell separation is a fundamental step in a number of biological and industrial processes, where many methodologies accomplish this separation in a continuous throughput manner. Many of these devices operate by combining fluid drag forces with an externally applied force including those arising from magnetic,[1,2] optical,[3,4] dielectrophoretic (DEP)[5–7] and acoustophoretic[8–11] fields, or using the flow profile of the fluid as it passes contractions or obstacles.[12,13] For each of these methods, particles with different dimensions, shapes, and electric or mechanical properties experience different forces and therefore displacements. The requirement for an externally generated continuous flow, however, limits the ability for these methods to be applied outside laboratory settings and usually necessitates external pumps with the minimum volume requirements that this entails.

In contrast, batch processing can be applied to small, μl-scale samples and increase diagnostic detection efficacy, crucial in many biological processes.[14–16] The ability to perform sample preparation on-chip reduces time investment; this compliments the reduction of reagent usage, allowing low operational costs. Despite these advantages, there have been comparatively few studies in particle separation for static fluids. Previous methodologies for the batch-sorting of small samples include optical tweezers,[17] magnetic actuation[1] and locally induced flow from acoustic[18] or electrohydrodynamic streaming.[19] These methods are limited, however, in their separation efficiency (flow-based methods), complexity of operation (optical methods), or types of particles/cells that can be separated (magnetic methods). To tackle this, acoustic actuation offers easy on chip integration, the ability to use portable miniaturized circuits to actuate the acoustic field[20] and good biocompatibility.[21,22] In addition, acoustic force fields can be displaced[23] which permits the generation of particle mobility that is required for separation within a static fluid volume.

The disturbance of an acoustic field due to the presence of a particle, specifically one that differs in density and/or speed of sound with respect to the surrounding medium, results in a time-averaged acoustic radiation force (ARF) that acts on the particle. The force is a result of second order terms in the Navier–Stokes equation, which time-average over an oscillation to a non-zero value. As such the ARF acting on a particle leads to a net movement rather than an oscillation.[24] Whilst acoustic fields also lead to Bjerknes forces (forces arising from the scattered wave from a nearby particle) and acoustic streaming (a steady state swirling fluid motion), it is the acoustic radiation force which is most widely exploited for particle manipulation. Typically, this is through the excitation of either bulk acoustic waves[25–28] (BAW) or surface acoustic

[a]*Laboratory for Micro Systems, Department of Mechanical and Aerospace Engineering, Monash University, Clayton, Victoria 3800, Australia. E-mail:* [redacted]

[b]*Engineering Product Design Pillar, Singapore University of Technology and Design, Singapore*

† Electronic supplementary information (ESI) available. See DOI: 10.1039/c5ra26965b

View Article Online
Paper RSC Advances

waves[29–31] (SAW). The former seeks to excite resonances within the fluid volume using longitudinal or flexural modes coupled from a vibrating structure; the latter uses a spatially periodic electrical field to create a resonant condition on a piezoelectric substrate. In the case of SAW, a further distinction can be made between travelling SAWs (TSAWs), in which a wave propagates through the system, and standing SAWs (SSAWs) in which there are two counter propagating waves. Sorting within a continuous flowing fluid has been achieved using BAW,[32–34] TSAW[31,35–39] and SSAW.[40,41] In batch systems, with very small samples in contact with a substrate, separation has been shown using acoustic streaming in droplets,[18] in an open chamber[42] and in a channel.[43]

Here, we examine the use of acoustic radiation forces alone for particle separation in a batch system, and demonstrate that the controllability of this type of acoustic force allows highly specific separation. Our method utilizes a combination of several mechanisms made possible by SAW based actuation. Firstly and uniquely, we utilise both TSAW and SSAW; the former acts to push the particles across the chamber, the latter to capture particles in bands of minimum force potential. Secondly, we sweep the frequency of excitation, in doing so we average the force fields over a wide frequency range. Such an approach has been used to refine the force field in a droplet,[44] handle particles in multiple chambers,[45] and migrate particles across a chamber in a moving standing wave.[46] While the usage here is most akin to the latter example, we show that the final location of the particles is size dependant due to the addition of the travelling wave to the swept standing wave. Thirdly, utilising the ability of SAW systems to operate at high frequencies,[47] we are able to generate wavelengths, λ_f, that approach the diameter of the larger particles. Forces generated by TSAW and SSAW scale differently to particle radius, r ($F_{\mathrm{TSAW}} \propto r^6$,[35] and $F_{\mathrm{SSAW}} \propto r^3$,[24] if particle radius, $r \ll \lambda_f$). Furthermore, Skowronek *et al.*[48] demonstrated that TSAW is effective for particle deflection when the parameter, $\kappa \geq 1.28 \pm 0.20$, where $\kappa = k \times r$ (k is the wavenumber in the fluid). Hence the relative importance of each force type is particle size dependant; we show that the difference in response this gives rise to is further enhanced as λ_f approaches the size of the larger particle, r_{large} to operate above the critical κ parameter.[49]

We show that the cut-off radius between behaviour types (TSAW or SSAW dominated) is frequency range dependant, and demonstrate the separation of 3.1 μm from 5.1 μm particles, as well as 5.1 μm from 7 μm within a static sample.

Operating principle

Experimental

The system consists of a microfluidic chamber, cast in polydimethylsiloxane (PDMS), and bonded onto a 128° rotated Y-cut X-propagating lithium niobate, $LiNbO_3$ (LN) piezoelectric substrate. This substrate is patterned with four sets (each aligned 45° from the *X*-axis) of aluminium interdigital transducers (IDTs), which are arranged in two pairs arranged orthogonally to each other (Fig. 1). The speed of sound in LN differs with respect to the propagation direction, here in this setup it is approximately 3600 m s^{-1}.[50] Each set of IDTs is chirped,[51] meaning that there is a spatial variation in pitch between the electrodes (SAW wavelength, λ_{SAW} range; 20–70 μm), making them responsive to a range of frequencies. Each set of transducers consists of 34 finger pairs with individual finger widths between 20 μm and 70 μm with an aperture of 1140 μm. The actuation of two pairs of orthogonally oriented sets of IDTs permits the generation of a 2D acoustic field[52] within the microfluidic chamber when an oscillating (*i.e.* A/C) electrical signal is applied. This field can have both standing and travelling wave components, whose relative magnitudes depend on the power applied to each set of IDTs.

The device is held under a microscope (Olympus BX43) using a 3D printed frame where spring loaded contact pins make contact with the electrode pads on the LN substrate. The experiments are recoded at 15 frames per second using a microscope mounted camera (Dino-Eye AM4023CT). The electrical signal is provided by a combined signal generator and amplifier (Rohde &Schwarz HAMEG HM8134-3 and Amplifier Research 25A250A). This generator is capable of providing a swept frequency signal, in which the frequency is constantly changed from a lower frequency limit, f_{L}, to a higher frequency limit, f_{H}, in 1 MHz steps, with a set cycle time period, T_{CYCLE}. For separation of 3.1 and 5.1 μm particles a 70–120 MHz signal range over with $T_{\mathrm{CYCLE}} = 10.3$ s was used. For separating 5.1 μm and 7 μm the frequency range and T_{CYCLE} are 60–90 MHz and 6.45 s, respectively. The S_{11} values, a measure of input port voltage reflection coefficient (*i.e.* efficiency of the examined IDT; power transmitted into the LN to generate SAW) were assayed using a network analyser (PowerSAW Belektronig F20).

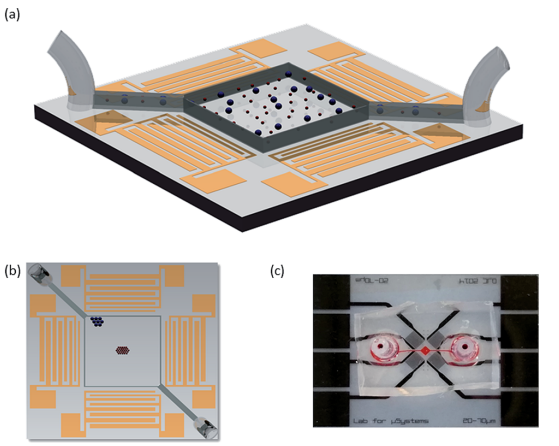

Fig. 1 (a) Diagram of the batch sorting device used in the experimental setup (particles dispersed homogenously as an initial condition) the chamber size is 707 μm (W) × 707 μm (L) × 25 μm (H), (b) top view of the idealised particle batch sorting (smaller particles (red) congregate in the centre and the larger particles (blue) at the top left corner) and (c) picture of the device used.

View Article Online
RSC Advances Paper

Analysis of the fluorescent particles intensity in the captured images allows time dependant data to be gathered on the collection of the particles. Firstly, a suitable RGB threshold was applied to the entire image such that areas in which a particle was present were attributed the value of 1 and the remaining areas the value of 0. Two areas measuring 100 × 100 pixels in the locations where the particles finish were identified, and the intensity analysed. The location of these areas was held constant throughout comparable experiments. The average intensity was then calculated for 5 distinct equally spaced time steps. To allow for a comparison over different samples accommodating for varying initial particle counts and distributions, the average intensity of each particle size is normalised by the total average intensity of both particle sizes within the analysis regions at corresponding time steps. It is this normalised average intensity distribution within the two regions which are used to demonstrate particle separation.

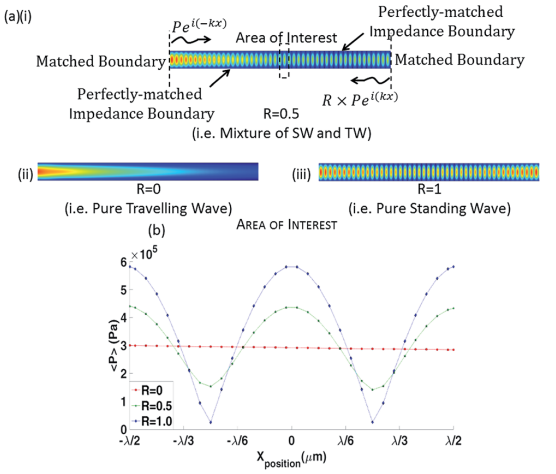

Fig. 2 (a) FE model depicting boundary conditions and 2nd order time averaged absolute pressure distribution when (i) $R = 0.5$ (mixed SW/TW), (ii) $R = 0$ (pure TW) and (iii) $R = 1$ (pure SW), (b) plot of the 2nd order time-averaged pressure field against the X-position (1 λ_f shown) for different R values.

Numerical simulation

The forces exerted on a particle that is much smaller than the acoustic wavelength are well understood for both standing waves[24] (SWs) and travelling waves[53] (TWs), though the simultaneous effects of both these wave components has not been investigated. In this work, a combination of these two types of waves and the effect it has on particles of various sizes are presented. The acoustic radiation force is a non-linear effect, arising from second order terms. This means that whilst the pressure fields arising from each of the wave types can be summed, such linear superposition is not possible for the force fields acting upon particle sizes that a comparable to the wavelength as investigated here.[54] To illustrate the effect of a mixed wave field in what is a complex system, a simple 2D model capturing the salient features has been developed using COMSOL Multiphysics. This model incorporates the effects of the TSAW and SSAW forces, though use of a swept frequency will not be examined.

When an acoustic wave encounters a suspended object (with differing density and/or speed of sound to the suspending medium) the wave will be diffracted and scattered. In order to avoid reflections such as those arising from a scattered wave, the fluid volume has been made long and thin, see Fig. 2(a). The upper and lower boundaries are such that a matched acoustic impedance boundary condition is imposed; this means that any scattered wave will propagate through it and reflections will be avoided. At each end of the chamber, boundary conditions need to be established such that a range of combinations of standing and travelling wave can be investigated. This necessitates a different boundary condition, so to keep scattered wave reflection to a minimum, these boundaries are located a long way from the scattering object and the boundaries are kept short. Each end of the chamber acts as a wave source; by keeping the edges narrow the fields that emerge in the centre of the chamber are in the far field region of the ultrasonic source[55,56] and so represent a reasonable approximation of a uniform sinusoidal waveform.

The amplitude of the leftward propagating wave is set to be a ratio (<1), R, of the rightward wave. This imbalance leads to a pressure field consisting of a standing wave (amplitude proportional to R, the standing wave ratio) and travelling wave (amplitude proportional to $1 - R$) component in the centre of the chamber, labelled the area of interest in Fig. 2(a) ($14\lambda_f$ from each end). Each end of the chamber also has a matched acoustic boundary layer, which allows waves of a defined wavenumber to pass through without reflection.

This model investigates the effects of the particle within a pressure field of a certain wavelength and does not directly simulate the piezoelectric LN substrate as we are primarily interested in the interaction between a particle and a combined SW/TW pressure field. The particle is assigned the same material properties as the polystyrene fluorescent particles used in the experiments ($\rho_p = 1050$ kg m^{-3}, $c_p = 2350$ m s^{-1}).

The time-averaged force acting on a solid particle of arbitrary size when the fluid viscosity is neglected can be calculated using:[57]

$$F = \frac{1}{2}\rho_f \int_{S_0} \left[\langle \boldsymbol{v}_1^2 \rangle - \frac{1}{\rho_f^2 c_f^2} \langle \boldsymbol{p}_1^2 \rangle \right] n \mathrm{d}S - \rho_f \int_{S_0} \langle (n.\boldsymbol{v}_1)\boldsymbol{v}_1 \rangle \mathrm{d}S \quad (1)$$

where, ρ_f and c_f (1000 kg m^{-3} and 1490 m s^{-1}) are the density and speed of sound of the fluid respectively, and $\boldsymbol{v}_1^2$ and $\boldsymbol{p}_1^2$ are the mean square fluctuation of the velocity and pressure respectively. The forces calculated have been benchmarked against cases shown by Dual *et al.*[57] In the pressure fields considered, the SSAW and TSAW forces on a particle are assessed over a distance of λ_f (from $-\lambda_f/2$ to $\lambda_f/2$ at $\lambda_f/12$ intervals).

View Article Online
Paper RSC Advances

Results and discussions

Numerical results

When a particle is located within the pressure field (Fig. 3(a)), eqn (1) can be used to calculate the forces acting on its surface over a single oscillation cycle, examples are shown in Fig. 3(b) to (d). The acoustic contrast between the particle and the fluid medium gives rise to these forces while also distorting the local pressure field. Fig. 3(e) shows the total force (*i.e.* after integration over the particle surface) as a function of radius, r, for both pure travelling wave and a pure standing wave. This allows a link to be made with established theories, in which the scaling with radius is known to differ; for a sphere, $F_{\mathrm{TSAW}} \propto r^6$,[35] and $F_{\mathrm{SSAW}} \propto r^3$,[24] provided $r \ll \lambda_f$. This difference in the relationship means that a larger particle is subject to a larger TSAW induced force than is a smaller one. What this figure shows is that as the radius is increased so that r approaches λ_f, this difference is further enhanced as the increase in force associated with the SW tapers off at a certain r value as it is increased, whereas F_{TSAW} continues to increase, yielding an r_{crit} above which $F_{\mathrm{TSAW}} > F_{\mathrm{SSAW}}$. Hence, to increase the influence of the travelling wave and so the sorting effect, smaller wavelengths should be used, thus increasing the size of the particle relative to the wavelength.

Both the orientation of the forces and the influence of the particle on the force field can be seen for increasing particle sizes in Fig. 3(b)–(d). In each case the particle is located in the same location, leftward of the pressure antinode, so a pure standing wave would act to move the particle further leftward towards the pressure node. Conversely, a pure TW acts to push the particle in the wave's propagation direction, hence rightward. It can be seen, from Fig. 3(b)–(d) the net force on the smallest, 3 μm, particles is leftward (toward the nodal position), whilst for the 5 μm and 10 μm particles is rightward, hence the change between dominance of SW and TW is shown as radius dependant (R value held constant at 0.3).

Fig. 3 addresses the dominant force at one location. In order to map out the spatial force field the simulated particle is sequentially translated with reference to the field, the resulting net force variation is shown in Fig. 4(a) and (b) for two different R values (1, 0.2) and three particle sizes (1, 4, and 7 μm). What can be seen is that for certain combinations of these two parameters the force is never negative, hence always rightward in nature, *i.e.* the TW force dominates over the whole wavelength. If the non-dimensional size of a particle, $a = r/\lambda_f$, is above a critical size, $a_{\mathrm{crit}} = r_{\mathrm{crit}}/\lambda_f$, the particle's trajectory (at all locations of a wavelength) will be dictated by the TW and migrate rightward, otherwise if $a < a_{\mathrm{crit}}$ the particle will ultimately be held in one location (where $F = 0$ and $\mathrm{d}F/\mathrm{d}x$ is negative). As expected in the pure SW scenario, Fig. 4(a), all three particle sizes will migrate to fixed locations. However, for an R value of 0.2, Fig. 4(b), the 7 μm will migrate rightward, whilst the 1 μm and 4 μm particles will be held static. This model demonstrates the principle of size based separation by use of a TW and SW, whereby larger particles are preferentially translated in this hybrid field.

Fig. 4(c) shows the value of the minimum force over a wavelength as a function of the standing wave ratio, R for a range of particle sizes. The plot shows that as the value of R increases, the dominant component of the acoustic field transitions from TSAW to SSAW gradually and thus the potential to tune r_{crit}. This is further demonstrated by plotting the value of a_c against R, Fig. 4(d) shows the crossover R value for a given r. Bearing in mind that the value of R is a measure of the relative amplitude, and so dominance, of the TW and SW, Fig. 3(e) also indicates, indirectly, a mechanism to tune the critical particle system, by operating at a lower or higher frequency the relative strength of the force generated due to TW or SW is altered, and hence the relative importance of these two wave components can be altered by R or frequency change (*i.e.* change in λ_f).

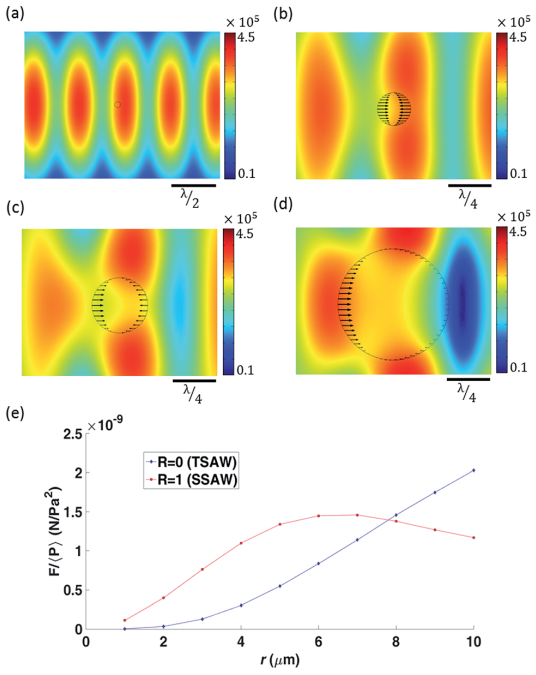

Fig. 3 2nd order time averaged absolute pressure distribution when $R = 0.3$ (*i.e.* 30% standing wave) ($\lambda_f = 30$ μm; $P = 1$ MPa) with (a) a 1 μm particle placed at $\frac{-\lambda}{12}$ from the centre, an acoustic radiation force (ARF) arrow plot (normalised arrows visualise the relative magnitude of the ARF acting at it's corresponding location)with particle sizes (b) 3 μm, (c) 5 μm and (d) 10 μm placed in the same location as (a) (colour bar scale units in Pa), (e) force, F by the 2nd order time averaged absolute pressure, <P> plotted against particle radius, r in μm for a pure TSAW (blue) and a pure SSAW (red).

Experimental results

The numerical results demonstrate several aspects of the underlying physics allowing particle separation, however it does not address the effect of sweeping the frequency of excitation. This plays two key roles; firstly, when considering the balance between the SW and TW it enhances the TW effect, and secondly when considering particle dominated by the SW, it

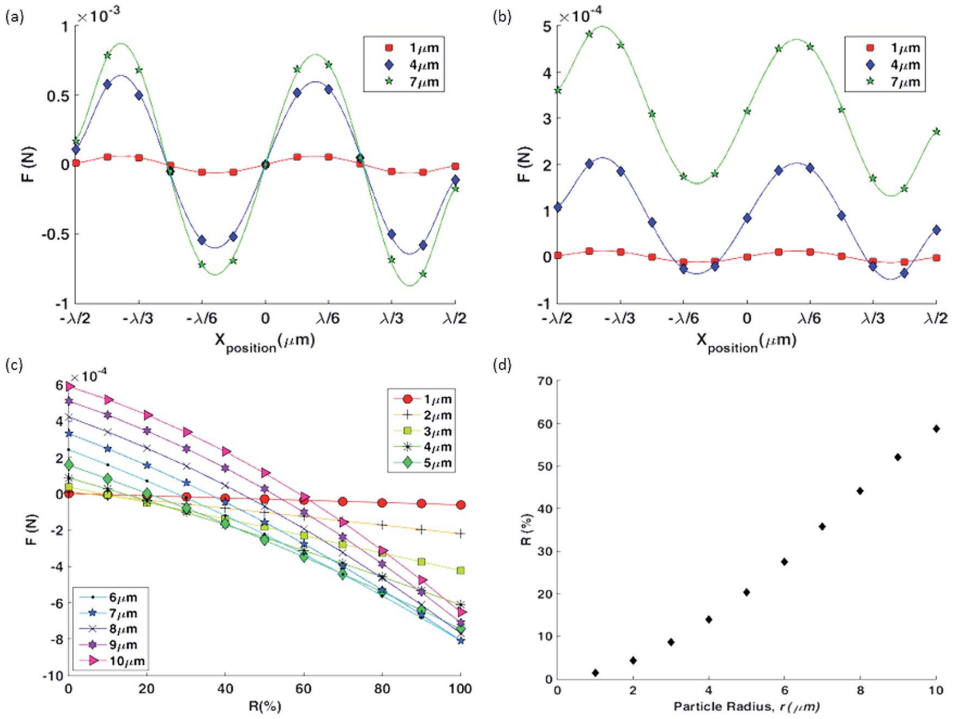

Fig. 4 FE model calculated ARF in the X-direction against X-position from the centre of the chamber ($\lambda_f = 30$ μm) with (a) $R = 1$ (*i.e.* 100% SSAW) and (b) $R = 0.2$ (*i.e.* 20% SSAW). (c) Minimum calculated ARF at $\frac{-\lambda}{8}$ against R for various particle sizes in μm, and (d) crossover SW ratio (*i.e.* ratio at which the SW becomes more dominant than the TW) against particle radius, r.

causes collection into a single location rather than large number of static pressure nodes due to the time-averaged effect of the force field.[46]

The R value, determining the balance between TW and SW, of the experimental system is set by the differing response of the IDTs to the electrical signal. The effective actuation amplitude is dependent on the S_{11} of the IDTs. The S_{11} parameter is the reflection coefficient due to the electrical impedance mismatch between the IDTs and the power source (this includes the influence of cables and electrical connectors). The S_{11} curves of the IDTs based on an identical electrical input signal are shown in Fig. 5(a), it can be seen that despite nominally identical electrode patterns, there are differences in these plots. By sweeping the frequency over a range, inevitably some part of this bandwidth will display differing S_{11}. Within this subset of frequencies, there will be a TW component as well as a SW component. The amplitude of the wave produced by each IDT set depends on the S_{11} parameter of the corresponding IDT. For instance, if an IDT set has a S_{11} parameter of 0.6, the transmitted electrical signal amplitude to that particular IDT is 40% (*i.e.* $(1 - S_{11}) \times 100\%$) of the input power. Therefore, the lower the S_{11} parameter, more electrical power is transmitted to the IDT set. Here, the amplitudes (for an identical input electrical signal) of the SW and TW respectively, at a given frequency, are A_1 and $A_2 - A_1$, where A_1 and A_2 are the wave amplitudes of the weaker and stronger sources respectively, for frequencies below 105 MHz. A larger S_{11} at a given frequency, as indicated in Fig. 5(a), means a weaker SAW (*i.e.* lower wave amplitude) emanating from that IDT (*i.e.* IDT 1 in this scenario). The effect of the variations in S_{11} is demonstrated in Fig. 5(b) which shows the spatial variation of surface displacement, measured by Laser Doppler Vibrometer (Polytec UHF-120) occurring between the IDTs when all four are actuated by the same electrical input. If the peak (marked by the black square in Fig. 5(b)) displacement magnitude is observed, the peak in Fig. 5(b)(i and iii) are similar, however, Fig. 5(b)(ii) has a smaller magnitude (*i.e.* lighter red comparatively; colour bar scale is identical for all three images). This is due to the presence of a TW and SW combination whereby, the resultant magnitude of a wave differs throughout a complete oscillation as depicted by the normalised amplitude plot in Fig. 5(b)(iv) corresponding to the same phase presented. The presence of different displacement magnitude peaks as shown in Fig. 5(b) would not be observed in a pure SW or TW system but only with a combination of SW and TW.

As observed in Fig. 5(a) the differences in S_{11}, thus, differences in the amplitudes of the waves are relatively small, less than the values of R used in the simulations. The reason is due to the frequency sweep. For a pure standing wave, the particles will move from the force potential minima, U (not to be confused with force, F; where $F = -\nabla U$) at one frequency, to that of the next frequency, this will bring them closer to the centre

View Article Online
Paper RSC Advances

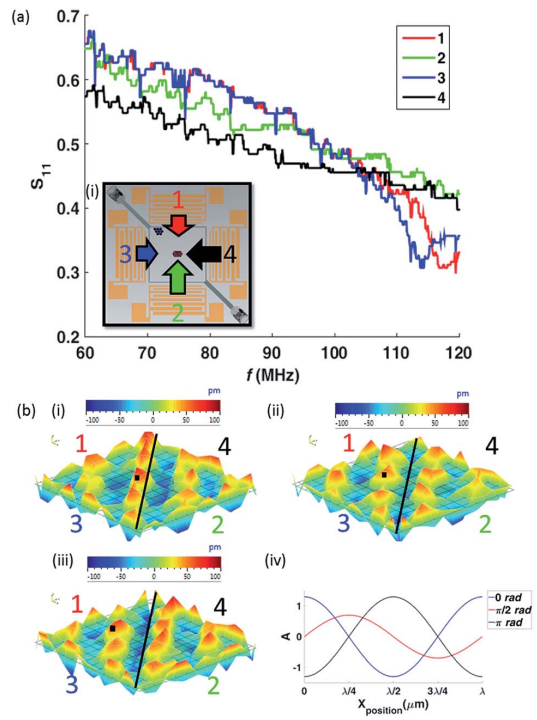

Fig. 5 (a) S_{11} parameter curve against frequency, f for each of the IDTs used as denoted by the inset (i) (arrow lengths depict the relative power transmitted to the corresponding IDT at 95 MHz). The value of $1 - S_{11}$ parameter, denotes the power transmitted to the device leading to the power disparity within the system giving rise to a combination of TSAW and SSAW. (b) Time series images of Laser Doppler Vibrometer (LDV) scan data demonstrating the presence of the TSAW at 95 MHz every $\frac{\pi}{2}$ rad phase (black line denotes centre diagonal of the scan area (constant position); black square denotes the tracked wave peak) (i) 0 rad (ii) $\frac{\pi}{2}$ rad (iii) π rad and (iv) depiction of normalised magnitude, A when $R = 0.3$ against X position at 3 different time intervals within a period (increments of $\frac{\pi}{2}$ rad) (1 λ_{SAW} shown).

of the chamber, with each frequency change, as each minima is offset from the previous one. In the context of single frequency of operation, as in Fig. 4, for TW dominated behaviour there are no local force potential minima. However, if the frequency is swept this condition is relaxed.

For the sake of simplicity in describing the phenomenon, we consider a simplified 1-dimensional system (it should be noted that the system utilised here in experiments is a 2-dimensional system), where a leftward TW component is added to the SW force potential (*i.e.* a slope is added to a sine wave). When the distance between the rightward local maxima and the local minima (d_a) is larger than between the same local minima and the local leftward maxima (d_b), we term this an asymmetrical force potential. To bring particles to the centre (in the 1-dimensional case) from the right-hand side is straightforward; it follows the pure SW case, but with further assistance from the TW. What is more interesting is the behaviour on the left-hand side of the chamber as this is where the two particle sizes behave differently. The minima of the SW dominated particles may be offset such that the particles are drawn to the centre (the offset is $<1/2(d_a + d_b)$), however due to the force potential asymmetry the same stepwise changing of the frequency could lead to a particle jumping from one local minima to the next leftward one if the offset exceeds d_b. Hence, even if local minima are present in the force potential, the use of a swept frequency system can mean that the TW causes migration away from the larger source (*i.e.* A_2 & A_4 for the case shown in Fig. 5(b)). Indeed, when a single frequency (120 MHz) was used, no difference in behaviour was observed between 3.1 μm and 5.1 μm diameter particles, *i.e.* neither were TW dominated. The power transmitted to each set of IDTs was not actively altered. As shown by Fig. 5(a), a disparity is observed for the IDT design used and therefore active control was not required to demonstrate the sorting mechanism. However, if precise control of the TW dominated particle's final location is required, active control of input power to individual sets of IDTs can be implemented.

The role of sweeping the frequency for SW dominated particles is to cause a longer migration trajectory than simply between an antinode and the nearest node in a single frequency system. Fig. 6 shows how, 5.1 μm particles (dominated by

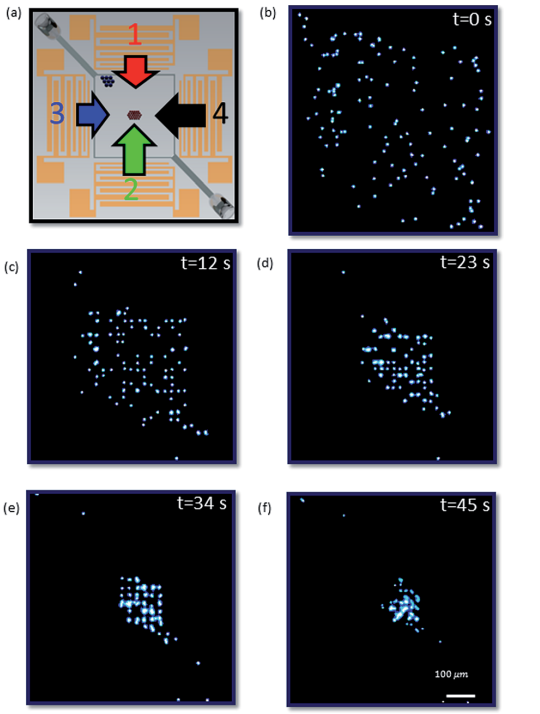

Fig. 6 (a) The orientation of the chamber in relation to the IDTs and depiction of the relative transmitter power for 90 MHz (*i.e.* f_H). Time series of images (depicted square is the entire chamber as shown in Fig. 1(a) as seen from above) demonstrating 5 μm particle collection dominated by SSAW as a result of the sweep over a range (60–90 MHz (1 MHz interval); 400 mV) of frequencies ($T_5 = 45$ s; 7 sweep cycles). From the initial dispersion (b) to the final position (f) (scale is equal over all images). See ESI Video 1† for multimedia.

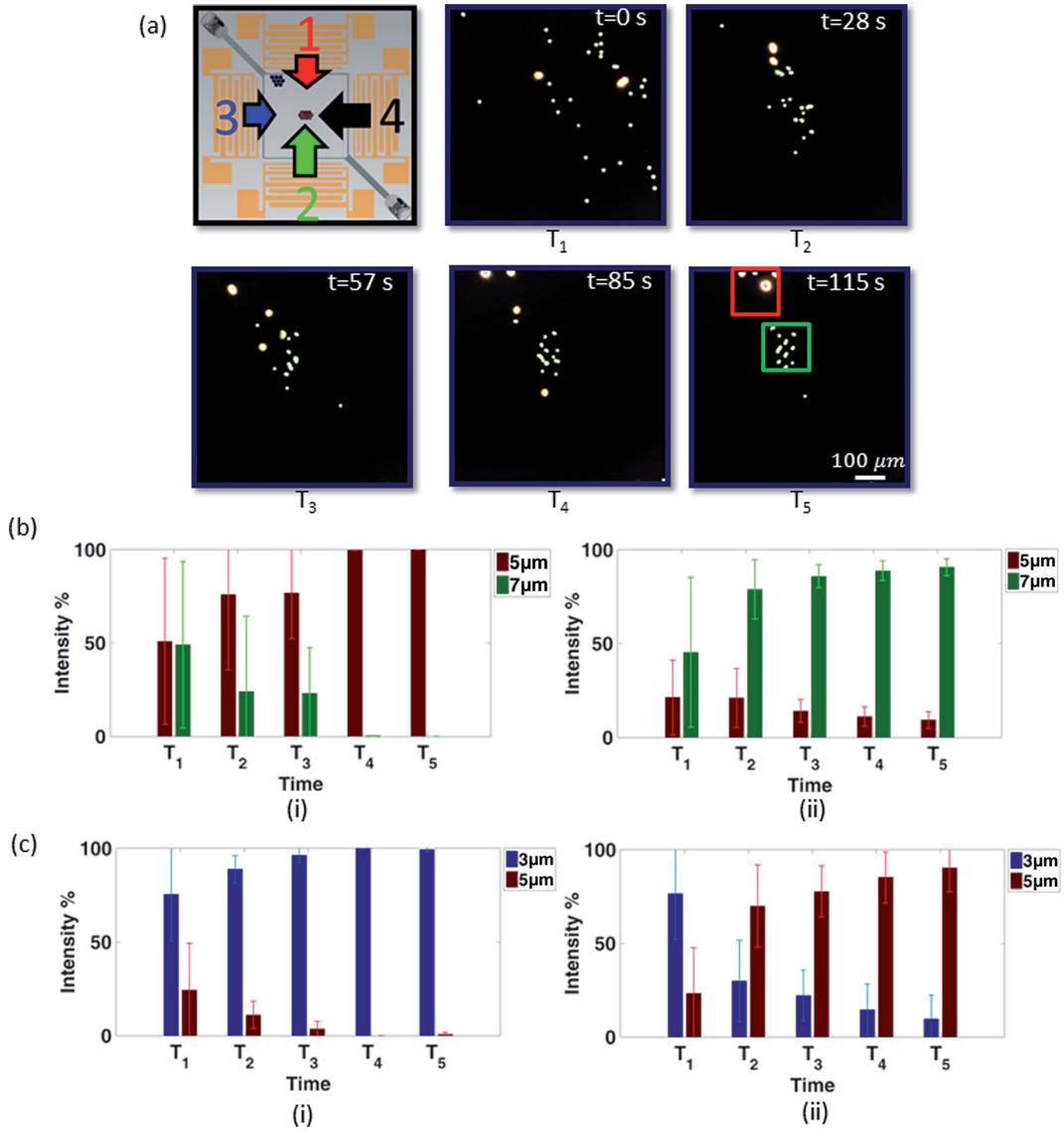

Fig. 7 (a) Chamber orientation and relative transmitted power depiction (at 90 MHz (*i.e.* f_H)) along with time sequence images of experimental data for particle separation of 5 μm (green) and 7 μm (yellow) particles (depicted square is the entire chamber as shown in Fig. 1(a) as seen from above) (scale is equal over all images) (see ESI video 2† for multimedia) and (b) average intensity percentage against time analysis data (i) centre of chamber (*i.e.* as depicted by the green square in (a)) (ii) side of chamber (*i.e.* as depicted by the red square in (a)) (350 mV; $T_5 = 115$ s). (c) Average intensity percentage against time analysis data based on experimental data of particle separation for 3.1 μm and 5.1 μm particles (i) centre of chamber (*i.e.* as depicted by the green square in (a)) (ii) side of chamber (*i.e.* as depicted by the red square in (a)) (250 mV; $T_5 = 210$ s).

SW effects, with $a < a_{crit}$) are first trapped in distinct locations at the pressure nodes[54] of a 2-dimensional field at a single frequency, and then as the frequency is raised from 60 MHz to 90 MHz, and the cycle repeated, gradually migrate to the centre of the chamber as result of the averaged force field over a sweep cycle.

Whilst particles dominated by the SW will migrate to the centre of the chamber when the frequency is swept, those dominated by the TW (over some part of the frequency sweep) will migrate away from the larger amplitude source (or sources if 4 IDTs are used). To demonstrate this, the microfluidic chamber was filled with fluorescent polystyrene particles of 2 distinct sizes and the IDTs actuated. In the first case, a sample with 5.1 μm (green) and 7 μm (yellow) particles were separated using a frequency range of 60 MHz (f_L) to 90 MHz (f_H) with a T_{CYCLE} of 6.45 s. As shown in Fig. 7(a), the particles are initially

dispersed throughout the chamber. Once the IDTs are excited, particles of both sizes are translated, with smaller particles shifted to the chamber centre. Midway through the experiment (T_3) most of the smaller 5.1 μm particles have been concentrated at the middle of the chamber as a result of the dominant SSAW ($a_{5\ \mu m} < a_{crit}$). In contrast, the 7 μm particles ($a_{7\ \mu m} > a_{crit}$) migrate to the top left corner of the chamber (*i.e.* A_2 & $A_4 > A_1$ & A_3; see relative power depiction in Fig. 7(a)). The bar graphs in Fig. 7(b)(i and ii) show the percentage of each particle within two areas of the chamber (see Fig. 7(a) for their location) as a function of normalized intensity. It can be seen that over time the proportion of 5.1 μm particles increase to 100% and the proportion of 7 μm particles decrease consistently at the centre of the chamber. In contrast, in Fig. 7(b)(ii), it can be observed that, the proportion of larger 7 μm particles increases while the smaller 5.1 μm particles decrease. It should be noted that the appearance of the yellow 7 μm particle present in the middle of the chamber as seen in Fig. 7(a) T_4 is due to particle migration drifting from the chamber outlet. However, this particle is also forced towards to the larger particle collection region (see ESI Video 2†). The total time to achieve complete separation of 5.1 μm and 7 μm particles excited at 350 mV is 115 s. The data presented is the average over 3 trials; the error bars show one standard deviation. As the initial location of the particles is random and the final position is determined by the response the acoustic field, it is clear that the error bars reduce significantly as the experiment progresses.

In Fig. 7(c), samples of 3.1 μm and 5.1 μm particles have been successfully separated. Again linking back to Fig. 4(b), to enter the regime in which TW becomes increasingly important the particle size needs to approach the wavelength, as the particles being separated are smaller in this experiment, this means an increase in frequency is required. Consequently, the excitation frequency range is increased, and set at 70 MHz (f_L) to 120 MHz (f_H) over a time period of 10.3 s. It can be seen that under these operational conditions the 3.1 μm particles collect at the center of the chamber whilst the 5.1 μm particles migrate away from IDTs 1 & 3 (*i.e.* stronger sources; see S_{11} curve in Fig. 5(a) at 120 MHz). In this case, the larger 5.1 μm particles migrate to the bottom right corner where, A_1 & $A_3 > A_2$ & A_4 as opposed to the earlier case whereby, A_2 & $A_4 > A_1$ & A_3. As such, the use of frequency range to tune the critical particle size for separation is demonstrated. The total time to achieve complete separation of 3.1 μm and 5.1 μm particles excited at 250 mV is 210 s.

Conclusions

The concentration and size-based separation of particles has been demonstrated in a static flow condition by exploiting a pressure field that combines both standing and travelling waves. These are excited by generation of counter propagating surface acoustic waves and modified using a continuously swept excitation frequency. Separation occurs due to the hitherto unexplored interplay between travelling and standing wave forces as the particle size approaches the acoustic wavelength, where the travelling wave force can exceed that of the standing wave. The use of a swept frequency further accentuates the effect of the travelling wave on larger particles and causes smaller particle migration with the moving standing wave field resulting in concentration from the entire volume of the sample chamber (rather than a quarter wavelength as for a single frequency excitation). The result is the larger particles are pushed across the chamber dominated by the travelling wave component, and smaller particles are collected at the center of the chamber due to the standing wave component. We demonstrate this methodology in the deterministic separation of 5.1 μm and 7 μm particles using a frequency range from 60 MHz to 90 MHz, and 5.1 μm from 3.1 μm particles using an excitation frequency range of 70 MHz to 120 MHz.

Acknowledgements

We gratefully acknowledge support received from the Australian Research Council, Grant No. DP110104010. This work was performed in part at the Melbourne Centre for Nanofabrication (MCN) in the Victorian Node of the Australian National Fabrication Facility (ANFF).

References

1 Y. Wang, Y. Zhao and S. K. Cho, *J. Micromech. Microeng.*, 2007, **17**, 2148.
2 N. Xia, T. Hunt, B. Mayers, E. Alsberg, G. Whitesides, R. Westervelt and D. Ingber, *Biomed. Microdevices*, 2006, **8**, 299–308.
3 M. P. MacDonald, G. C. Spalding and K. Dholakia, *Nature*, 2003, **426**, 421–424.
4 B. Landenberger, H. Höfemann, S. Wadle and A. Rohrbach, *Lab Chip*, 2012, **12**, 3177–3183.
5 H. Shafiee, M. B. Sano, E. A. Henslee, J. L. Caldwell and R. V. Davalos, *Lab Chip*, 2010, **10**, 438–445.
6 P. R. C. Gascoyne and J. Vykoukal, *Electrophoresis*, 2002, **23**, 1973–1983.
7 S. Park, Y. Zhang, T.-H. Wang and S. Yang, *Lab Chip*, 2011, **11**, 2893–2900.
8 J. Nam, Y. Lee and S. Shin, *Microfluid. Nanofluid.*, 2011, **11**, 317–326.
9 J. Nam, H. Lim, D. Kim and S. Shin, *Lab Chip*, 2011, **11**, 3361–3364.
10 J. Shi, H. Huang, Z. Stratton, Y. Huang and T. J. Huang, *Lab Chip*, 2009, **9**, 3354–3359.
11 F. Petersson, A. Nilsson, C. Holm, H. Jönsson and T. Laurell, *Lab Chip*, 2005, **5**, 20–22.
12 M. Yamada, M. Nakashima and M. Seki, *Anal. Chem.*, 2004, **76**, 5465–5471.
13 J. McGrath, M. Jimenez and H. Bridle, *Lab Chip*, 2014, **14**, 4139–4158.
14 H. M. Davey and D. B. Kell, *Microbiol. Rev.*, 1996, **60**, 641–696.
15 N. Sivanantha, C. Ma, D. J. Collins, M. Sesen, J. Brenker, R. L. Coppel, A. Neild and T. Alan, *Appl. Phys. Lett.*, 2014, **105**, 103704.
16 M. Eisenstein, *Nature*, 2006, **441**, 1179–1185.

17 Y. Tan, D. Sun, J. Wang and W. Huang, *IEEE Trans. Biomed. Eng.*, 2010, **57**, 1816–1825.
18 P. R. Rogers, J. R. Friend and L. Y. Yeo, *Lab Chip*, 2010, **10**, 2979–2985.
19 L. Y. Yeo, D. Lastochkin, S.-C. Wang and H.-C. Chang, *Phys. Rev. Lett.*, 2004, **92**, 133902.
20 L. Y. Yeo and J. R. Friend, *Biomicrofluidics*, 2009, **3**, 012002.
21 J. Hultström, O. Manneberg, K. Dopf, H. M. Hertz, H. Brismar and M. Wiklund, *Ultrasound in Medicine and Biology*, 2007, **33**, 145–151.
22 D. Bazou, R. Kearney, F. Mansergh, C. Bourdon, J. Farrar and M. Wride, *Ultrasound in Medicine and Biology*, 2011, **37**, 321–330.
23 X. Ding, S.-C. S. Lin, B. Kiraly, H. Yue, S. Li, I.-K. Chiang, J. Shi, S. J. Benkovic and T. J. Huang, *Proc. Natl. Acad. Sci. U. S. A.*, 2012, **109**, 11105–11109.
24 L. P. Gor'Kov, *Sov. Phys. Dokl.*, 1962, **6**, 773–775.
25 M. Hill, R. J. Townsend and N. R. Harris, *Ultrasonics*, 2008, **48**, 521–528.
26 P. Glynne-Jones, C. E. M. Demore, Y. Congwei, Q. Yongqiang, S. Cochran and M. Hill, *IEEE Trans. Ultrason. Ferroelectrics Freq. Contr.*, 2012, **59**, 1258–1266.
27 A. Neild, S. Oberti and J. Dual, *Sens. Actuators, B*, 2007, **121**, 452–461.
28 I. Leibacher, S. Schatzer and J. Dual, *Lab Chip*, 2014, **14**, 463–470.
29 M. Sesen, T. Alan and A. Neild, *Lab Chip*, 2014, **14**, 3325–3333.
30 D. J. Collins, T. Alan, K. Helmerson and A. Neild, *Lab Chip*, 2013, **13**, 3225–3231.
31 D. J. Collins, A. Neild and Y. Ai, *Lab Chip*, 2016, DOI: 10.1039/c5lc01335f.
32 L. Johansson, F. Nikolajeff, S. Johansson and S. Thorslund, *Anal. Chem.*, 2009, **81**, 5188–5196.
33 T. Laurell, F. Petersson and A. Nilsson, *Chem. Soc. Rev.*, 2007, **36**, 492–506.
34 A. Lenshof and T. Laurell, *Chem. Soc. Rev.*, 2010, **39**, 1203–1217.
35 G. Destgeer, K. H. Lee, J. H. Jung, A. Alazzam and H. J. Sung, *Lab Chip*, 2013, **13**, 4210–4216.
36 T. Franke, S. Braunmuller, L. Schmid, A. Wixforth and D. A. Weitz, *Lab Chip*, 2010, **10**, 789–794.
37 L. Schmid, D. A. Weitz and T. Franke, *Lab Chip*, 2014, **14**, 3710–3718.
38 G. Destgeer, B. H. Ha, J. H. Jung and H. J. Sung, *Lab Chip*, 2014, **14**, 4665–4672.
39 G. Destgeer, B. H. Ha, J. Park, J. H. Jung, A. Alazzam and H. J. Sung, *Anal. Chem.*, 2015, **87**, 4627–4632.
40 X. Ding, S.-C. S. Lin, M. I. Lapsley, S. Li, X. Guo, C. Y. Chan, I.-K. Chiang, L. Wang, J. P. McCoy and T. J. Huang, *Lab Chip*, 2012, **12**, 4228–4231.
41 D. J. Collins, T. Alan and A. Neild, *Lab Chip*, 2014, **14**, 1595–1603.
42 P. Rogers, I. Gralinski, C. Galtry and A. Neild, *Microfluid. Nanofluid.*, 2013, **14**, 469–477.
43 C. Devendran, I. Gralinski and A. Neild, *Microfluid. Nanofluid.*, 2014, **17**, 879–890.
44 S. Oberti, A. Neild, R. Quach and J. Dual, *Ultrasonics*, 2009, **49**, 47–52.
45 B. Vanherberghen, O. Manneberg, A. Christakou, T. Frisk, M. Ohlin, H. M. Hertz, B. Onfelt and M. Wiklund, *Lab Chip*, 2010, **10**, 2727–2732.
46 A. Haake, A. Neild, G. Radziwill and J. Dual, *Biotechnol. Bioeng.*, 2005, **92**, 8–14.
47 R. J. Shilton, M. Travagliati, F. Beltram and M. Cecchini, *Adv. Mater.*, 2014, **26**, 4941–4946.
48 V. Skowronek, R. W. Rambach, L. Schmid, K. Haase and T. Franke, *Analytical chemistry*, 2013, **85**, 9955–9959.
49 G. Destgeer and H. J. Sung, *Lab Chip*, 2015, **15**, 2722–2738.
50 A. Holm, Q. Stürzer, Y. Xu and R. Weigel, *Microelectron. Eng.*, 1996, **31**, 123–127.
51 V. M. Ristic, *Principles of acoustic devices*, Wiley, New York, 1983.
52 D. J. Collins, B. Morahan, J. Garcia-Bustos, C. Doerig, M. Plebanski and A. Neild, *Nat. Commun.*, 2015, **6**, 8686.
53 K. Yosioka and Y. Kawasima, *Acustica*, 1955, **5**, 167–173.
54 S. Oberti, A. Neild and J. Dual, *J. Acoust. Soc. Am.*, 2007, **121**, 778.
55 A. Holm, P. Wallner, W. Ruile and R. Weigel, *Ultrason. Symp. Proc.*, 1997, **1**, 153–156.
56 A. Neild, D. Hutchins, T. Robertson, L. Davis and D. Billson, *Ultrasonics*, 2005, **43**, 183–195.
57 J. Dual, P. Hahn, I. Leibacher, D. Moller, T. Schwarz and J. Wang, *Lab Chip*, 2012, **12**, 4010–4021.

Chapter 5

Optimisation of an Acoustic Resonator for Particle Manipulation in Air

5.1 Overview

Particle manipulation and transport in air is of great interest for batch process systems. Acoustic levitation enables a non-contact approach of trapping and examining mechanical properties of biological materials. [218] The use acoustic levitation has attracted interest in analytical and bioanalytical chemistry applications. [165] Utilisation of a non-contact approach allows for more accurate examination of chemical and mechanical properties as the inspected sample is isolated, therefore, reducing contamination and damage. Sample preparation procedures in levitated drops have been performed for various chemical procedures such as acid-base titration, solvent exchange , sample preparation for gas chromatography and analyte enrichment by evaporation. [219] Acoustic levitation and transport of particles within airborne systems have also been reported to sizes as small as 500 μm. [49,50,164,220] However, very small micron-sized (i.e. sub 100 μm) particle handling has not been reported.

Individualised micon-sized particle trapping for inspection purposes is proposed in this chapter. Knowledge of liquid based acoustofluidic systems is transferred across for operation in air. It is suggested that an increased frequency, thus, reducing the acoustic wavelength would enable individualised particle trapping. FEA modelling investigation accommodating for attenuation which is more significant at the MHz frequency range, suggests an optimum operational frequency exist for a given system size. The optimisation process was extended by employing a one-dimensional analytical wave-propagation model to obtain ideal layer thickness and material selection for maximum energy transfer. Based on the predictions gathered from the modelling, an experimental device was fabricated to successfully trap dense polymethyl methacrylate (PMMA) as small as 14.8 μm in diameter. This work serves as a precursor investigation into a full non-contact 3D individualised particle transport.

5.2 Publication

The following publication has been published and reprinted from [32]. Copyright 2015, with permission from Elsevier.

Monash University

Declaration for Thesis Chapter 5
Declaration by candidate

In the case of Chapter 5, the nature and extent of my contribution to the work was the following:

Nature of contribution	**Extent of contribution**
Design and fabrication of devices, experimentation, numerical modelling, development, results analysis, interpretation and writing	85%

The following co-authors contributed to the work:

Name	**Nature of contribution**	**Extent of contribution**
Assoc. Prof. Duncan R. Billson	Project Supervision	N/A
Prof. David A. Hutchins	Project Supervision	N/A
Assoc. Prof. Adrian Neild	Project Supervision	N/A

The undersigned hereby certify that the above declaration correctly reflects the nature and extent of the candidate's and co-authors' contributions to this work.

Candidate's Signature: 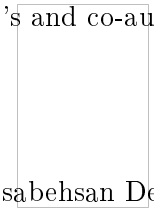

Candidate's Name: Citsabehsan Devendran

Date: 30th November 2015

Main Supervisor's Signature: 

Main Supervisors's Name: Assoc. Prof. Adrian Neild

Date: 30th November 2015

Sensors and Actuators B 224 (2016) 529–538

Contents lists available at ScienceDirect

Sensors and Actuators B: Chemical

journal homepage: www.elsevier.com/locate/snb

Optimisation of an acoustic resonator for particle manipulation in air

Citsabehsan Devendran[a], Duncan R. Billson[b], David A. Hutchins[b], Adrian Neild[a,*]

[a] Laboratory for Micro Systems, Department of Mechanical and Aerospace Engineering, Monash University, Clayton Campus, Clayton 3800, VIC, Australia
[b] School of Engineering, University of Warwick, Coventry CV4 7AL, United Kingdom

ARTICLE INFO

Article history:
Received 8 April 2015
Received in revised form 15 October 2015
Accepted 20 October 2015
Available online 23 October 2015

Keywords:
Microfluidic
Ultrasound
Particle manipulation

ABSTRACT

An acoustic resonator system has been investigated for the manipulation and entrapment of micron-sized particles in air. Careful consideration of the effect of the thickness and properties of the materials used in the design of the resonator was needed to ensure an optimised resonator. This was achieved using both analytical and finite-element modelling, as well as predictions of acoustic attenuation in air as a function of frequency over the 0.8 to 2.0 MHz frequency range. This resulted in a prediction of the likely operational frequency range to obtain particle manipulation. Experimental results are presented to demonstrate good capture of particles as small as 15 μm in diameter.

1. Introduction

Biomedical applications increasingly use micro-electromechanical systems (MEMS) technology and small particle capture in their implementation. Examples include the analysis of airborne particles and pathogens. Microgrippers can be used to manipulate such particles in liquid [1], capture cells in suspension [2] and characterize mechanical properties of individual biological particles [3], and are usually designed to grip particles by frictional forces [1,4–6]. However, these contact-based approaches can cause damage due to the mechanical forces involved [3]; they can also encounter problems with stiction, due to significant adhesive (capillary) forces that can be present at such small scales [7–9]. Stiction effects can be reduced by using surface coatings [10] and/or by minimising contact surface area by modifying the tip geometry of the gripper, for example [11]. However, a non-contact approach is required when handling delicate samples which may be damaged by frictional gripping methods.

A number of non-contact approaches to particle manipulation are available. These include optical traps [12] and electric field methods (dielectrophoresis or DEP) [13]. These methods have numerous applications, although miniaturisation and integration within MEMS-based devices is problematic. A high optical density is required for optical trapping, and the DEP method only operates over a limited spatial range. A third method, to be investigated here, uses forces generated by an ultrasonic field [14,15]. This technique, also known as acoustophoresis, can be integrated into small-scale devices to manipulate particles and droplets in both liquids and gases [16,17].

The acoustic method relies on differences in material properties between the particles and the medium, as this generates acoustic radiation forces (ARFs). These non-linear forces act directly on the suspended matter, causing a migration over multiple oscillation cycles [18]. Acoustic manipulation, using ARF, has been widely applied in microfluidic devices, due to good biocompatibility [19], relatively simple instrumentation, robust architectures and good on-chip integration possibilities. Capabilities such as positioning of particles in a single plane for filtration (acoustic filters) [20,21], within a microfluidic channel [22] and within three dimensions [23] have been demonstrated. It can also be used for particle sorting and separation [24,25], and for the production and manipulation of aqueous droplets in oil [26,27].

While manipulation of particles in microfluidic liquid based systems is well established, there are only a handful of examples for manipulation of small particles in air. Acoustic levitation and transport of particles in air have been reported in the literature [17,28–30], as has the ability to trap liquid droplets [31,32]. There have been several other resonator designs that have been explored to successfully levitate particles and droplets in air using acoustics. Design of an acoustic horn attached to solid plates and blocks [33–35] have been used to excite the air cavity and trap particles and droplets. In addition, two cylindrical bolted langevin transducers which were used by Kozuka et al. [36] managed to trap 2 to 3 mm polystyrene particles and mist as well. Furthermore, Khmelev et al. [37] designed a stepped disk ultrasonic transducer to effectively coagulate aerosol particles as small as 0.4 μm together.

* [redacted]

http://dx.doi.org/10.1016/j.snb.2015.10.068
0925-4005/

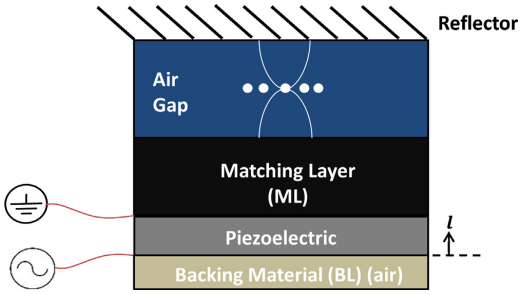

Fig. 1. Device assembly and terminal configuration (intended standing wave profile and particle collection location depicted in white).

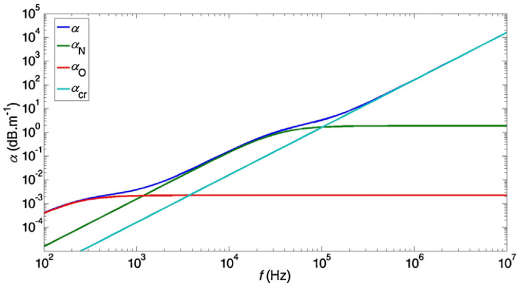

Fig. 2. Plot of absorption coefficient, α (dB/m) against frequency, f (Hz) for air.

Manipulation of particles as small as 500 μm in an acoustic resonator has been demonstrated [17]. However, most work with small particles has been performed in water within microfluidic resonators [20,38,39]. Here, we wish to individually manipulate very small, dense, solid particles in air, with diameters as small as 15 μm. Changing the dispersion medium to air at higher frequencies introduces losses due to attenuation [40], which are not a major factor in liquids. In addition, piezoelectric elements used for ultrasound generation are far less efficient in air, due to the large acoustic impedance mismatch between the two. This requires the use of a matching layer between the piezoelectric element and the air gap, which has to be optimised for use in a resonant air-filled cavity.

In this paper, both analytical and finite element (FE) models are used to examine the optimum criteria for an ultrasonic resonator that can be used for the manipulation of small particles in air, at frequencies of up to 2 MHz. Each layer within the design has to be chosen carefully in terms of thickness and material characteristics, for specific frequencies of operation. The modelling was then used to design and test a system which could be used with microparticle initially at rest on a surface with diameters as small as 15 μm experimentally.

2. Acoustic absorption in air

Models of acoustic resonators have been developed to predict the effects of acoustic impedance mismatch between the transducer and air, and subsequent attenuation in the air medium. FE modelling, using COMSOL Multiphysics™, has been used to predict the radiated pressure field within the air gap of the resonator within which the particles are held. This takes into account the frequency-dependent attenuation of ultrasound in air, allowing the selection of an optimum operating frequency for a particular application. Second, an analytical model has been developed to optimise the design of the transducer at the chosen frequency of operation, and considers the thickness and material properties of both the piezoelectric material and the impedance matching layer. Numerical evaluation of the analytical model has been conducted using MATLAB™. The system that has been modelled is shown in Fig. 1. The air-backed PZT (lead zirconate titanate) piezoelectric element generates ultrasound, which travels preferentially into the air-filled resonator due to the acoustic impedance matching layer (ML). The air gap itself, within which particle trapping should occur, forms a resonator by reflection from the glass slide reflector as shown in Fig. 1, the reflection of the inner side of this slide is assumed to be a perfect reflector.

As stated above, a major difference between using acoustofluidic systems in water and in air is that attenuation is much greater in air at frequencies in the low MHz range. Hence, the effect of attenuation as a function of frequency in air needs to be incorporated into the modelling. Two main absorption mechanisms are present–classical and relaxation effects [40]. Classical losses are due to the change of kinetic energy of molecules into heat, caused mainly by viscous and heat conduction losses (sometimes referred to as viscous dissipation losses), and collectively known as the Stokes–Kirchhoff loss. Relaxation losses are associated with a change of kinetic translational energy of the molecules into internal energy within the molecules themselves. Relaxation losses have two main forms, namely rotational absorption, which consists of relaxation losses due to rotationally excited molecules, and vibrational absorption due to excited molecules of oxygen and nitrogen [41].

Since, both the classical losses and rotational absorption are functions of temperature (T), pressure (P) and frequency (f), they can be combined and described via a single absorption coefficient α_{cr}. There are also absorption coefficients that can be predicted for vibrational effects in oxygen ($\alpha_{vib,O}$) and nitrogen ($\alpha_{vib,N}$) [40], leading to absorption coefficient curves for each mechanism, as shown in Fig. 2, which has been generated using the following equations (expressed in units of dB/m)

$$\alpha_{cr} = 15.895 \times 10^{-11} \frac{(T/T_0)^{1/2}}{(P/P_0)} f^2 \tag{1a}$$

$$\alpha_{vib,O} = 1.110 \times 10^{-1} \frac{e^{-2239.1/T}}{f_{r,O} + (f^2/f_{r,O})} \left(\frac{T_0}{T}\right)^{5/2} f^2 \tag{1b}$$

$$\alpha_{vib,N} = 9.480 \times 10^{-1} \frac{e^{-3352.0/T}}{f_{r,N} + (f^2/f_{r,N})} f^2 \tag{1c}$$

here T_0 and P_0 are reference values for temperature (293.15 K) and atmospheric pressure (101.325 kPa), respectively. The terms $f_{r,O}$ and $f_{r,N}$ are the frequencies of maximum absorption by oxygen and nitrogen, respectively, and are given by

$$f_{r,O} = \left(\frac{P}{P_0}\right) \left\{24 + 4.41 \times 10^4 h \left[\frac{12.(0.05+h)}{(0.391+h)}\right]\right\} \tag{2}$$

$$f_{r,N} = \left(\frac{P}{P_0}\right) (9 + 200h), \tag{3}$$

where h is the molar concentration of water vapour. A value of $h = 1.038$ was used here, which corresponds to a relative humidity of approximately 45% at 20 °C (conditions of the experimental setup and consistent with 293.15 K). The total acoustic absorption coefficient, α can then be found from

$$\alpha = \alpha_{cr} + \alpha_{vib,O} + \alpha_{vib,N} \tag{4}$$

The resulting predictions are shown in Fig. 2 for the frequencies of interest. In particular, it can be seen that α increases by more than an order of magnitude between the frequencies of

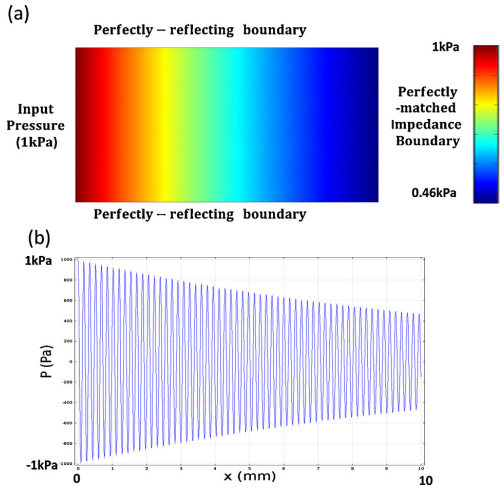

Fig. 3. (a) FE (COMSOL) model depicting boundary conditions and pressure amplitude variations that result, and (b) total acoustic pressure decay over the air path considered (10 mm at 2 MHz; Q_{air} = 482). However, these simulations have been conducted over the full frequency range being considered to yield Q_{air} values as a function of frequency."

100 kHz and 1 MHz (becoming increasingly dominated by classical and rotational losses) emphasizing the need to take attenuation into account in the model.

While such an attenuation coefficient is useful for analytical work, it is not so simple to apply to the FE models that formed part of the present work. To this end, Gröschl [42] described a quality factor approach for describing energy loss within a liquid medium, by deriving a complex expression for the acoustic velocity in the presence of damping (c_{damped}). The same approach can be used to account for attenuation in air. This involved a quality factor (Q_{air}) that modified the standard value for the speed of sound for air (c = 343 m/s at 20 °C), as follows:

$$c_{damped} = c \times \left(1 + i\frac{1}{Q_{air}}\right) \tag{5}$$

To show how this approach could be implemented, an FE model was created for a 10 mm long air-filled rectangular chamber of 5 mm width, with perfectly-reflecting side walls. A constant sinusoidal input pressure of 1 kPa was input at one end of chamber, and absorbed at the other end using a matched impedance layer (see Fig. 3(a)). Suitable values for α could be estimated from Eq. (4) for a particular frequency f within the range of interest (800 kHz–2 MHz) of this study. The FE model was then run with an excitation at a given f, for different values of Q_{air}, until a value was found that corresponded to the level of attenuation that would have been predicted by Eq. (4). An example of the FE output showing acoustic pressure decay at f = 2 MHz is shown in Fig. 3(b) which resulted in a corresponding quality factor, Q_{air} of 482. These frequency-dependent values of Q_{air} have subsequently been used in the main finite element model which investigates the effect of attenuation on the choice of operating frequency.

3. Modelling of air-filled resonators

3.1. Details of the models

The modelling studies were designed to serve two purposes. The first aim was to be able to model the effect of acoustic propagation within an air-filled chamber, and to predict forces on particles at particular frequencies. This optimisation of the operational frequency, taking into account the role of attenuation, used a finite element (FE) model. The second approach was to use analytical modelling to optimise the design of the layered resonator, in terms of its main elements—the chamber, the piezoelectric element, and the acoustic matching layer needed for efficient operation in air. Taken together, they allowed the whole system to be designed for effective manipulation of small particles.

The FE model considered a half wavelength $\left(\lambda_{air}/2\right)$ air gap (meaning the air-gap thickness was matched to the frequency of operation) within a chamber with parallel opposing surfaces (see Fig. 4(a); bounded by the displacement surface at the bottom and the reflective surface on the top). The aim was to find the conditions for optimal capture and positioning of small particles. When absorption is present, attenuation will increase with frequency, hence, our investigation focussed on determining the optimum frequency of operation to trap a given particle in air with a fixed excitation energy.

A complete three-dimensional model could not be developed due to high memory requirements and processing power restrictions. However, an axisymmetric model, with the full air chamber formed by rotation about the central axis (as shown on the left hand side of Fig. 4(a)), was used to provide a modelling comparison to the experimental results from a similarly-sized chamber, to be described in the next section. Note that the chamber side was assumed to have the same acoustic impedance as air, thus effectively modelling a non-reflecting boundary; this simulated a chamber with no sides. The input kinetic energy density into the system was held constant across the range of frequencies examined, by determining the required acceleration, $a_{boundary}$, for different angular frequencies (ω). The term kinetic input energy density is used to denote the energy transferred across from the surface of the matching layer into the air gap per unit length or area depending on if it is a 2D or 3D scenario, respectively. In both cases, this was done in order to keep the energy input into the FEA model of the air gap constant, allowing a comparison across the range of frequencies considered, such that an optimum operational frequency could be obtained. This was achieved by altering the displacement ζ of the input surface using

$$a_{boundary} = \omega^2 \times \zeta \tag{6}$$

$$\zeta \propto \frac{\sqrt{KE}}{f} \tag{7}$$

here KE, the kinetic energy, is kept constant. A value of ζ = 1 nm was assumed for f = 1 MHz, and the displacement scaled accordingly for the other frequencies considered. This displacement and the appropriate quality factors for air, Q_{air}, were then implemented in the FE model of the air chamber to obtain the resultant maximum 2nd order time-averaged absolute pressure within the air gap. Based on these pressures, the resultant ARF, F on a compressible sphere was calculated, based on Yosioka's formula [43,44]. This can be stated as

$$\left\langle F \right\rangle = \rho_f \pi \Phi^2 (k_F r_S)^3 F_Y \sin(2k_F x_S) \tag{8}$$

with the density compressibility factor F_Y given by

$$F_Y = \frac{\lambda + \left(2/3\,(\lambda - 1)\right)}{1 + 2\lambda} - \frac{1}{3\lambda\sigma^2} \tag{9}$$

here $\lambda = \rho_S/\rho_F$ and $\sigma = c_S/c_F$, in which ρ_S, ρ_F, c_S and c_F are the density and speed of sound of the solid and fluid, respectively. The wave number k_F is given by $k_F = 2\pi f/c_F$, r_S is the radius of the particle, and x_S is the position of the sphere. The velocity potential amplitude

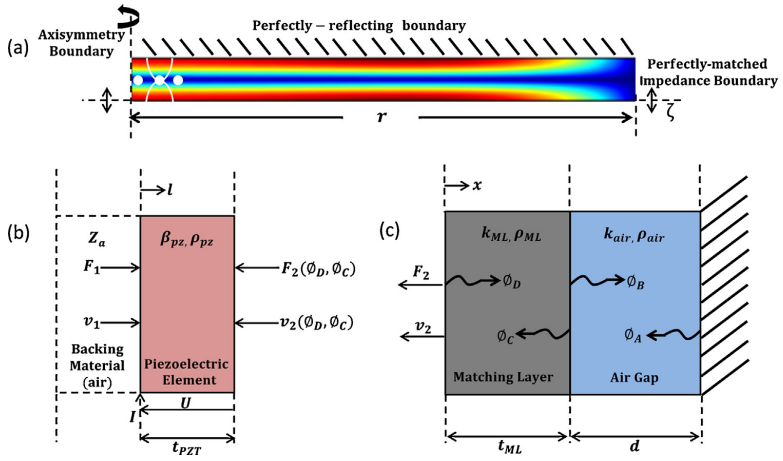

Fig. 4. (a) An axisymmetric FE model depicting boundary conditions and 2nd order time averaged absolute pressure distribution (The matched impedance boundary condition was imposed manually and not with the built in COMSOL PML). The half-wavelength standing wave profile and particle collection position are depicted in white. (b) Force and velocity direction along with the positive *l* direction used in the piezoelectric numerical analysis. (c) Boundary conditions implemented in the matching layer–air gap system. (The wave propagation direction in subset (b) and (c) of this figure has been rotated clockwise by 90° to ease the description and mathematical notation).

in a harmonic system, Φ is given in terms of the density, ρ, the pressure, P and the angular frequency ω by

$$\Phi = \frac{P}{i\omega\rho} \tag{10}$$

Evaluation of the forces via Eq. (8) allowed the FE model to be used for optimising the value of *f* for particle manipulation in air.

The next step was to use analytical modelling to determine the optimum design parameters for the construction of an air-filled chamber for a given value of *f*. The parameters to be investigated were the thickness of the main components within the resonator (the PZT piezoelectric element, the matching layer and the air gap) and the optimum material properties of the matching layer. The latter was needed due to the large acoustic impedance differences between different components in an air-based system, a far more significant issue than for operation in liquid. A one-dimensional numerical analysis was carried out using fundamental equations to represent the chamber. This approach was similar to that used by Haake [44], although no assumptions were made concerning the phase of the output wave from the piezoelectric substrate. The effect of using a matching layer and air gap on the system as a whole was considered, the coupling between the matching layer and air gap being of especial interest due to the large acoustic impedance mismatch. It is worth noting that a layered resonator design for operation in liquid systems has been developed [20,38,39] previously and our results are compared within this study.

The model assumed an acoustic source in the form of a piezoelectric element, attached to which was an impedance matching layer in contact with the air. A standing wave is then established by transmission across the impedance boundary between the matching layer and air, with perfect reflection from the boundary at the far end of the air cavity, this set up is depicted in Fig. 4(b) and (c). In contrast to Hill [20], who modelled a resonator for liquid use, this model includes the piezoelectric element and the matching layer, in order to investigate the role of material selection in energy transfer across the high acoustic contrast boundary between the matching layer material and air. It should be noted that Hill [39] previously, did include the piezoelectric element using an equivalent-circuit transducer model and matching layer in his models but did not investigate the effects of varying the matching layer properties (i.e. specific acoustic impedance), in contrast to what was carried out in this study.

The analytical model started by considering the conversion of the electrical input to an acoustic output from the piezoelectric layer. Nowotny et al. [45] analysed a general one dimensional propagation through a two-electrode arbitrarily oriented layered piezoelectric substrate. As the propagation direction is dictated by the orientation of our system, we use the simpler approach outlined in [46]. This involves forces: F_1 and F_2 and particle velocities: v_1 and v_2 as shown in Fig. 4(b), voltage potential (U), current (I), piezoelectric element thickness (l) and angular frequency (ω). The relevant expression is

$$\begin{bmatrix} F_1 \\ F_2 \\ U \end{bmatrix} = -i \begin{bmatrix} Z_{pz}\cot(\beta_{pz}l) & Z_{pz}\csc(\beta_{pz}l) & \frac{h}{\omega} \\ Z_{pz}\csc(\beta_{pz}l) & Z_{pz}\cot(\beta_{pz}l) & \frac{h}{\omega} \\ \frac{h}{\omega} & \frac{h}{\omega} & \frac{h}{\omega}C_0 \end{bmatrix} \begin{bmatrix} v_1 \\ v_2 \\ I \end{bmatrix}. \tag{11}$$

here Z_{pz} is the acoustic impedance of the piezoelectric element, given by $Z_{pz} = A\sqrt{\rho_{pz}E^D}$, where ρ_{pz} is the density of the PZT transducer, and E^D is the stiffened elastic constant (the "stiffening" occurring due to piezoelectric effects [46]) defined by $E^D = E^E + \left(e^2/\varepsilon^s\right)$, e being the piezoelectric constant, E^E the elastic constant and ε^s the permittivity at constant strain in the piezoelectric material. The wavenumber β_{pz} in the piezoelectric is $\beta_{pz} = \omega/c_L^D$, where c_L^D is the stiffened longitudinal velocity defined by $c_L^D = \sqrt{E^D/\rho_{pz}}$, and $h = e/\varepsilon^s$. C_0 is the clamped (zero strain) capacitance of the piezoelectric element, the measured capacitance at a frequency well above any pronounced resonance.

Boundary conditions were implemented to link the piezoelectric layer shown in Fig. 4(b) with the matching layer and air gap as shown in Fig. 4(c) (the axes *l* and *x*, respectively, are aligned). These boundary conditions are applied to a general velocity potential equation representing waves propagating in each of the media considered. In general, the velocity potential equation is defined as $\emptyset_n = \Phi_n e^{i(\omega t \pm kx + \vartheta_n)}$ and the subscript, n can be replaced by *A*, *B*, *C* or *D* as defined in Fig. 4(c). Where, $\emptyset_n$ is the velocity potential, Φ_n is the

velocity potential amplitude (see Eq. (10)) at some position x. ϑ_n is the phase of the wave at $x = 0$, and the sign of the wavenumber k in the medium denotes the direction of propagation. From this definition of the velocity potential functions, the particle velocity v_n and pressure P_n can be derived and implemented as boundary conditions using, respectively, where, $v_n = -\nabla\emptyset_n$ and $P_n = \rho\left(\partial\emptyset_n/\partial t\right)$.

For example, we arrive with an expression for the velocity and pressure in the air gap, v_{air} and P_{air}.

$$v_{air} = ik_{air}e^{i\omega t}\left(\Phi_B e^{i(-k_{air}x+\vartheta_B)} - \Phi_A e^{i(k_{air}x+\vartheta_A)}\right) \tag{12}$$

$$P_{air} = i\omega\rho_{air}e^{i\omega t}\left(\Phi_B e^{i(-k_{air}x+\vartheta_B)} + \Phi_A e^{i(k_{air}x+\vartheta_A)}\right) \tag{13}$$

By imposing multiples of half-wavelength air gap and a hard ($v_{air} = 0$ m/s) boundary condition at the right end of the air gap as shown in Fig. 4(c), a relationship between $\emptyset_A$ and $\emptyset_B$ can be found using Eq. (12) using simultaneous equations comparing the real and imaginary components:

$$\Phi_B = \Phi_A \tag{14}$$

and

$$\vartheta_B = \vartheta_A + 2\left(k_{air}\right)\left(\frac{n\lambda}{2}\right) \tag{15}$$

here the wavenumber has the subscript air to indicate it is in relation to the wave in the air layer. Consequently, a relationship between $\emptyset_D$ and $\emptyset_C$ can be obtained by implementing pressure and velocity equilibrium boundary conditions at the matching layer–air gap interface.

By equating pressure and velocity at the matching layer–air gap ($x = 0$) interface using equations for velocity v_n and pressure P_n, we obtain

$$i\omega\rho_{ML}e^{i\omega t}\left(\Phi_D e^{i(\vartheta_D)} + \Phi_C e^{i(\vartheta_C)}\right) = i\omega\rho_{air}e^{i\omega t}\left(\Phi_A e^{i\left(2k_{air}(n\lambda/2)+\vartheta_A\right)} + \Phi_A e^{i(\vartheta_A)}\right) \tag{16}$$

and,

$$ik_{ML}e^{i\omega t}\left(\Phi_D e^{i(\vartheta_D)} - \Phi_C e^{i(\vartheta_C)}\right) = ik_{air}e^{i\omega t}\left(\Phi_A e^{i\left(2k_{air}(n\lambda/2)+\vartheta_A\right)} - \Phi_A e^{i(\vartheta_A)}\right) \tag{17}$$

where Eqs. (12)–(15) have been used to eliminate terms Φ_B and ϑ_B.

We can solve these two simultaneous equations to obtain an expression for $\emptyset_C$ in terms of $\emptyset_D$ noting that $\emptyset_C$ at $x = 0$ is given by $\Phi_C e^{i(\vartheta_C)}$ (likewise $\emptyset_D = \Phi_D e^{i(\vartheta_D)}$). We define an acoustic reflection term R that occurs at the interface between the matching layer and the air gap such that $\emptyset_C = R \times \emptyset_D$. The R can be written as:

$$R = \left[\frac{D-1}{D+1}\right] \tag{18}$$

where,

$$D = \left(\frac{\rho_{air}k_{ML}}{\rho_{ML}k_{air}}\right) \times \left[\frac{e^{i(2k_{air}d)}+1}{e^{i(2k_{air}d)}-1}\right] \tag{19}$$

here ρ_{air} and ρ_{ML} are the densities and k_{air} and k_{ML} are the wave numbers of the air and matching layers respectively, and d is the thickness of the air gap. Information obtained from this analysis allows for a relationship between $\emptyset_C$ and $\emptyset_D$ which simplifies the subsequent analysis steps described below.

We now have one equation ($\emptyset_C = R \times \emptyset_D$) with two unknowns ($\emptyset_C$, $\emptyset_D$). In order to be able to evaluate these unknowns and ultimately find the pressure profile in the air gap, we utilise the conversion matrix (Eq. (11)) for the piezoelectric element, as this yields a second equation relating $\emptyset_D$ and $\emptyset_C$, thus providing a solution for $\emptyset_D$ in terms of the voltage input, U. Using equations depicting $\emptyset_n$, v_n and P_n and the boundary conditions of $F_1 = Z_{BL}v_1$, $F_2 = -A\omega\rho_{ML}\left[\emptyset_D + \emptyset_C\right]$ and $v_2 = -ik_{ML}e^{i\omega t}\left[\emptyset_D - \emptyset_C\right]$, yields:

$$\emptyset_D = UX_T + \emptyset_C R_T \tag{20}$$

where

$$Y = \frac{-2h^2Z_{pz}}{\omega^2}\left[\frac{\cos\left(\beta_{pz}l\right)-1}{\sin\left(\beta_{pz}l\right)}\right] - \frac{iZ_{pz}\cot\left(\beta_{pz}l\right)}{\omega C_0}\left[Z_{ML}+Z_{aBL}\right] - \frac{\left[Z_{ML}Z_{BL}+{Z_{pz}}^2\right]}{\omega C_0} + \frac{ih^2}{\omega^2}\left[Z_{ML}+Z_{BL}\right] \tag{21}$$

$$R_T = \frac{\left(\left(-2h^2Z_{pz}/\omega^2\right)\left[\left(\cos\left(\beta_{pz}l\right)-1\right)/\left(\sin\left(\beta_{pz}l\right)\right)\right] + \left(\left(iZ_{pz}\cot\left(\beta_{pz}l\right)\right)/\omega C_0\right)\left[Z_{ML}-Z_{BL}\right] + \left[\left(Z_{ML}Z_{BL}-{Z_{pz}}^2\right)\right]/\omega C_0 - \left(ih^2/\omega^2\right)\left[Z_{ML}-Z_{BL}\right]\right)}{Y} \tag{22}$$

$$X_T = \left(\frac{h}{\omega k_{ML}}\right)\frac{\left[\left(\left(Z_{pz}\left(\cos\left(\beta_{pz}l\right)-1\right)\right)/\sin\left(\beta_{pz}l\right)\right) - iZ_{BL}\right]}{Y} \tag{23}$$

and where Z_{ML} and Z_{BL} are the acoustics impedances of the matching layer and the backing layer (air) respectively. As $\emptyset_C = R \times \emptyset_D$, with R defined above, then combining Eqs. (20)–(23) produces an expression for $\emptyset_D$ in terms of the voltage input and piezoelectric properties as below:

$$\emptyset_D = \frac{UX_T}{(1 - RR_T)} \tag{24}$$

It is thus possible to determine the pressure in the air gap as a result of applied voltage potential, the material properties and layer dimensions. Eq. (24) gives an expression for $\emptyset_D$; using this and the relation $\emptyset_C = R \times \emptyset_D$, Eq. (19) or (20) will give $\emptyset_A$. This allows a description of the pressure field in the air gap, bearing in mind that P_{air} is given by Eq. (16) and that Φ_A, Φ_B, ϑ_A and ϑ_B have been related above in Eqs. (14) and (15).

3.2. Predictions of the models

The models were used to find an optimum design for a complete resonant chamber, which could then be evaluated experimentally. The variables under consideration for the layered resonator design included the material chosen for the matching layer, and individual layer thicknesses of the piezoelectric material, matching layer and air gap. A numerical simulation was carried out by varying the density, ρ_{ML} and speed of sound, c_{ML} of the matching layer (the product of which results in the specific acoustic impedance, Z_{ML}). The aim was to study the combined effects of optimising geometry and materials to maximise the pressure (in the air gap) which in turn gives us the force (which acts on the particles) and consider how the acoustic attenuation limits operation in air at higher frequencies.

In order to investigate the optimum operating frequency, two sets of data are presented from the FE model for a fixed input energy. The first uses a constant value for Q_{air} (taken as that at a frequency of 0.95 MHz ($Q_{air} = 1013$). This is to illustrate the expected rise in force with frequency. The second set studies the change in Q_{air} with frequency so as to investigate attenuation within the air layer. In this second data set, we expect to see a maximum force to occur at a particular frequency due to the trade-off between the increase in force with frequency (as shown in Eq. (8) where $\langle F \rangle$ scales with k_F) and the loss of energy with attenuation at higher frequencies. The results are shown in Fig. 5 for path lengths that represent odd multiples of $\lambda_{air}/2$, each being resonant within the air gap. For a constant energy input condition (scaled to 1 nm input displacement at 1 MHz using Eq. (7)), and a constant Q_{air}, it is observed in Fig. 5(a) that the resultant 2nd order time-averaged absolute pressure, P experiences a maximum in amplitude at ~1.5 MHz for the $\lambda_{air}/2$ case (Fig. 5(a)). The curves for $3\lambda_{air}/2$ and $5\lambda_{air}/2$ show a less pronounced maximum at the same value. For the dry

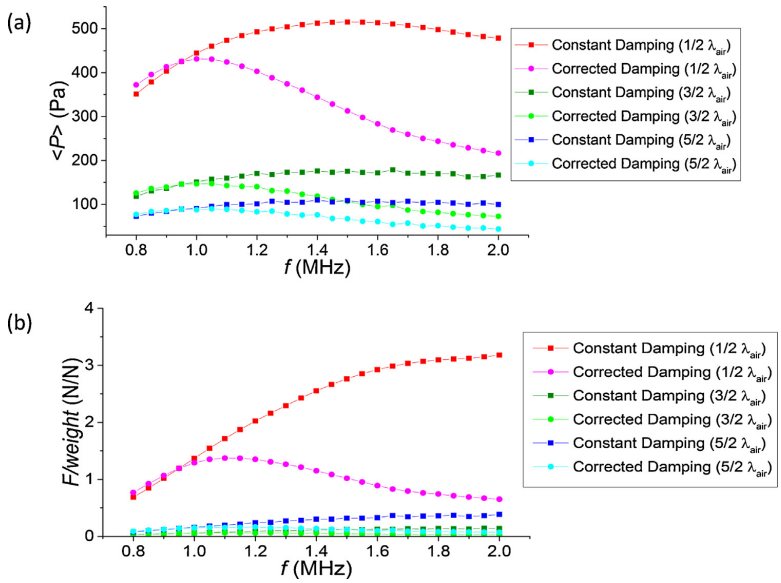

Fig. 5. Results of FE modelling for acoustic transmission through the resonator air gap in terms of (a) 2nd order time-averaged absolute pressure ⟨*P*⟩ and (b) force per unit weight (*F*/weight) as a function of frequency. The results are shown over odd multiples of $\lambda_{air}/2$. Two sets of data are presented in each plot for a 3.18 mm diameter chamber (see Fig. 4(a))—one for a constant value of $Q_{air} = 1013$ ("Constant Damping"), and a second with Q_{air} calculated for each frequency ("Corrected Damping").

PMMA particles used in the experiments, the radiation force per unit particle weight (*F*/weight) calculated using Eq. (8) increases with frequency for the entire range considered (Fig. 5(b)). *F*/weight demonstrates the ratio of radiation force exerted upon a particle relative to the particle's weight (capability of levitation) and its dependency on the frequency of operation.

Consider now the case where Q_{air} is adjusted as a function of frequency (i.e. the "corrected damping") case. Now it is observed (see Fig. 5) that the maximum values of ⟨*P*⟩ and *F*/weight occur at 1 MHz and 1.1 MHz, respectively, for the $\lambda_{air}/2$ resonance, with a significant decrease in amplitude at higher frequencies. Similar trends are seen for the $3\lambda_{air}/2$ and $5\lambda_{air}/2$ cases. This indicates the effect of frequency-dependant attenuation on the resonant characteristics of the chamber. It is worth noting that the relationship of both ⟨*P*⟩ and *F*/weight with frequency is dependent on the size of the chamber itself. The FE model assumes side walls through which energy can be dissipated. Thus, if the diameter of the chamber was to be increased for the same thickness of air gap, a shift in the maxima to lower frequencies would be observed. This is illustrated in Fig. 6. This is due to the fact that for smaller systems more energy is lost due to diffraction; thus, to compensate for this, a higher frequency is required to reduce diffractive effects. This trend is similar for the $3\lambda_{air}/2$ and $5\lambda_{air}/2$ cases. However, it should be noted that at larger air gap thicknesses, values of both ⟨*P*⟩ and *F*/weight decrease significantly as shown in Fig. 5(a) and (b). As was demonstrated in Fig. 5(b), the optimum frequency to operate a parallel acoustic trapping mode in air for $r = 3.18$ mm (equal perimeter to a 5×5 mm square chamber as used in experiments) is predicted to be 1.1 MHz.

The value of the best frequency of operation could now be used within the analytical model, the aim being to optimise the physical design of the resonant acoustic chamber design. This was achieved by determining the optimum layer thickness of each layer in the system. The model was constructed with three layers, as shown in Fig. 7(a): a piezoelectric layer (backed by air), a matching layer and an air gap (terminated by a rigid reflector). The air gap was chosen to be $0.5001\lambda_{air}$ (i.e. very close to $0.5\lambda_{air}$ but avoiding a numerical error in the Matlab™ code when calculating *D* as shown in Eq. (19) within the numerical analysis). The optimum thickness values of the other two layers, and their material parameters, could then be investigated, together with the role of damping. It should be noted that the resonator layers were all considered as one system (i.e. each layer was linked together) in the numerical analysis but is to be discussed in stages (i.e. layer by layer) to help the discussion of the findings. A three-stage approach was adopted. First, the material properties and damping factor of the piezoelectric layer was set to that given by the manufacturer, PZT, manufactured by Ferroperm Ltd [47]). The role of the thickness of the piezoelectric layer (t_{PZT}) was examined by finding the velocity potential amplitude (Φ_D) in an aluminium matching layer across a range of values. Fig. 7(a) shows the velocity potential for a range of thicknesses (normalised by piezoelectric wavelength, i.e. t_{PZT}/λ_{PZT}). A peak value occurs at $t_{PZT}/\lambda_{PZT} = 0.254$. Such data was collected for a range of matching layer acoustic impedances, and in each case the thickness at which a maximum velocity potential occurs (see circle in Fig. 7(a)) has been identified. The result is shown in Fig. 7(b) for the case in which the matching layer has a *Q* factor (Q_{ML}) of 400 which corresponds to that of typical solids. This Q_{ML} value was chosen as it is in line with other studies [39,41], however it is worth noting that this value becomes less significant in a more realistic scenario when energy losses within the piezoelectric element is considered as will be discussed later. In both cases it can be seen that there is no significant (3.6% variation) effect on the optimum piezoelectric thickness for a matching-layer impedance Z_{ML} above 15MRayls.

The second stage was to investigate the best matching layer thickness (t_{ML}) for the optimum thickness of piezoelectric material identified above, with the air gap remaining fixed at $0.5001\lambda_{air}$. The

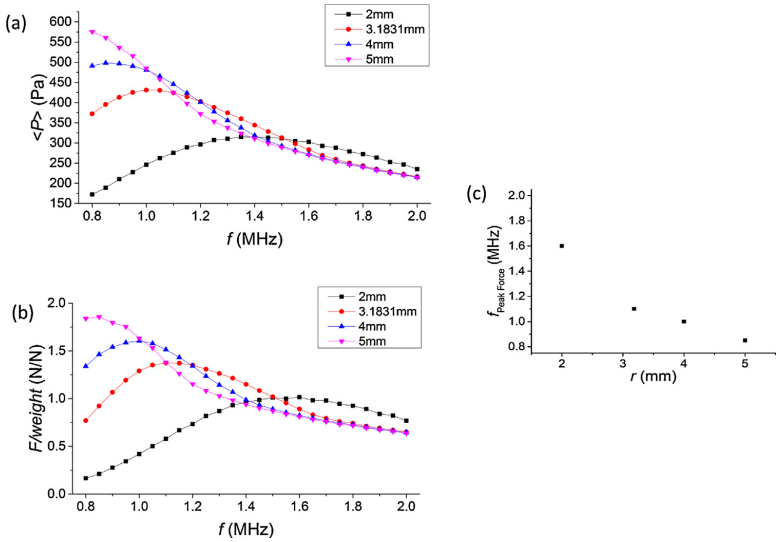

Fig. 6. Effect of chamber radius, r on (a) 2nd order time averaged absolute pressure, $\langle P \rangle$ vs frequency, f, (b) F/weight vs frequency, f, and (c) the frequency at which the peak force occurs.

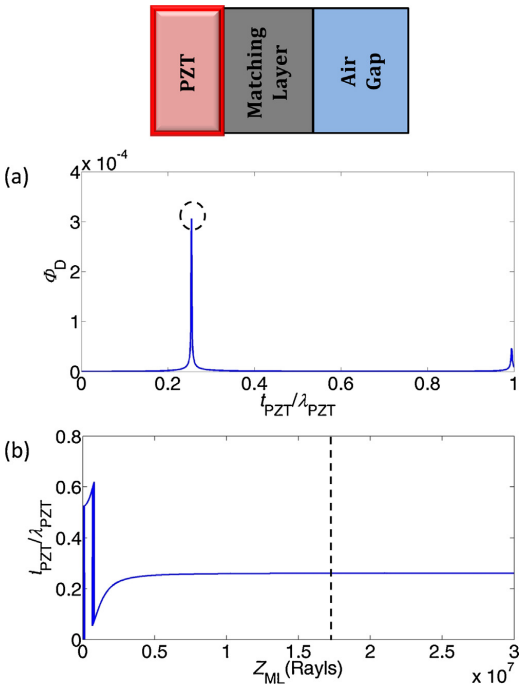

Fig. 7. Investigation of PZT parameters. (a) Arrangement of PZT element, matching layer and a fixed air gap of $\approx 0.5\lambda_{air}$. (b) Dependence of Φ_D on the normalised piezoelectric element thickness (t_{PZT}/λ_{PZT}). (c) Dependence of (t_{PZT}/λ_{PZT}) on the specific acoustic impedance, Z_{ML} (Rayls) of the matching layer, for $Q_{air} = 965$, $Q_{PZT} = 1000$ and $Q_{ML} = 400$. The dotted line depicts the specific acoustic impedance of aluminium ($Z_{ML} = 17.28$ MRayls).

value of t_{ML} would be expected to depend on Z_{ML} (and hence λ_{ML}). The dependence of the 2nd order time-averaged absolute pressure, $\langle P \rangle$ in the aluminium matching layer on t_{ML}/λ_{ML} is shown in Fig. 8(a). This allowed the best normalised thickness (t_{ML}/λ_{ML}) to be determined as a function of impedance Z_{ML}, and the results are shown in Fig. 8(b). This is for fixed values of $Q_{air} = 965$, $Q_{PZT} = 1000$ (based on supplier's (Ferroperm) minimal value) and $Q_{ML} = 400$. It is interesting to note that the optimum thickness only differs from a steady value of $t_{ML}/\lambda_{ML} \approx 0.5$ at impedance values which are below 10 MRayls. This then predicts that in a chamber such as that assumed in this work, there is very little sensitivity to the optimum value of t_{ML}/λ_{ML}, and that for the situation where $z_{ML} \gg z_{air}$, the matching-layer to air interface acts as a pressure-release boundary. This is consistent with acoustic wave reflection theory [48] where a reflection coefficient, R of -1 or mathematically represented as a phase shift of π radians with a magnitude of 1 would be expected on reflection at the matching layer–air interface. Based on this observation, a value of $t_{ML} \approx n\lambda_{ML}/2$ should hold for any solid material, making the design of the matching layer very simple. Note that this finding differs from the requirement in a travelling wave airborne transducer system (due to the presence of the reflected wave in our system altering the boundary condition), as used for applications such as non-destructive testing, where a $\lambda_{ML}/4$ matching layer thickness is used.

The third stage (Fig. 9) investigated the signal in the air gap and its dependency on material properties, specifically the acoustic impedance, Z_{ML}. The maximum pressure in the air gap is shown for a range of impedances of the matching layer (Z_{ML}) in Fig. 9(a), for fixed values of PZT thickness ($t_{PZT} = 0.254\lambda_{PZT}$), air gap ($t_{air} \approx 0.5\lambda_{air}$) and the matching layer thickness ($t_{ML} \approx 0.5\lambda_{ML}$). It can be seen that there are multiple peaks in amplitude, and that these are more closely-spaced at lower values of Z_{ML}. However, when damping is added to the matching layer and piezoelectric layer, these oscillations are less pronounced, as would be expected (Fig. 9(b)). Here, Q_{ML} was fixed at 400 (typical for aluminium) and Q_{PZT} varied. Similarly, when Q_{PZT} was set to 1000 whilst Q_{ML} was varied, Fig. 9(c), the oscillations were again much less pronounced.

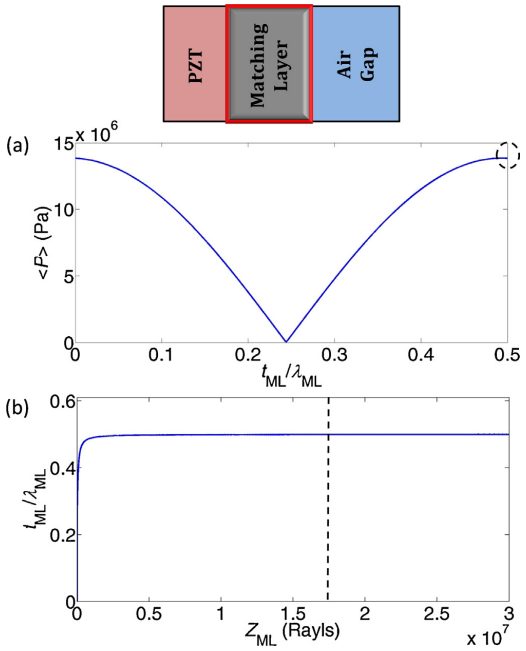

Fig. 8. Effect of variations in thickness of the matching layer (t_{ML}) for a constant PZT thickness ($0.254\lambda_{PZT}$) and air gap ($\approx 0.5\lambda_{air}$). (a) Dependence of $\langle P \rangle$ in the matching layer medium (aluminium) on the matching layer thickness (normalised by λ_{ML}). (b) Matching layer thickness (normalised by λ_{ML}) dependence on specific acoustic impedance, Z_{ML} (Rayls), for values of $Q_{air} = 965$, $Q_{PZT} = 1000$ and $Q_{ML} = 400$. The dotted line depicts the specific acoustic impedance of aluminium ($Z_{ML} = 17.28$ MRayls).

It is also worth noting that the Q_{ML} values used play a minimal role at realistic acoustic impedances as there is not much variation in the resultant pressure for the range of Q_{ML} values considered.

It can be concluded from the above analysis that the choice of matching layer material is not nearly as significant as the thickness. These numerical findings are consistent with the experimental observations by Hill [20] who used three different matching layer materials (i.e. brass, aluminium and macor) where minimal variations in the transmitted acoustic energy was observed when constructing a layered resonator in a liquid based resonator. In the above, it has been demonstrated theoretically that an air-filled cavity behaves in a similar fashion. These predictions can be used to design effective experimental resonators for particle manipulation in air, as will now be described.

4. Experimental fabrication and testing

To validate and demonstrate the findings of the models, an acoustic resonator was fabricated to show that micron-sized particles could be positioned and held stationary experimentally within an air-filled chamber. The design was shown schematically in Fig. 1(a). The actual chamber consisted of a 5 mm square, 0.5 mm thick PZT element (Ferroperm PZ-26; with diminishingly thin electrodes on either side of the piezoelectric element) adhered to a 3 mm thick aluminium matching layer using a thin layer of epoxy resin (measured to be <50 μm collectively with the electrodes of the PZ-26 piezo-ceramic used). The model establishes the optimum dimensions of each layer in terms of wavelength and the operational frequency; hence each idealised dimension is dictated. However, in reality it is not possible to meet all these requirements exactly. Specifically, the piezoelectric element was limited by those dimensions which were readily available; a 500 μm thick Pz26 piezoelectric disk was used. As such, the resonant frequency of the piezoelectric and matching layer component combination was measured using a Laser Doppler Vibrometer, and this was matched to that required and to the air gap thickness." It is worth noting that the epoxy resin is not considered in the numerical analysis. As a result an additional loss of energy transmitted into the matching layer may be experienced; consequently leading to a reduced 2nd order time-averaged pressure absolute pressure within the air gap should be experienced. However, as a very thin uniform layer of adhesive material is used, a relatively small effect should be expected as shown in the modelling study carried out by Hill et al. [39]. The transducer was excited by an alternating voltage at the bottom surface of the piezoelectric transducer and electrically grounded on the top surface (i.e. at the PZT/aluminium interface). Electrical connections were made using insulated copper wires and silver conductive paint. Acoustic resonances within the air cavity were achieved using a glass reflector, attached rigidly to the moving stage of a micro-positioner, so as to allow precise control over the air gap. This allowed the optimum conditions predicted by the modelling to be achieved. The PZT transducer was driven at the chosen frequency using a Stanford Research Systems Model No.DS345 waveform generator and an Amplifier Research Model No.25A250A power amplifier. This was used to trap dry PMMA particles (with properties $\rho_s = 1190$ kg/m^3 and $c_s = 2350$ m/s; Bangs Laboratories Inc.) at specified locations within the air cavity. Imaging was carried out using an optical microscope (Infinity Photo-optical Company) fitted with a Hitachi KPD20AU CCD camera.

The existing literature [17,28–30] is concerned with significantly larger objects compared to those chosen for this study. Experiments have confirmed that the design needed for the efficient manipulation of micro-particles in air can be achieved using acoustic resonators, provided the conditions outlined in the modelling above are met. To this end an acoustic resonator has been fabricated to operate at 1.1 MHz. The transducer was excited at a 2 V_{pp} waveform from the signal generator at 1.0025 MHz (i.e. resonant frequency of the transducer) with a $3/2\lambda_{air}$ (≈ 500 μm) gap size. Note that this was used to aid particle visualisation (instead of $1/2\lambda_{air}$). Therefore to achieve sufficient force to levitate a PMMA particle, the input excitation amplitude/displacement, ζ_i should be scaled accordingly (F/weight $\propto \left(\zeta_i/\zeta_{@1nm}\right)^2$). The PMMA microspheres (Bangs Laboratories Inc.; $\rho_{particle} = 1190$ kg/m^3) of sizes 83 μm and 15 μm, respectively, were introduced at the bottom surface of the air gap (i.e. on top of the matching layer). As shown in Fig. 10(a) and (b), dry particles were successfully trapped in air. As shown in Fig. 10(a), the 83 μm particles were individually trapped just below the pressure nodes. The distance at which the particle sits below the pressure node can be used to estimate the acoustic radiation force maximum by performing a force balance with the weight of the particle, this yields a value of the order 10^{-8} N. A range of particles including dry expanded hollow polystyrene microspheres (Expancel Microspheres 461 DET 40 d25; 35–55 μm and 25 kg/m^3) were also used. The system was able to trap the above mentioned Expancel microspheres at resonator air gap distances of up to $9/2\lambda_{air}$. It was thus demonstrated that the use of the models led to the design of an efficient resonator for individualised particle collection in air, which, for the first time, was able to operate at the small particle sizes used. It should be noted that this is not necessarily the lower limit of particle size but the lower limit we were able to demonstrate. Since, the system used here is an open ended system, wind draft from outside the

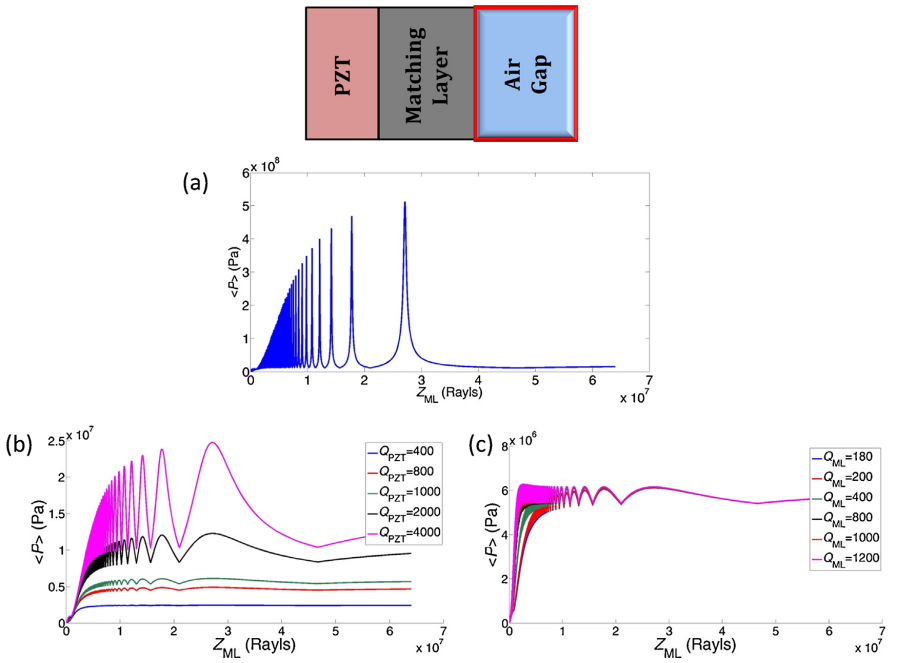

Fig. 9. Variation of $\langle P \rangle$ with specific acoustic impedance of the matching layer (Z_{ML}). (a) Result for fixed values of PZT thickness ($t_{PZ} = 0.254\lambda_{PZT}$), air gap ($t_{air}/d \approx 0.5\lambda_{air}$) and the matching layer thickness ($t_{ML} \approx 0.5\lambda_{ML}$), with $Q_{air} = 965$. (b) Conditions as in (a) but with $Q_{ML} = 400$ and Q_{PZT} varied. (c) Conditions as in (a), but with $Q_{PZT} = 1000$ and Q_{ML} varied.

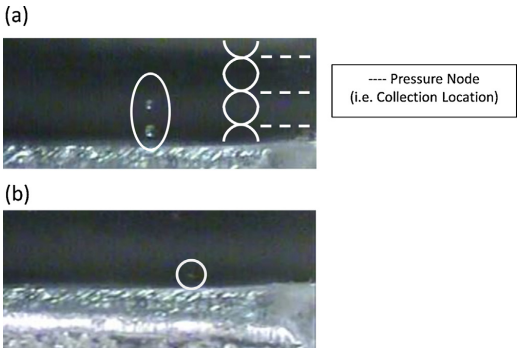

Fig. 10. Optical photographs showing levitation of dry PMMA particles of various diameters in an air-filled cavity of $3/2\lambda_{air}$ thickness. (a) 83 μm diameter particles (circled) that were trapped at the pressure nodes of the resonant cavity, as shown to the right of the image. (b) Entrapment of a very small 15 μm diameter PMMA particle.

system is a lot more significant and inhibits localised particle collection. It is worth noting that effects of acoustic streaming were not evident in experiments (even when mist was used to help visualise the field) and hence its effects were not considered in this study. As the particle must be elevated from a substrate, stiction based adhesion forces act as a key limiting factor on minimum particle size. These forces scale with the particle radius, r [49], as well as the relative humidity of the system [50]. This contrasts with the size scaling of the ARF (r^3). Hence, when the particle sizes decrease, the ARF decreases more significantly than the stiction based adhesion forces, and as such the later begins to dominate.

5. Conclusions

An acoustic modelling approach has been used to help identify design parameters of an optimised robust design of an acoustic resonator in air. A method to obtain an optimum frequency of operation was demonstrated and found to be dependent on the size of the system. However, an optimum operational frequency of 1.1 MHz was determined using finite element analysis when frequency dependent attenuation factors were considered for the system studied. In addition, the thickness of the piezoelectric element considered (Ferroperm Pz26) should be $\approx 0.254\lambda_{PZT}$, together with a matching layer thickness of $\approx 0.5\lambda_{ML}$ for relatively high acoustic impedance properties. When suitable quality factors are considered, the selection of matching layer material becomes less important as the resultant pressure field amplitudes do not vary significantly with material selection. However, individual layer thicknesses play a significant role. The knowledge from the theoretical analysis was used to design an experimental resonator which successfully levitated and trapped solid particles of micron-sizes (83 μm and 15 μm). Particle levitation and trapping at this size scale has not been reported in the literature to date which demonstrates the success of using modelling to elucidate the correct experimental conditions.

Acknowledgements

This work was performed in part at the Melbourne Centre for Nanofabrication (MCN) in the Victorian Node of the Australian

National Fabrication Facility (ANFF). The authors are grateful for funding provided by the Australian Research Council (Discovery Project DP110104010).

References

[1] F. Beyeler, A. Neild, S. Oberti, D.J. Bell, Y. Sun, J. Dual, B.J. Nelson, Monolithically fabricated microgripper with integrated force sensor for manipulating microobjects and biological cells aligned in an ultrasonic field, J. Microelectromech. Syst. 16 (2007) 7–15.
[2] Y.-W. Lu, C.-J.C. Kim, Microhand for biological applications, Appl. Phys. Lett. 89 (2006) 164101.
[3] K. Van Vliet, G. Bao, S. Suresh, The biomechanics toolbox: experimental approaches for living cells and biomolecules, Acta Mater. 51 (2003) 5881–5905.
[4] C.-J. Kim, A.P. Pisano, R.S. Muller, M.G. Lim, Polysilicon microgripper, Sens. Actuators, A: Phys. 33 (1992) 221–227.
[5] R. Salim, H. Wurmus, A. Harnisch, D. Hülsenberg, Microgrippers created in microstructurable glass, Microsyst. Technol. 4 (1997) 32–34.
[6] T.C. Duc, G.-K. Lau, J.F. Creemer, P.M. Sarro, Electrothermal microgripper with large jaw displacement and integrated force sensors, J. Microelectromech. Syst. 17 (2008) 1546–1555.
[7] S. Saito, H. Himeno, K. Takahashi, Electrostatic detachment of an adhering particle from a micromanipulated probe, J. Appl. Phys. 93 (2003) 2219–2224.
[8] E. van West, A. Yamamoto, T. Higuchi, The concept of "Haptic Tweezer", a non-contact object handling system using levitation techniques and haptics, Mechatronics 17 (2007) 345–356.
[9] R.S. Fearing, Survey of sticking effects for micro parts handling, in: Intelligent Robots and Systems 95. 'Human Robot Interaction and Cooperative Robots', Proceedings. 1995 IEEE/RSJ International Conference on, IEEE, 1995, pp. 212–217.
[10] R. Maboudian, W.R. Ashurst, C. Carraro, Tribological challenges in micromechanical systems, Tribol. Lett. 12 (2002) 95–100.
[11] F. Arai, D. Andou, Y. Nonoda, T. Fukuda, H. Iwata, K. Itoigawa, Integrated microendeffector for micromanipulation, IEEE/ASME Trans. Mechatron. 3 (1998) 17–23.
[12] N. Manaresi, A. Romani, G. Medoro, L. Altomare, A. Leonardi, M. Tartagni, R. Guerrieri, A CMOS chip for individual cell manipulation and detection, IEEE J. Solid-State Circuits 38 (2003) 2297–2305.
[13] H. Shafiee, M.B. Sano, E.A. Henslee, J.L. Caldwell, R.V. Davalos, Selective isolation of live/dead cells using contactless dielectrophoresis (cDEP), Lab Chip 10 (2010) 438–445.
[14] F. Petersson, A. Nilsson, C. Holm, H. Jönsson, T. Laurell, Continuous separation of lipid particles from erythrocytes by means of laminar flow and acoustic standing wave forces, Lab Chip 5 (2005) 20–22.
[15] T. Franke, S. Braunmuller, L. Schmid, A. Wixforth, D.A. Weitz, Surface acoustic wave actuated cell sorting (SAWACS), Lab Chip 10 (2010) 789–794.
[16] W. Xie, C. Cao, Y. Lü, B. Wei, Levitation of iridium and liquid mercury by ultrasound, Phys. Rev. Lett. 89 (2002) 104304.
[17] D. Foresti, M. Nabavi, M. Klingauf, A. Ferrari, D. Poulikakos, Acoustophoretic contactless transport and handling of matter in air, Proc. Natl. Acad. Sci. U.S.A. 110 (2013) 12549–12554.
[18] L.P. Gor'kov, On the forces acting on a small particle in an acoustical field in an ideal fluid, Sov. Phys. Dokl. 6 (1962) 773.
[19] J. Hultström, O. Manneberg, K. Dopf, H.M. Hertz, H. Brismar, M. Wiklund, Proliferation and viability of adherent cells manipulated by standing-wave ultrasound in a microfluidic chip, Ultrasound Med. Biol. 33 (2007) 145–151.
[20] M. Hill, R.J. Townsend, N.R. Harris, Modelling for the robust design of layered resonators for ultrasonic particle manipulation, Ultrasonics 48 (2008) 521–528.
[21] P. Glynne-Jones, C.E.M. Demore, Y. Congwei, Q. Yongqiang, S. Cochran, M. Hill, Array-controlled ultrasonic manipulation of particles in planar acoustic resonator, IEEE Trans. Ultrason. Ferroelectr. Freq. Control 59 (2012) 1258–1266.
[22] A. Neild, S. Oberti, F. Beyeler, J. Dual, B.J. Nelson, A micro-particle positioning technique combining an ultrasonic manipulator and a microgripper, J. Micromech. Microeng. 16 (2006) 1562.
[23] A.L. Bernassau, C.R.P. Courtney, J. Beeley, B.W. Drinkwater, D.R.S. Cumming, Interactive manipulation of microparticles in an octagonal sonotweezer, Appl. Phys. Lett. 102 (2013) 4101.
[24] C. Devendran, I. Gralinski, A. Neild, Separation of particles using acoustic streaming and radiation forces in an open microfluidic channel, Microfluid. Nanofluid. 17 (2014) 879–890.
[25] A. Lenshof, T. Laurell, Continuous separation of cells and particles in microfluidic systems, Chem. Soc. Rev. 39 (2010) 1203–1217.
[26] D.J. Collins, T. Alan, K. Helmerson, A. Neild, Surface acoustic waves for on-demand production of picoliter droplets and particle encapsulation, Lab Chip 13 (2013) 3225–3231.
[27] M. Sesen, T. Alan, A. Neild, Microfluidic on-demand droplet merging using surface acoustic waves, Lab Chip 14 (2014) 3325–3333.
[28] W. Xie, B. Wei, Dependence of acoustic levitation capabilities on geometric parameters, Phys. Rev. E 66 (2002) 026605.
[29] D. Foresti, N. Bjelobrk, M. Nabavi, D. Poulikakos, Investigation of a line-focused acoustic levitation for contactless transport of particles, J. Appl. Phys. 109 (2011) 093503.
[30] D. Foresti, M. Nabavi, D. Poulikakos, Contactless transport of matter in the first five resonance modes of a line-focused acoustic manipulatora, J. Acoust. Soc. Am. 131 (2012) 1029–1038.
[31] S. Santesson, S. Nilsson, Airborne chemistry: acoustic levitation in chemical analysis, Anal. Bioanal. Chem. 378 (2004) 1704–1709.
[32] M. Reißenweber, S. Krempel, G. Lindner, High-speed camera observation of multi-component droplet coagulation in an ultrasonic standing wave field, in: SPIE Micro + Nano Materials, Devices, and Applications, International Society for Optics and Photonics, 2013 (89234K-89234K-89210).
[33] E. Trinh, Compact acoustic levitation device for studies in fluid dynamics and material science in the laboratory and microgravity, Rev. Sci. Instrum. 56 (1985) 2059–2065.
[34] J. Li, P. Liu, H. Ding, W. Cao, Modeling characterization and optimization design for PZT transducer used in Near Field Acoustic Levitation, Sens. Actuators, A: Phys. 171 (2011) 260–265.
[35] S. Ueha, Y. Hashimoto, Y. Koike, Non-contact transportation using near-field acoustic levitation, Ultrasonics 38 (2000) 26–32.
[36] T. Kozuka, K. Yasui, T. Tuziuti, A. Towata, Y. Iida, Noncontact acoustic manipulation in air, Jpn. J. Appl. Phys. 46 (2007) 4948.
[37] V.N. Khmelev, A.N. Lebedev, S.N. Tsyganok, A.V. Shalunov, A.N. Galahov, K.V. Shalunova, Multifrequency ultrasonic transducer with stepped-plate disk, in: Micro/Nanotechnologies and Electron Devices, 2009. EDM 2009. International Conference and Seminar on, 2009, pp. 250–253.
[38] M. Hill, The selection of layer thicknesses to control acoustic radiation force profiles in layered resonators, J. Acoust. Soc. Am. 114 (2003) 2654–2661.
[39] M. Hill, Y. Shen, J.J. Hawkes, Modelling of layered resonators for ultrasonic separation, Ultrasonics 40 (2002) 385–392.
[40] D. Hutchins, A. Neild, Airborne ultrasound transducers, in: Ultrasonic Transducers: Materials and Design for Sensors, Actuators and Medical Applications, Elsevier Science, 2012, pp. 374.
[41] L. Evans, H. Bass, L. Sutherland, Atmospheric absorption of sound: theoretical predictions, J. Acoust. Soc. Am. 51 (1972) 1565–1575.
[42] M. Gröschl, Ultrasonic separation of suspended particles—Part I: Fundamentals, Acta Acust. Acust. 84 (1998) 432–447.
[43] K. Yosioka, Y. Kawasima, Acoustic radiation pressure on a compressible sphere, Acustica 5 (1955) 167–173.
[44] A. Haake, Micromanipulation of Small Particles with Ultrasound, Technische Universität, Berlin, 2004.
[45] H. Nowotny, E. Benes, General one-dimensional treatment of the layered piezoelectric resonator with two electrodes, J. Acoust. Soc. Am. 82 (1987) 513–521.
[46] V.M. Ristic, Principles of Acoustic Devices, Wiley, New York, NY, 1983.
[47] Ferroperm, Ferroperm Piezoceramics Catalogue, Ferroperm, 2003.
[48] L. Kinsler, A. Frey, H. Coppens, J. Sanders, H. Saunders, Fundamentals of acoustics, Am. Soc. Mech. Eng. (1983).
[49] J.N. Israelachvili, Adhesion and wetting phenomena, in: J.N. Israelachvili (Ed.), Intermolecular and Surface Forces, third ed., Academic Press, San Diego, CA, 2011, pp. 415–467 (17).
[50] Y. Li, D. Trauner, F.E. Talke, Effect of humidity on stiction and friction of the head/disk interface, IEEE Trans. Magn. 26 (1990) 2487–2489.

Biographies

Citsabehsan Devendran graduated with a Bachelor of Engineering (Hons) from Monash University in 2011. He is currently completing his Ph.D. research degree with the Laboratory for Microsystems in Monash University, Clayton Campus. His research interests lie within acoustofluidic particle manipulation and separation within liquid and air based microfluidic systems.

Duncan Billson is an associate professor in the School of Engineering, University of Warwick, and has developed his expertise in sensor technologies in both academic and industrial environments over the last ten years. After his BSc (Physics, Birmingham), and MSc (Optoelectronics, Herriot-Watt University, Edinburgh), he worked for TWI, Cambridge, UK, as a physicist in the NDE department. He then returned to Warwick, where he was awarded his PhD in early 1995. In 1996 Dr Billson went on to work for ABB-TRC, Ltd. and in 1998 he returned to Warwick as a research fellow and later as lecturer.

David Hutchins obtained his PhD from the University of Aston, UK. He then had various Postdoctoral Fellowship positions, and was subsequently made an associate professor at Queen's University, Canada. He joined the University of Warwick in the UK in 1988, and was made a Professor of Engineering in 1995. His research interests include noncontact ultrasound, micromachined transducers, ultrasonic imaging and nondestructive evaluation.

Adrian Neild received a PhD in engineering from the University of Warwick, in 2003. Subsequently, he worked as a postdoctoral researcher at the Institute for Mechanical Systems at ETH Zurich (Swiss Federal Institute of Technology Zurich). He has been a faculty member at Monash University since 2006 and is an Associate Professor and Australian Research Fellow. His research interests are in the fields of ultrasound, the use of acoustics for actuation of micro-fluidic systems and particle manipulation.

Chapter 6

Conclusions and Future Work

This chapter will summarise the contribution of the work discussed throughout this thesis. Following this, ongoing work and recommendation on future work will be presented.

6.1 Contributions

The knowledge gap in evidently necessary microfluidic batch process systems for sample preparation is apparent. Therefore, the focus of the work carried out within this thesis was to widen the understanding and implementation of these systems. Throughout this thesis, new systems for particle manipulation in liquid and air based batch process systems were developed. Applicability of acoustics or more specifically, acoustofluidics within microfluidic systems, opens up the possibility of realising these systems. Utilising acoustics, the exertion of non-contact gentle, yet robust range of forces that can be selectively used for various applications. The following will discuss the specific contributions that stem from each of the chapters included in this thesis.

Chapter 3

In this chapter, a method to separate particles based on their size within a static fluid system was developed. Here, the integration of ARF to collect the particles and acoustic streaming induced drag forces to assist the delivery of smaller particles to the open fluid-air interface using BAW. Computational modelling using COMSOL Multiphysics, a finite element analysis package predicted the behaviour of particles of varying sizes. The developed numerical models suggests the ability to tune the critical particle separation size by scaling the size of the system. With the combination of several key factors (i.e. excitation amplitude, short and repetitive excitations and channel perimeter pre-filling with a buffer) particle migration to the free open surface was enhanced experimentally. The separation of 3 μm and 10 μm particles was achieved at a single frequency by exploiting the differing force (i.e. ARF and acoustic streaming induced drag) dominated mechanisms experienced by the particles. Finally, the separated 3 μm particles at the open surface was extracted with high purity of 99% using a micro-sampling pipette.

Chapter 4

Here, an improvement to the performance of size-deterministic particle separation to further reduce the separation size within a batch system is demonstrated. SAW is used as the excitation method as opposed to BAW enabling several key factors to realise the proposed system. The integration of TSAW and SSAW (scales differently to particle size as discussed in Chapter 4) at acoustic wavelengths that approach the size of the particles are utilised as the underlying sorting mechanism. The sorting is enhanced by sweeping the frequency over a range to allow migration of the SSAW dominated particles to migrate beyond a wavelength. Computational numerical analysis, using COMSOL Multiphysics demonstrates the sorting mechanism and suggests that the shift from SSAW dominant to TSAW dominant forcing can be achieved by altering the wavelength of excitation. Experimentally, two sets of mixed particles, 7 μm and 5.1 μm using a frequency range of 60 to 90 MHz and 5.1 μm from 3.1 μm particles over a range of 70 to 120 MHz are successfully separated.

Chapter 5

The demand and underwhelming investigation into very small sub-100 μm particle manipulation in air is addressed here. A individualised particle manipulation is proposed to realised a full 3D non-contact acoustic trapping microgripper. Knowledge and understanding of acoustic radiation forces in liquid based systems is transferred across for operation in air. As a starting point, optimisation of a layered resonator accommodating for acoustic attenuation and material thickness and selection is investigated. It is suggested, to trap and manipulate micron-sized particle, the wavelength should be decreased. However, as the frequency is increased, the acoustic energy lost due to attenuation which scales with frequency, results in an optimum operational frequency. Furthermore, an analytical 1D model is developed to predict ideal layer thickness and material properties to be fabricated experimentally. Finally, experimentally, dense PMMA particles as small as 14.8 μm have been successfully trapped in air. This design optimisation serves as a building block to realising a full 3D non-contact acoustic trapping microgripper.

6.2 Ongoing and Future Work

As outlined in this thesis, investigations into batch process systems utilising acoustics has resulted in several contributions. However, the need for further development into batch process microfluidic systems is evidently necessary. This section will briefly discuss some ongoing and potential avenues for future research.

In Chapter 4, it is demonstrated that particles can be sorted based on size by employing TSAW and SSAW simultaneously. The ability to sort particles based on their characteristics (i.e. mechanical properties, size and shape) is of immense potential. Based on the sorting capabilities and the understanding of this system, blood sorting into its individual constituents (i.e. white blood cells, platelets and plasma). Furthermore, this

technique is currently being developed for enrichment and sorting of diseased circulating cells that differ in terms of mechanical properties. For example, human red blood cells that are infected with one of four species of a parasite that belongs to the genus *Plasmodium*. [221] Such an infection increases the stiffness [222, 223] of the cells along with its adhesive properties. The increased stiffness decreases the compressibility, κ and therefore, an acoustic contrast between healthy and infected cells exists. Here, the developed system aims to sort these healthy and infected cells from each other by exploiting the altered properties. The current work will look into developing an early detection tool of malaria parasite infected cells within batch process systems.

As discussed in Chapter 5 (Section 5.1), the design optimisation serves as a precursor towards developing a complete 3D individualised particle transport. Thus, this work will be further developed to integrate a modified layered resonator design that allows for 3D particle mobility in air with the use of an acoustic trapping microgripper. As discussed within the publication in Section 5.2, the major issue and limiting factor of manipulating particles of very small sizes is as a result of stiction with the donor surface, associated with the high surface area to size ratio of microparticles. Therefore, investigation into reducing adhesion properties arising from stiction is suggested. Finally, a reflector surface that is able to establish a resonant acoustic field as a stand-alone, self-confined component will need to be integrated, allowing a complete spatial control of the particle.

"*The process of scientific discovery is, in effect, a continual flight from wonder*"

Albert Einstein

Bibliography

[1] Mei He, Jennifer Crow, Marc Roth, Yong Zeng, and Andrew K Godwin. Integrated immunoisolation and protein analysis of circulating exosomes using microfluidic technology. *Lab on a Chip*, 14(19):3773–3780, 2014.

[2] Jordi Vila-Planas, Elisabet Fernández-Rosas, Bergoi Ibarlucea, Stefanie Demming, Carme Nogués, Jose A Plaza, Carlos Domínguez, Stephanus Büttgenbach, and Andreu Llobera. Cell analysis using a multiple internal reflection photonic lab-on-a-chip. *Nature Protocols*, 6(10):1642–1655, 2011.

[3] Irena Barbulovic-Nad, Sam H Au, and Aaron R Wheeler. A microfluidic platform for complete mammalian cell culture. *Lab on a Chip*, 10(12):1536–1542, 2010.

[4] Šeila Selimović, Mehmet R Dokmeci, and Ali Khademhosseini. Organs-on-a-chip for drug discovery. *Current Opinion in Pharmacology*, 13(5):829–833, 2013.

[5] Steve CC Shih, Hao Yang, Mais J Jebrail, Ryan Fobel, Nathan McIntosh, Osama Y Al-Dirbashi, Pranesh Chakraborty, and Aaron R Wheeler. Dried blood spot analysis by digital microfluidics coupled to nanoelectrospray ionization mass spectrometry. *Analytical Chemistry*, 84(8):3731–3738, 2012.

[6] Wei Wang, Rui Xie, Xiao-Jie Ju, Tao Luo, Li Liu, David A Weitz, and Liang-Yin Chu. Controllable microfluidic production of multicomponent multiple emulsions. *Lab on a Chip*, 11(9):1587–1592, 2011.

[7] Andres W Martinez, Scott T Phillips, and George M Whitesides. Three-dimensional microfluidic devices fabricated in layered paper and tape. *Proceedings of the National Academy of Sciences*, 105(50):19606–19611, 2008.

[8] Daniel Therriault, Scott R White, and Jennifer A Lewis. Chaotic mixing in three-dimensional microvascular networks fabricated by direct-write assembly. *Nature Materials*, 2(4):265–271, 2003.

[9] Iain A Larmour, Steven EJ Bell, and Graham C Saunders. Remarkably simple fabrication of superhydrophobic surfaces using electroless galvanic deposition. *Angewandte Chemie*, 119(10):1740–1742, 2007.

[10] Helen Song, Michelle R Bringer, Joshua D Tice, Cory J Gerdts, and Rustem F Ismagilov. Experimental test of scaling of mixing by chaotic advection in droplets

moving through microfluidic channels. *Applied Physics Letters*, 83(22):4664–4666, 2003.

[11] LLA Adams, Thomas E Kodger, Shin-Hyun Kim, Ho Cheng Shum, Thomas Franke, and David A Weitz. Single step emulsification for the generation of multi-component double emulsions. *Soft Matter*, 8(41):10719–10724, 2012.

[12] Nicole Pamme and Andreas Manz. On-chip free-flow magnetophoresis: continuous flow separation of magnetic particles and agglomerates. *Analytical Chemistry*, 76(24):7250–7256, 2004.

[13] David W Inglis. Efficient microfluidic particle separation arrays. *Applied Physics Letters*, 94(1):013510, 2009.

[14] Filip Petersson, Lena Åberg, Ann-Margret Swärd-Nilsson, and Thomas Laurell. Free flow acoustophoresis: microfluidic-based mode of particle and cell separation. *Analytical Chemistry*, 79(14):5117–5123, 2007.

[15] Daniel R Gossett, Westbrook M Weaver, Albert J Mach, Soojung Claire Hur, Henry Tat Kwong Tse, Wonhee Lee, Hamed Amini, and Dino Di Carlo. Label-free cell separation and sorting in microfluidic systems. *Analytical and Bioanalytical Chemistry*, 397(8):3249–3267, 2010.

[16] David G Grier. A revolution in optical manipulation. *Nature*, 424(6950):810–816, 2003.

[17] DA Hutchins and A Neild. Airborne ultrasound transducers. *Ultrasonic Transducers: Materials and Design for Sensors, Actuators and Medical Applications*, page 374, 2012.

[18] SS Sadhal. Acoustofluidics 13: Analysis of acoustic streaming by perturbation methods. *Lab on a Chip*, 12(13):2292–2300, 2012.

[19] Martin Wiklund, Roy Green, and Mathias Ohlin. Acoustofluidics 14: Applications of acoustic streaming in microfluidic devices. *Lab on a Chip*, 12(14):2438–2451, 2012.

[20] Ivo Leibacher, Peter Reichert, and Jürg Dual. Microfluidic droplet handling by bulk acoustic wave (BAW) acoustophoresis. *Lab on a Chip*, 15:2896–2905, 2015.

[21] Patrick Thévoz, Jonathan D. Adams, Herbert Shea, Henrik Bruus, and H. Tom Soh. Acoustophoretic synchronization of mammalian cells in microchannels. *Analytical Chemistry*, 82(7):3094–3098, 2010. PMID: 20199060.

[22] Martyn Hill, Rosemary J Townsend, and Nicholas R Harris. Modelling for the robust design of layered resonators for ultrasonic particle manipulation. *Ultrasonics*, 48(6):521–528, 2008.

[23] Marco A. B. Andrade, Nicolás Pérez, and Julio C. Adamowski. Particle manipulation by a non-resonant acoustic levitator. *Applied Physics Letters*, 106(1), 2015.

[24] Thomas Laurell and Andreas Lenshof. *Microscale Acoustofluidics*. Royal Society of Chemistry, 2014.

[25] Richard Shilton, Ming K Tan, Leslie Y Yeo, and James R Friend. Particle concentration and mixing in microdrops driven by focused surface acoustic waves. *Journal of Applied Physics*, 104(1):014910, 2008.

[26] Jinjie Shi, Daniel Ahmed, Xiaole Mao, Sz-Chin Steven Lin, Aitan Lawit, and Tony Jun Huang. Acoustic tweezers: patterning cells and microparticles using standing surface acoustic waves (SSAW). *Lab on a Chip*, 9(20):2890–2895, 2009.

[27] Ghulam Destgeer, Byung Hang Ha, Jin Ho Jung, and Hyung Jin Sung. Submicron separation of microspheres via travelling surface acoustic waves. *Lab on a Chip*, 14:4665–4672, 2014.

[28] Xiaoyun Ding, Sz-Chin Steven Lin, Brian Kiraly, Hongjun Yue, Sixing Li, I-Kao Chiang, Jinjie Shi, Stephen J Benkovic, and Tony Jun Huang. On-chip manipulation of single microparticles, cells, and organisms using surface acoustic waves. *Proceedings of the National Academy of Sciences*, 109(28):11105–11109, 2012.

[29] Xiaoyun Ding, Sz-Chin Steven Lin, Michael Ian Lapsley, Sixing Li, Xiang Guo, Chung Yu Chan, I-Kao Chiang, Lin Wang, J. Philip McCoy, and Tony Jun Huang. Standing surface acoustic wave (SSAW) based multichannel cell sorting. *Lab on a Chip*, 12:4228–4231, 2012.

[30] Patrick Tabeling. *Introduction to microfluidics*. Oxford University Press, 2010.

[31] Citsabehsan Devendran, Ian Gralinski, and Adrian Neild. Separation of particles using acoustic streaming and radiation forces in an open microfluidic channel. *Microfluidics and Nanofluidics*, 17(5):879–890, 2014.

[32] Citsabehsan Devendran, Duncan R. Billson, David A. Hutchins, and Adrian Neild. Optimisation of an acoustic resonator for particle manipulation in air. *Sensors and Actuators B: Chemical*, 224:529 – 538, 2016.

[33] Citsabehsan Devendran, Nipuna R. Gunasekara, David J. Collins, and Adrian Neild. Batch process particle separation using surface acoustic waves (SAW): integration of travelling and standing SAW. *RSC Advances*, 6:5856–5864, 2016.

[34] Citsabehsan Devendran, Duncan R. Billson, David A. Hutchins, Tuncay Alan, and Adrian Neild. Acoustic resonator optimisation for airborne particle manipulation. *Physics Procedia*, 70:6 – 9, 2015. Proceedings of the 2015 ICU International Congress on Ultrasonics, Metz, France.

[35] Eric K Sackmann, Anna L Fulton, and David J Beebe. The present and future role of microfluidics in biomedical research. *Nature*, 507(7491):181–189, 2014.

[36] Nam-Trung Nguyen and Steven T Wereley. *Fundamentals and applications of microfluidics*. Artech House, 2002.

[37] Howard A Stone, Abraham D Stroock, and Armand Ajdari. Engineering flows in small devices: microfluidics toward a lab-on-a-chip. *Annu. Rev. Fluid Mech.*, 36:381–411, 2004.

[38] Maxine A McClain, Christopher T Culbertson, Stephen C Jacobson, and J Michael Ramsey. Flow cytometry of *escherichia coli* on microfluidic devices. *Analytical Chemistry*, 73(21):5334–5338, 2001.

[39] Dieter Schmalzing, Lance Koutny, Aram Adourian, Phillip Belgrader, Paul Matsudaira, and Daniel Ehrlich. DNA typing in thirty seconds with a microfabricated device. *Proceedings of the National Academy of Sciences*, 94(19):10273–10278, 1997.

[40] Ivonne Schneegaß, Reiner Bräutigam, and Johann Michael Köhler. Miniaturized flow-through PCR with different template types in a silicon chip thermocycler. *Lab on a Chip*, 1(1):42–49, 2001.

[41] David A LaVan, David M Lynn, and Robert Langer. Moving smaller in drug discovery and delivery. *Nature Reviews Drug Discovery*, 1(1):77–84, 2002.

[42] JGE Gardeniers and A Van den Berg. Lab-on-a-chip systems for biomedical and environmental monitoring. *Analytical and Bioanalytical Chemistry*, 378(7):1700–1703, 2004.

[43] Curtis D Chin, Vincent Linder, and Samuel K Sia. Lab-on-a-chip devices for global health: past studies and future opportunities. *Lab on a Chip*, 7(1):41–57, 2007.

[44] Priscilla Rogers, Ian Gralinski, Cameron Galtry, and Adrian Neild. Selective particle and cell clustering at air-liquid interfaces within ultrasonic microfluidic systems. *Microfluidics and Nanofluidics*, 14(3-4):469–477, 2013.

[45] Ghulam Destgeer, Kyung Heon Lee, Jin Ho Jung, Anas Alazzam, and Hyung Jin Sung. Continuous separation of particles in a pdms microfluidic channel via travelling surface acoustic waves (TSAW). *Lab on a Chip*, 13(21):4210–4216, 2013.

[46] L. Gorkov. On the forces acting on a small particle in an acoustical field in an ideal fluid. *Soviet Physics Doklady*, 1962.

[47] Marina Reißenweber, Sandro Krempel, and Gerhard Lindner. High-speed camera observation of multi-component droplet coagulation in an ultrasonic standing wave field. In *SPIE Micro+ Nano Materials, Devices, and Applications*, pages 89234K–89234K. International Society for Optics and Photonics, 2013.

[48] WJ Xie, CD Cao, YJ Lü, and B Wei. Levitation of iridium and liquid mercury by ultrasound. *Physical review letters*, 89(10):104304, 2002.

[49] Daniele Foresti, Majid Nabavi, Mirko Klingauf, Aldo Ferrari, and Dimos Poulikakos. Acoustophoretic contactless transport and handling of matter in air. *Proceedings of the National Academy of Sciences*, 110(31):12549–12554, 2013.

[50] Daniele Foresti, Majid Nabavi, and Dimos Poulikakos. Contactless transport of matter in the first five resonance modes of a line-focused acoustic manipulator. *The Journal of the Acoustical Society of America*, 131(2):1029–1038, 2012.

[51] Andréas Manz, N Graber, and H Michael Widmer. Miniaturized total chemical analysis systems: a novel concept for chemical sensing. *Sensors and Actuators B: Chemical*, 1(1):244–248, 1990.

[52] Yuksel Temiz, Robert D Lovchik, Govind V Kaigala, and Emmanuel Delamarche. Lab-on-a-chip devices: How to close and plug the lab? *Microelectronic Engineering*, 132:156–175, 2015.

[53] Daniel Figeys and Devanand Pinto. Lab-on-a-chip: a revolution in biological and medical sciences. *Analytical Chemistry*, 72(9):330–A, 2000.

[54] Amir M Foudeh, Tohid Fatanat Didar, Teodor Veres, and Maryam Tabrizian. Microfluidic designs and techniques using lab-on-a-chip devices for pathogen detection for point-of-care diagnostics. *Lab on a Chip*, 12(18):3249–3266, 2012.

[55] Vijay Srinivasan, Vamsee K Pamula, and Richard B Fair. An integrated digital microfluidic lab-on-a-chip for clinical diagnostics on human physiological fluids. *Lab on a Chip*, 4(4):310–315, 2004.

[56] Anna J Tüdős, Geert AJ Besselink, and Richard BM Schasfoort. Trends in miniaturized total analysis systems for point-of-care testing in clinical chemistry. *Lab on a Chip*, 1(2):83–95, 2001.

[57] Chong H Ahn, Jin-Woo Choi, Gregory Beaucage, Joseph H Nevin, Jeong-Bong Lee, Aniruddha Puntambekar, and Jae Y Lee. Disposable smart lab on a chip for point-of-care clinical diagnostics. *Proceedings of the IEEE*, 92(1):154–173, 2004.

[58] Mehdi Ghodbane, Elizabeth C Stucky, Tim J Maguire, Rene S Schloss, David I Shreiber, Jeffrey D Zahn, and Martin L Yarmush. Development and validation of a microfluidic immunoassay capable of multiplexing parallel samples in microliter volumes. *Lab on a Chip*, 15(15):3211–3221, 2015.

[59] Alphonsus HC Ng, M Dean Chamberlain, Haozhong Situ, Victor Lee, and Aaron R Wheeler. Digital microfluidic immunocytochemistry in single cells. *Nature Communications*, 6, 2015.

[60] Mohtashim H Shamsi, Kihwan Choi, Alphonsus HC Ng, and Aaron R Wheeler. A digital microfluidic electrochemical immunoassay. *Lab on a Chip*, 14(3):547–554, 2014.

[61] J Wiest, T Stadthagen, M Schmidhuber, M Brischwein, J Ressler, U Raeder, H Grothe, A Melzer, and B Wolf. Intelligent mobile lab for metabolics in environmental monitoring. *Analytical Letters*, 39(8):1759–1771, 2006.

[62] Leanne Marle and Gillian M Greenway. Microfluidic devices for environmental monitoring. *TrAC Trends in Analytical Chemistry*, 24(9):795–802, 2005.

[63] BL Karger, YH Chu, and F Foret. Capillary electrophoresis of proteins and nucleic acids. *Annual Review of Biophysics and Biomolecular Structure*, 24(1):579–610, 1995.

[64] Adam T Woolley and Richard A Mathies. Ultra-high-speed DNA fragment separations using microfabricated capillary array electrophoresis chips. *Proceedings of the National Academy of Sciences*, 91(24):11348–11352, 1994.

[65] Dieter Schmalzing, Aram Adourian, Lance Koutny, Liuda Ziaugra, Paul Matsudaira, and Daniel Ehrlich. DNA sequencing on microfabricated electrophoretic devices. *Analytical Chemistry*, 70(11):2303–2310, 1998.

[66] David J Collins, Tuncay Alan, Kristian Helmerson, and Adrian Neild. Surface acoustic waves for on-demand production of picoliter droplets and particle encapsulation. *Lab on a Chip*, 13(16):3225–3231, 2013.

[67] Petra S Dittrich and Andreas Manz. Lab-on-a-chip: microfluidics in drug discovery. *Nature Reviews Drug Discovery*, 5(3):210–218, 2006.

[68] Amir M Ghaemmaghami, Matthew J Hancock, Helen Harrington, Hirokazu Kaji, and Ali Khademhosseini. Biomimetic tissues on a chip for drug discovery. *Drug Discovery Today*, 17(3):173–181, 2012.

[69] Peter Woias. Micropumps-past, progress and future prospects. *Sensors and Actuators B: Chemical*, 105(1):28–38, 2005.

[70] JC Rife, MI Bell, JS Horwitz, MN Kabler, RCY Auyeung, and WJ Kim. Miniature valveless ultrasonic pumps and mixers. *Sensors and Actuators A: Physical*, 86(1):135–140, 2000.

[71] Stefano Oberti, Adrian Neild, and Tuck Wah Ng. Microfluidic mixing under low frequency vibration. *Lab on a Chip*, 9(10):1435–1438, 2009.

[72] Jue Nee Tan and Adrian Neild. Microfluidic mixing in a y-junction open channel. *AIP Advances*, 2(3):032160, 2012.

[73] Priscilla Rogers and Adrian Neild. Selective particle trapping using an oscillating microbubble. *Lab on a Chip*, 11(21):3710–3715, 2011.

[74] Hartmut Gau, Stephan Herminghaus, Peter Lenz, and Reinhard Lipowsky. Liquid morphologies on structured surfaces: from microchannels to microchips. *Science*, 283(5398):46–49, 1999.

[75] F Gattiker, F Umbrecht, J Neuenschwander, U Sennhauser, and C Hierold. Novel ultrasound read-out for a wireless implantable passive strain sensor (WIPSS). *Sensors and Actuators A: Physical*, 145:291–298, 2008.

[76] Yizhong Wang, Yuejun Zhao, and Sung Kwon Cho. Efficient in-droplet separation of magnetic particles for digital microfluidics. *Journal of Micromechanics and Microengineering*, 17(10):2148, 2007.

[77] Nan Xia, Tom P Hunt, Brian T Mayers, Eben Alsberg, George M Whitesides, Robert M Westervelt, and Donald E Ingber. Combined microfluidic-micromagnetic separation of living cells in continuous flow. *Biomedical Microdevices*, 8(4):299–308, 2006.

[78] MP MacDonald, GC Spalding, and Kishan Dholakia. Microfluidic sorting in an optical lattice. *Nature*, 426(6965):421–424, 2003.

[79] Benjamin Landenberger, Henning Höfemann, Simon Wadle, and Alexander Rohrbach. Microfluidic sorting of arbitrary cells with dynamic optical tweezers. *Lab on a Chip*, 12(17):3177–3183, 2012.

[80] Hadi Shafiee, Michael B Sano, Erin A Henslee, John L Caldwell, and Rafael V Davalos. Selective isolation of live/dead cells using contactless dielectrophoresis (cDEP). *Lab on a Chip*, 10(4):438–445, 2010.

[81] Peter RC Gascoyne and Jody Vykoukal. Particle separation by dielectrophoresis. *Electrophoresis*, 23(13):1973, 2002.

[82] Seungkyung Park, Yi Zhang, Tza-Huei Wang, and Samuel Yang. Continuous dielectrophoretic bacterial separation and concentration from physiological media of high conductivity. *Lab on a Chip*, 11(17):2893–2900, 2011.

[83] Jeonghun Nam, Yongjin Lee, and Sehyun Shin. Size-dependent microparticles separation through standing surface acoustic waves. *Microfluidics and Nanofluidics*, 11(3):317–326, 2011.

[84] Jeonghun Nam, Hyunjung Lim, Dookon Kim, and Sehyun Shin. Separation of platelets from whole blood using standing surface acoustic waves in a microchannel. *Lab on a Chip*, 11(19):3361–3364, 2011.

[85] Jinjie Shi, Hua Huang, Zak Stratton, Yiping Huang, and Tony Jun Huang. Continuous particle separation in a microfluidic channel via standing surface acoustic waves (SSAW). *Lab on a Chip*, 9(23):3354–3359, 2009.

[86] Filip Petersson, Andreas Nilsson, Cecilia Holm, Henrik Jönsson, and Thomas Laurell. Continuous separation of lipid particles from erythrocytes by means of laminar flow and acoustic standing wave forces. *Lab on a Chip*, 5(1):20–22, 2005.

[87] Masumi Yamada, Megumi Nakashima, and Minoru Seki. Pinched flow fractionation: continuous size separation of particles utilizing a laminar flow profile in a pinched microchannel. *Analytical Chemistry*, 76(18):5465–5471, 2004.

[88] J McGrath, M Jimenez, and H Bridle. Deterministic lateral displacement for particle separation: a review. *Lab on a Chip*, 14(21):4139–4158, 2014.

[89] Hazel M Davey and Douglas B Kell. Flow cytometry and cell sorting of heterogeneous microbial populations: the importance of single-cell analyses. *Microbiological Reviews*, 60(4):641–696, 1996.

[90] Ninnuja Sivanantha, Charles Ma, David J Collins, Muhsincan Sesen, Jason Brenker, Ross L Coppel, Adrian Neild, and Tuncay Alan. Characterization of adhesive properties of red blood cells using surface acoustic wave induced flows for rapid diagnostics. *Applied Physics Letters*, 105(10):103704, 2014.

[91] Michael Eisenstein. Cell sorting: divide and conquer. *Nature*, 441(7097):1179–1185, 2006.

[92] Hoyoung Yun, Kisoo Kim, and Won Gu Lee. Cell manipulation in microfluidics. *Biofabrication*, 5(2):022001, 2013.

[93] Emma Eriksson, Kristin Sott, Fredrik Lundqvist, Martin Sveningsson, Jan Scrimgeour, Dag Hanstorp, Mattias Goksör, and Annette Granéli. A microfluidic device for reversible environmental changes around single cells using optical tweezers for cell selection and positioning. *Lab on a Chip*, 10(5):617–625, 2010.

[94] Arnaud Bertsch, Stephan Heimgartner, Peter Cousseau, and Philippe Renaud. Static micromixers based on large-scale industrial mixer geometry. *Lab on a Chip*, 1(1):56–60, 2001.

[95] Tae Woo Lim, Yong Son, Yu Jin Jeong, Dong-Yol Yang, Hong-Jin Kong, Kwang-Sup Lee, and Dong-Pyo Kim. Three-dimensionally crossing manifold micro-mixer for fast mixing in a short channel length. *Lab on a Chip*, 11(1):100–103, 2011.

[96] Arjun P Sudarsan and Victor M Ugaz. Multivortex micromixing. *Proceedings of the National Academy of Sciences*, 103(19):7228–7233, 2006.

[97] Helen Song, Delai L Chen, and Rustem F Ismagilov. Reactions in droplets in microfluidic channels. *Angewandte Chemie International Edition*, 45(44):7336–7356, 2006.

[98] Andres W Martinez, Scott T Phillips, Manish J Butte, and George M Whitesides. Patterned paper as a platform for inexpensive, low-volume, portable bioassays. *Angewandte Chemie International Edition*, 46(8):1318–1320, 2007.

[99] Andres W Martinez, Scott T Phillips, Benjamin J Wiley, Malancha Gupta, and George M Whitesides. FLASH: a rapid method for prototyping paper-based microfluidic devices. *Lab on a Chip*, 8(12):2146–2150, 2008.

[100] Muhsincan Sesen, Tuncay Alan, and Adrian Neild. Microfluidic on-demand droplet merging using surface acoustic waves. *Lab on a Chip*, 2014.

[101] P Ferraro, S Coppola, S Grilli, M Paturzo, and V Vespini. Dispensing nano-pico droplets and liquid patterning by pyroelectrodynamic shooting. *Nature Nanotechnology*, 5(6):429–435, 2010.

[102] Haiyan Li, James R Friend, and Leslie Y Yeo. Surface acoustic wave concentration of particle and bioparticle suspensions. *Biomedical Microdevices*, 9(5):647–656, 2007.

[103] Rafael Gómez-Sjöberg, Dallas T Morisette, and Rashid Bashir. Impedance microbiology-on-a-chip: Microfluidic bioprocessor for rapid detection of bacterial metabolism. *Journal of Microelectromechanical Systems*, 14(4):829–838, 2005.

[104] Jean-Christophe Baret, Oliver J Miller, Valerie Taly, Michaël Ryckelynck, Abdeslam El-Harrak, Lucas Frenz, Christian Rick, Michael L Samuels, J Brian Hutchison, Jeremy J Agresti, et al. Fluorescence-activated droplet sorting (FADS): efficient microfluidic cell sorting based on enzymatic activity. *Lab on a Chip*, 9(13):1850–1858, 2009.

[105] Sungyoung Choi, Jeffrey M Karp, and Rohit Karnik. Cell sorting by deterministic cell rolling. *Lab on a Chip*, 12(8):1427–1430, 2012.

[106] Xiaolin Wang, Shuxun Chen, Marco Kong, Zuankai Wang, Kevin D Costa, Ronald A Li, and Dong Sun. Enhanced cell sorting and manipulation with combined optical tweezer and microfluidic chip technologies. *Lab on a Chip*, 11(21):3656–3662, 2011.

[107] Kee Suk Ryu, Kashan Shaikh, Edgar Goluch, Zhifang Fan, and Chang Liu. Micro magnetic stir-bar mixer integrated with parylene microfluidic channels. *Lab on a Chip*, 4(6):608–613, 2004.

[108] Chunsun Zhang, Da Xing, and Yuyuan Li. Micropumps, microvalves, and micromixers within PCR microfluidic chips: advances and trends. *Biotechnology Advances*, 25(5):483–514, 2007.

[109] Hoang Van Phan, M Bulut Coşkun, Muhsincan Şeşen, Gregory Pandraud, Adrian Neild, and Tuncay Alan. Vibrating membrane with discontinuities for rapid and efficient microfluidic mixing. *Lab on a Chip*, 2015.

[110] Jessica Hultström, Otto Manneberg, Katja Dopf, Hans M Hertz, Hjalmar Brismar, and Martin Wiklund. Proliferation and viability of adherent cells manipulated by standing-wave ultrasound in a microfluidic chip. *Ultrasound in Medicine and Biology*, 33(1):145–151, 2007.

[111] Lo-Chang Hsiung, Chun-Hui Yang, Chi-Li Chiu, Chen-Lin Chen, Yueh Wang, Hsinyu Lee, Ji-Yen Cheng, Ming-Chih Ho, and Andrew M Wo. A planar interdigitated ring electrode array via dielectrophoresis for uniform patterning of cells. *Biosensors and Bioelectronics*, 24(4):869–875, 2008.

[112] Hang Lu, Martin A Schmidt, and Klavs F Jensen. A microfluidic electroporation device for cell lysis. *Lab on a Chip*, 5(1):23–29, 2005.

[113] Chia-Yen Lee, Gwo-Bin Lee, Jr-Lung Lin, Fu-Chun Huang, and Chia-Sheng Liao. Integrated microfluidic systems for cell lysis, mixing/pumping and DNA amplification. *Journal of Micromechanics and Microengineering*, 15(6):1215, 2005.

[114] S Winoto-Morbach, V Tchikov, and W Mueller-Ruchholtz. Magnetophoresis: I. detection of magnetically labeled cells. *Journal of Clinical Laboratory Analysis*, 8(6):400–406, 1994.

[115] Maciej Zborowski and Jeffrey J Chalmers. Magnetophoresis: Fundamentals and applications. *Wiley Encyclopedia of Electrical and Electronics Engineering*.

[116] Akira Ito, Masashige Shinkai, Hiroyuki Honda, and Takeshi Kobayashi. Medical application of functionalized magnetic nanoparticles. *Journal of Bioscience and Bioengineering*, 100(1):1–11, 2005.

[117] C Wilhelm, F Gazeau, J Roger, JN Pons, and J-C Bacri. Interaction of anionic superparamagnetic nanoparticles with cells: kinetic analyses of membrane adsorption and subsequent internalization. *Langmuir*, 18(21):8148–8155, 2002.

[118] Nicole Pamme and Claire Wilhelm. Continuous sorting of magnetic cells via on-chip free-flow magnetophoresis. *Lab on a Chip*, 6(8):974–980, 2006.

[119] A Hultgren, M Tanase, CS Chen, GJ Meyer, and DH Reich. Cell manipulation using magnetic nanowires. *Journal of Applied Physics*, 93(10):7554–7556, 2003.

[120] Ana Egatz-Gómez, Sonia Melle, Antonio A García, SA Lindsay, M Márquez, P Dominguez-Garcia, Miguel A Rubio, ST Picraux, JL Taraci, T Clement, et al. Discrete magnetic microfluidics. *Applied Physics Letters*, 89(3):34106–34106, 2006.

[121] Arthur Ashkin, JM Dziedzic, JE Bjorkholm, and Steven Chu. Observation of a single-beam gradient force optical trap for dielectric particles. *Optics Letters*, 11(5):288–290, 1986.

[122] Jungwoo Lee, Kanglyeol Ha, and K Kirk Shung. A theoretical study of the feasibility of acoustical tweezers: ray acoustics approach. *The Journal of the Acoustical Society of America*, 117(5):3273–3280, 2005.

[123] Arthur Ashkin. Optical trapping and manipulation of neutral particles using lasers. *Proceedings of the National Academy of Sciences*, 94(10):4853–4860, 1997.

[124] Youhua Tan, Dong Sun, Jinzhi Wang, and Wenhao Huang. Mechanical characterization of human red blood cells under different osmotic conditions by robotic manipulation with optical tweezers. *Biomedical Engineering, IEEE Transactions on*, 57(7):1816–1825, 2010.

[125] Xujing Wang, Xiao-Bo Wang, and Peter RC Gascoyne. General expressions for dielectrophoretic force and electrorotational torque derived using the Maxwell stress tensor method. *Journal of Electrostatics*, 39(4):277–295, 1997.

[126] DS Clague and EK Wheeler. Dielectrophoretic manipulation of macromolecules: The electric field. *Physical Review E*, 64(2):026605, 2001.

[127] Tohid Fatanat Didar and Maryam Tabrizian. Adhesion based detection, sorting and enrichment of cells in microfluidic lab-on-chip devices. *Lab on a Chip*, 10(22):3043–3053, 2010.

[128] Abhishek Jain and Jonathan D Posner. Particle dispersion and separation resolution of pinched flow fractionation. *Analytical Chemistry*, 80(5):1641–1648, 2008.

[129] Tomoki Morijiri, Satoshi Sunahiro, Masashi Senaha, Masumi Yamada, and Minoru Seki. Sedimentation pinched-flow fractionation for size-and density-based particle sorting in microchannels. *Microfluidics and Nanofluidics*, 11(1):105–110, 2011.

[130] Dongeun Huh, Joong Hwan Bahng, Yibo Ling, Hsien-Hung Wei, Oliver D Kripfgans, J Brian Fowlkes, James B Grotberg, and Shuichi Takayama. Gravity-driven microfluidic particle sorting device with hydrodynamic separation amplification. *Analytical Chemistry*, 79(4):1369–1376, 2007.

[131] Masumi Yamada and Minoru Seki. Hydrodynamic filtration for on-chip particle concentration and classification utilizing microfluidics. *Lab on a Chip*, 5(11):1233–1239, 2005.

[132] Masumi Yamada, Kyoko Kano, Yukiko Tsuda, Jun Kobayashi, Masayuki Yamato, Minoru Seki, and Teruo Okano. Microfluidic devices for size-dependent separation of liver cells. *Biomedical Microdevices*, 9(5):637–645, 2007.

[133] Sergey S Shevkoplyas, Tatsuro Yoshida, Lance L Munn, and Mark W Bitensky. Biomimetic autoseparation of leukocytes from whole blood in a microfluidic device. *Analytical Chemistry*, 77(3):933–937, 2005.

[134] Rainer D Jäggi, Roger Sandoz, and Carlo S Effenhauser. Microfluidic depletion of red blood cells from whole blood in high-aspect-ratio microchannels. *Microfluidics and Nanofluidics*, 3(1):47–53, 2007.

[135] Magalie Faivre, Manouk Abkarian, Kimberly Bickraj, and Howard A Stone. Geometrical focusing of cells in a microfluidic device: an approach to separate blood plasma. *Biorheology*, 43(2):147–160, 2006.

[136] Lotien Richard Huang, Edward C Cox, Robert H Austin, and James C Sturm. Continuous particle separation through deterministic lateral displacement. *Science*, 304(5673):987–990, 2004.

[137] Despina Bazou, Roisin Kearney, Fiona Mansergh, Celine Bourdon, Jane Farrar, and Michael Wride. Gene expression analysis of mouse embryonic stem cells following levitation in an ultrasound standing wave trap. *Ultrasound in Medicine and Biology*, 37(2):321–330, 2011.

[138] Priscilla R Rogers, James R Friend, and Leslie Y Yeo. Exploitation of surface acoustic waves to drive size-dependent microparticle concentration within a droplet. *Lab on a Chip*, 10(21):2979–2985, 2010.

[139] David J Collins, Ofer Manor, Andreas Winkler, Hagen Schmidt, James R Friend, and Leslie Y Yeo. Atomization off thin water films generated by high-frequency substrate wave vibrations. *Physical Review E*, 86(5):056312, 2012.

[140] Zeno Guttenberg, Helena Müller, Heiko Habermüller, Andreas Geisbauer, Jürgen Pipper, Jana Felbel, Mark Kielpinski, Jürgen Scriba, and Achim Wixforth. Planar chip device for PCR and hybridization with surface acoustic wave pump. *Lab on a Chip*, 5(3):308–317, 2005.

[141] Xiaoyun Ding, Peng Li, Sz-Chin Steven Lin, Zackary S. Stratton, Nitesh Nama, Feng Guo, Daniel Slotcavage, Xiaole Mao, Jinjie Shi, Francesco Costanzo, and Tony Jun Huang. Surface acoustic wave microfluidics. *Lab Chip*, 13:3626–3649, 2013.

[142] TP Abello. Absorption of ultrasonic waves by various gases. *Physical Review*, 31(6):1083, 1928.

[143] Robert W Leonard. The absorption of sound in carbon dioxide. *The Journal of the Acoustical Society of America*, 12(2):241–244, 1940.

[144] HE Bass and FD Shields. Vibrational relaxation and sound absorption in O_2 / H_2O mixtures. *The Journal of the Acoustical Society of America*, 56(3):856–859, 1974.

[145] HE Bass, LC Sutherland, Joe Piercy, and Landan Evans. Absorption of sound by the atmosphere. In *Physical Acoustics: Principles and methods. Volume 17 (A85-28596 12-71). Orlando, FL, Academic Press, Inc., 1984, p. 145-232.*, volume 17, pages 145–232, 1984.

[146] LB Evans, HE Bass, and LC Sutherland. Atmospheric absorption of sound: theoretical predictions. *The Journal of the Acoustical Society of America*, 51(5B):1565–1575, 1972.

[147] Louis V King. On the acoustic radiation pressure on spheres. In *Proceedings of the Royal Society of London A: Mathematical, Physical and Engineering Sciences*, volume 147, pages 212–240. The Royal Society, 1934.

[148] K Yosioka and Y Kawasima. Acoustic radiation pressure on a compressible sphere. *Acta Acustica United with Acustica*, 5(3):167–173, 1955.

[149] Lord Rayleigh. On the circulation of air observed in kundt's tubes, and on some allied acoustical problems. *Philosophical Transactions of the Royal Society of London*, pages 1–21, 1884.

[150] Carl Eckart. Vortices and streams caused by sound waves. *Physical Review*, 73(1):68, 1948.

[151] James Lighthill. Acoustic streaming. *Journal of Sound and Vibration*, 61(3):391–418, 1978.

[152] WL Nyborg. Acoustic streaming. *Physical Acoustics*, 2(Pt B):265, 1965.

[153] Lawrence A Crum. Bjerknes forces on bubbles in a stationary sound field. *The Journal of the Acoustical Society of America*, 57(6):1363–1370, 1975.

[154] TG Leighton, AJ Walton, and MJW Pickworth. Primary Bjerknes forces. *European Journal of Physics*, 11(1):47, 1990.

[155] Henrik Bruus. Acoustofluidics 2: Perturbation theory and ultrasound resonance modes. *Lab on a Chip*, 12(1):20–28, 2012.

[156] Alexander A Doinikov. Acoustic radiation pressure on a compressible sphere in a viscous fluid. *Journal of Fluid Mechanics*, 267:1–22, 1994.

[157] Henrik Bruus. Acoustofluidics 7: The acoustic radiation force on small particles. *Lab on a Chip*, 12(6):1014–1021, 2012.

[158] Mikkel Settnes and Henrik Bruus. Forces acting on a small particle in an acoustical field in a viscous fluid. *Physical Review E*, 85(1):016327, 2012.

[159] S Shiokawa, Y Matsui, and T Ueda. Liquid streaming and droplet formation caused by leaky Rayleigh waves. In *Ultrasonics Symposium, 1989. Proceedings., IEEE 1989*, pages 643–646. IEEE, 1989.

[160] Gustav Gautschi. *Piezoelectric Sensors*. Springer, 2002.

[161] Adrian Neild, Stefano Oberti, Felix Beyeler, Jürg Dual, and Bradley J Nelson. A micro-particle positioning technique combining an ultrasonic manipulator and a microgripper. *Journal of Micromechanics and Microengineering*, 16(8):1562, 2006.

[162] Martyn Hill, Yijun Shen, and Jeremy J Hawkes. Modelling of layered resonators for ultrasonic separation. *Ultrasonics*, 40(1):385–392, 2002.

[163] Thomas Laurell, Filip Petersson, and Andreas Nilsson. Chip integrated strategies for acoustic separation and manipulation of cells and particles. *Chemical Society Reviews*, 36(3):492–506, 2007.

[164] Daniele Foresti, Nada Bjelobrk, Majid Nabavi, and Dimos Poulikakos. Investigation of a line-focused acoustic levitation for contactless transport of particles. *Journal of Applied Physics*, 109(9):093503, 2011.

[165] Sabina Santesson and Staffan Nilsson. Airborne chemistry: acoustic levitation in chemical analysis. *Analytical and Bioanalytical Chemistry*, 378(7):1704–1709, 2004.

[166] Jinjie Shi, Xiaole Mao, Daniel Ahmed, Ashley Colletti, and Tony Jun Huang. Focusing microparticles in a microfluidic channel with standing surface acoustic waves (SSAW). *Lab on a Chip*, 8(2):221–223, 2008.

[167] Jinjie Shi, Shahrzad Yazdi, Sz-Chin Steven Lin, Xiaoyun Ding, I-Kao Chiang, Kendra Sharp, and Tony Jun Huang. Three-dimensional continuous particle focusing in a microfluidic channel via standing surface acoustic waves (SSAW). *Lab on a Chip*, 11(14):2319–2324, 2011.

[168] Muhsincan Sesen, Tuncay Alan, and Adrian Neild. Microfluidic plug steering using surface acoustic waves. *Lab on a Chip*, 15(14):3030–3038, 2015.

[169] Velimir M Ristic. *Principles of acoustic devices*. John Wiley and Sons, 1983.

[170] Bertram A Auld. *Acoustic fields and waves in solids*. John Wiley and Sons, 1973.

[171] Helmut Nowotny and Ewald Benes. General one-dimensional treatment of the layered piezoelectric resonator with two electrodes. *The Journal of the Acoustical Society of America*, 82(2):513–521, 1987.

[172] Felix Trampler, Stefan A Sonderhoff, Phylis WS Pui, Douglas G Kilburn, and James M Piret. Acoustic cell filter for high density perfusion culture of hybridoma cells. *Nature Biotechnology*, 12(3):281–284, 1994.

[173] Martin Gröschl, Wolfgang Burger, Bernhard Handl, Otto Doblhoff-Dier, Theodor Gaida, and Christine Schmatz. Ultrasonic separation of suspended particles-part iii: Application in biotechnology. *Acta Acustica United with Acustica*, 84(5):815–822, 1998.

[174] Martyn Hill and Robert JK Wood. Modelling in the design of a flow-through ultrasonic separator. *Ultrasonics*, 38(1):662–665, 2000.

[175] Sanjay Gupta and Donald L Feke. Filtration of particulate suspensions in acoustically driven porous media. *AIChE journal*, 44(5):1005–1014, 1998.

[176] Jeremy J Hawkes and W Terence Coakley. Force field particle filter, combining ultrasound standing waves and laminar flow. *Sensors and Actuators B: Chemical*, 75(3):213–222, 2001.

[177] RJ Townsend, M Hill, NR Harris, and MB McDonnell. Performance of a quarter-wavelength particle concentrator. *Ultrasonics*, 48(6):515–520, 2008.

[178] Maria Nordin and Thomas Laurell. Two-hundredfold volume concentration of dilute cell and particle suspensions using chip integrated multistage acoustophoresis. *Lab on a Chip*, 12(22):4610–4616, 2012.

[179] Gregory Goddard and Gregory Kaduchak. Ultrasonic particle concentration in a line-driven cylindrical tube. *The Journal of the Acoustical Society of America*, 117(6):3440–3447, 2005.

[180] Gregory Goddard, John C Martin, Steven W Graves, and Gregory Kaduchak. Ultrasonic particle-concentration for sheathless focusing of particles for analysis in a flow cytometer. *Cytometry Part A*, 69(2):66–74, 2006.

[181] Andreas Lenshof and Thomas Laurell. Continuous separation of cells and particles in microfluidic systems. *Chemical Society Reviews*, 39(3):1203–1217, 2010.

[182] Dwayne A Johnson and Donald L Feke. Methodology for fractionating suspended particles using ultrasonic standing wave and divided flow fields. *Separations Technology*, 5(4):251–258, 1995.

[183] Andreas Lenshof, Cecilia Magnusson, and Thomas Laurell. Acoustofluidics 8: Applications of acoustophoresis in continuous flow microsystems. *Lab on a Chip*, 12(7):1210–1223, 2012.

[184] Jonathan D Adams and H Tom Soh. Tunable acoustophoretic band-pass particle sorter. *Applied Physics Letters*, 97(6):064103, 2010.

[185] Jeremy J Hawkes, Robert W Barber, David R Emerson, and W Terence Coakley. Continuous cell washing and mixing driven by an ultrasound standing wave within a microfluidic channel. *Lab on a Chip*, 4(5):446–452, 2004.

[186] Filip Petersson, Andreas Nilsson, Henrik Jönsson, and Thomas Laurell. Carrier medium exchange through ultrasonic particle switching in microfluidic channels. *Analytical Chemistry*, 77(5):1216–1221, 2005.

[187] Adrian Neild, Stefano Oberti, and Jürg Dual. Design, modeling and characterization of microfluidic devices for ultrasonic manipulation. *Sensors and Actuators B: Chemical*, 121(2):452 – 461, 2007.

[188] F. Beyeler, A. Neild, Stefano Oberti, D.J. Bell, Yu Sun, Jürg Dual, and B.J. Nelson. Monolithically fabricated microgripper with integrated force sensor for manipulating microobjects and biological cells aligned in an ultrasonic field. *Journal of Microelectromechanical Systems*, 16(1):7–15, Feb 2007.

[189] Albrecht Haake, Adrian Neild, Gerald Radziwill, and Jürg Dual. Positioning, displacement, and localization of cells using ultrasonic forces. *Biotechnology and Bioengineering*, 92(1):8–14, 2005.

[190] AL Bernassau, CRP Courtney, J Beeley, BW Drinkwater, and DRS Cumming. Interactive manipulation of microparticles in an octagonal sonotweezer. *Applied Physics Letters*, 102(16):164101, 2013.

[191] Otto Manneberg, Bruno Vanherberghen, Jessica Svennebring, Hans M Hertz, Björn Önfelt, and Martin Wiklund. A three-dimensional ultrasonic cage for characterization of individual cells. *Applied Physics Letters*, 93(6):063901, 2008.

[192] Lord Rayleigh. On waves propagated along the plane surface of an elastic solid. *Proceedings of the London Mathematical Society*, s1-17(1):4–11, 1885.

[193] Arthur A Oliner. Acoustic surface waves. In *Berlin and New York, Springer-Verlag (Topics in Applied Physics. Volume 24), 1978. 342 p (For individual items see A79-16052 to A79-16055)*, volume 24, 1978.

[194] A. Holm, Q. Stürzer, Y. Xu, and R. Weigel. Investigation of surface acoustic waves on $LiNbO_3$, quartz, and $LiTaO_3$ by laser probing. *Microelectronic Engineering*, 31(1):123 – 127, 1996. Electron and Optical Beam Testing of Electronic Devices.

[195] RT Smith and FS Welsh. Temperature dependence of the elastic, piezoelectric, and dielectric constants of lithium tantalate and lithium niobate. *Journal of Applied Physics*, 42(6):2219–2230, 1971.

[196] James F Tressler, Sedat Alkoy, and Robert E Newnham. Piezoelectric sensors and sensor materials. *Journal of Electroceramics*, 2(4):257–272, 1998.

[197] Colin Campbell. *Surface acoustic wave devices for mobile and wireless communications*. Academic Press, 1998.

[198] J David N Cheeke. *Fundamentals and applications of ultrasonic waves*. CRC press, 2010.

[199] Tsung-Tsong Wu, He-Tai Tang, Yung-Yu Chen, and Pei-Ling Liu. Analysis and design of focused interdigital transducers. *Ultrasonics, Ferroelectrics, and Frequency Control, IEEE Transactions on*, 52(8):1384–1392, 2005.

[200] Hiromi Yatsuda. Design techniques for SAW filters using slanted finger interdigital transducers. *Ultrasonics, Ferroelectrics, and Frequency Control, IEEE Transactions on*, 44(2):453–459, 1997.

[201] D Ciplys and R Rimeika. Measurements of electromechanical coupling coefficient for surface acoustic waves in proton-exchanged lithium niobate. *Ultragarsas" Ultrasound"*, 33(3):14–20, 2014.

[202] Minoru Kurosawa, Takayuki Watanabe, Akira Futami, and Toshiro Higuchi. Surface acoustic wave atomizer. *Sensors and Actuators A: Physical*, 50(1):69–74, 1995.

[203] James R Friend, Leslie Y Yeo, Dian R Arifin, and Adam Mechler. Evaporative self-assembly assisted synthesis of polymeric nanoparticles by surface acoustic wave atomization. *Nanotechnology*, 19(14):145301, 2008.

[204] Wei-Kuo Tseng, Jr-Lung Lin, Wang-Chou Sung, Shu-Hui Chen, and Gwo-Bin Lee. Active micro-mixers using surface acoustic waves on Y-cut 128° $LiNbO_3$. *Journal of Micromechanics and Microengineering*, 16(3):539, 2006.

[205] Thomas Frommelt, Marcin Kostur, Melanie Wenzel-Schäfer, Peter Talkner, Peter Hänggi, and Achim Wixforth. Microfluidic mixing via acoustically driven chaotic advection. *Physical Review Letters*, 100(3):034502, 2008.

[206] Marco Cecchini, Salvatore Girardo, Dario Pisignano, Roberto Cingolani, and Fabio Beltram. Acoustic-counterflow microfluidics by surface acoustic waves. *Applied Physics Letters*, 92(10):104103, 2008.

[207] Ghulam Destgeer, Byung Hang Ha, Jinsoo Park, Jin Ho Jung, Anas Alazzam, and Hyung Jin Sung. Microchannel anechoic corner for size-selective separation and medium exchange via traveling surface acoustic waves. *Analytical Chemistry*, 87(9):4627–4632, 2015.

[208] Viktor Skowronek, Richard W Rambach, Lothar Schmid, Katharina Haase, and Thomas Franke. Particle deflection in a poly (dimethylsiloxane) microchannel using a propagating surface acoustic wave: size and frequency dependence. *Analytical Chemistry*, 85(20):9955–9959, 2013.

[209] Yannyk Bourquin, Abeer Syed, Julien Reboud, Lisa C Ranford-Cartwright, Michael P Barrett, and Jonathan M Cooper. Rare-cell enrichment by a rapid, label-free, ultrasonic isopycnic technique for medical diagnostics. *Angewandte Chemie*, 126(22):5693–5696, 2014.

[210] Adrien Bussonnière, Yannick Miron, Michaël Baudoin, Olivier Bou Matar, Michel Grandbois, Paul Charette, and Alan Renaudin. Cell detachment and label-free cell sorting using modulated surface acoustic waves (SAWs) in droplet-based microfluidics. *Lab on a Chip*, 14(18):3556–3563, 2014.

[211] Lothar Schmid, David A. Weitz, and Thomas Franke. Sorting drops and cells with acoustics: acoustic microfluidic fluorescence-activated cell sorter. *Lab on a Chip*, 14:3710–3718, 2014.

[212] David J Collins, Belinda Morahan, Jose Garcia-Bustos, Christian Doerig, Magdalena Plebanski, and Adrian Neild. Two-dimensional single-cell patterning with one cell per well driven by surface acoustic waves. *Nature Communications*, 6, 2015.

[213] Yuchao Chen, Ahmad Ahsan Nawaz, Yanhui Zhao, Po-Hsun Huang, J Phillip McCoy, Stewart J Levine, Lin Wang, and Tony Jun Huang. Standing surface acoustic wave (SSAW) based microfluidic cytometer. *Lab on a Chip*, 14(5):916–923, 2014.

[214] Kyungheon Lee, Huilin Shao, Ralph Weissleder, and Hakho Lee. Acoustic purification of extracellular microvesicles. *ACS Nano*, 9(3):2321–2327, 2015.

[215] Yuchao Chen, Sixing Li, Yeyi Gu, Peng Li, Xiaoyun Ding, Lin Wang, J Philip McCoy, Stewart J Levine, and Tony Jun Huang. Continuous enrichment of low-abundance cell samples using standing surface acoustic waves (SSAW). *Lab on a Chip*, 14(5):924–930, 2014.

[216] Ye Ai, Claire K Sanders, and Babetta L Marrone. Separation of escherichia coli bacteria from peripheral blood mononuclear cells using standing surface acoustic waves. *Analytical Chemistry*, 85(19):9126–9134, 2013.

[217] David J Collins, Tuncay Alan, and Adrian Neild. Particle separation using virtual deterministic lateral displacement (vDLD). *Lab on a Chip*, 14(9):1595–1603, 2014.

[218] Mary Ann H Weiser and Robert E Apfel. Extension of acoustic levitation to include the study of micron-size particles in a more compressible host liquid. *The Journal of the Acoustical Society of America*, 71(5):1261–1268, 1982.

[219] E Welter and B Neidhart. Acoustically levitated droplets: a new tool for micro and trace analysis. *Fresenius' Journal of Analytical Chemistry*, 357(3):345–350, 1997.

[220] Yoichi Ochiai, Takayuki Hoshi, and Jun Rekimoto. Three-dimensional mid-air acoustic manipulation by ultrasonic phased arrays. *PLoS ONE*, 9(5):e97590, 05 2014.

[221] Georges Snounou, Suganya Viriyakosol, William Jarra, Sodsri Thaithong, and K Neil Brown. Identification of the four human malaria parasite species in field samples by the polymerase chain reaction and detection of a high prevalence of mixed infections. *Molecular and Biochemical Parasitology*, 58(2):283–292, 1993.

[222] JP Mills, M Diez-Silva, DJ Quinn, M Dao, MJ Lang, KSW Tan, CT Lim, G Milon, PH David, O Mercereau-Puijalon, et al. Effect of plasmodial RESA protein on deformability of human red blood cells harboring *plasmodium falciparum*. *Proceedings of the National Academy of Sciences*, 104(22):9213–9217, 2007.

[223] Hope A Cranston, Charles W Boylan, Gregory L Carroll, Salvatore P Sutera, IY Gluzman, DJ Krogstad, et al. *Plasmodium falciparum* maturation abolishes physiologic red cell deformability. *Science*, 223(4634):400–403, 1984.